REFERENCE ONLY

UNIVERSITY OF LONDON THESIS

Degree PhD Year 2006 Name of Author CREIGHAN, S.C.

Laboratory Studies of the Formation of Molecular Hydrogen on Surfaces at Cryogenic Temperatures.

Susan Christine Creighan

Thesis submitted for the degree of Doctor of Philosophy

University College London
University of London

2006

ProQuest LLC
789 East Eisenhower Parkway
P.O. Box 1346
Ann Arbor, MI 48106-1346

Abstract

The interstellar medium (ISM) is the region of space between the stars, where star and planet formation occurs. Molecular hydrogen in the ISM initiates all the chemistry that occurs in these regions and without it, no stars or planets could form. The molecules formed by the chemistry initiated by H_2 provide cooling mechanisms for the huge molecular clouds which collapse to form stars. It is well known that the abundance of molecular hydrogen in the ISM is too high for it to form through gas phase processes alone and hence, the widely accepted theory is that H_2 forms through heterogeneous catalysis on the surfaces of interstellar dust grains. These grains make up approximately 1% of the mass of the ISM and are thought to be carbonaceous or silicate in nature. Despite its importance, only recently have laboratory experiments been set-up to study the formation of molecular hydrogen on interstellar grain analogues in detail.

This thesis presents results from an experiment designed to determine what happens to the energy released on the formation of H_2, under conditions similar to those of the ISM. The experiment involves using an atom source, ultrahigh vacuum chamber and cryogenic cooling methods in order to reach the temperatures and pressures of interstellar space. The laser technique of Resonance Enhanced Multiphoton Ionisation (REMPI) is employed to look at the internal energy distribution of newly formed H_2 and HD molecules from a graphite surface. Improvements to an existing experiment are described, including the introduction of a second atom source to study HD formation. New results are presented, including the first observations of molecular hydrogen formed ro-vibrationally excited in states $v'' = 1$ and $v'' = 2$. The results are placed in context with the results of other experiments to form H_2 under ISM conditions, and the astrophysical implications are discussed.

Acknowledgements

I would like to thank the following people for their help in getting this thesis finished:

Steve Price, for his excellent supervision and expertise over the course of my PhD, Wendy Brown for being a great second supervisor and James Perry for teaching me how to use all the equipment and helping me realise it isn't as scary as it first appears!

All those who have helped in the lifting of the dreaded coldhead, particularly Amandeep Bolina and Daniel Stone, and everyone who has sympathised with my numerous spanner injuries, but prevented me from inflicting any fatal blows on the kit...

All the technical support staff, without whom the experiments in the basement would be even more difficult to get working.

Everyone in the Physical Chemistry group, past and present - you know who you are – thanks for everything!

My family and all my friends, including those outside the world of UCL chemistry, who have provided support and entertainment when needed.

Lastly, but most importantly, Stuart – I would never have got to this stage without you. Thank you.

Table of Contents

List of Figures

Chapter 1.

Chapter 2.

Chapter 3.

Chapter 4.

Chapter 5.

Chapter 6.

Appendix A.

Appendix B.

List of Tables

Chapter 1.

Chapter 3.

Chapter 5.

Chapter 1. Introduction

The interstellar medium (ISM), as its name suggests, is the region of space between the stars. Although most of the matter in the Universe is tied up in stars and planets, the regions between them are far from empty and much important chemistry occurs in this environment. The ISM includes huge volumes of dust grains and gas called interstellar clouds, of mean density 10^{10} atoms m^{-3} [1]. The gas in these clouds is around 90% hydrogen and the clouds can vary in size and density. The clouds are loosely classified as 'dense' ('dark' or 'molecular') 'diffuse' and 'HII' regions; in the latter region, hydrogen exists mostly in an ionised state. Dust grains account for 1% of the mass of the clouds and, as will become clear, this dust plays an extremely important role in the chemistry of these regions. The clouds are themselves the sites of star formation, as will be discussed in detail later in this section.

Molecular hydrogen makes up most of the gas in the molecular clouds and this simple molecule, H_2, has been described as the 'key to interstellar chemistry' [2]. Molecular hydrogen is the dominant molecule in the ISM and is approximately 10^5 times more abundant than CO, the next most abundant molecule. Hydrogen is also the most abundant element in the Universe, in all its forms it accounts for 75% by mass of the Universe or 92% by number density [1]. Hydrogen was among the very first of the elements to be formed at the beginning of the Universe, along with helium and very small amounts of lithium, and was also the key to the formation of the first stars and large-scale structures in the early Universe. The rest of this Chapter will describe the role of hydrogen in the ISM, including theories for its formation, and will introduce the experiments performed in the UCL Cosmic Dust laboratory to investigate the formation of molecular hydrogen under conditions similar to those in the ISM.

1.1. Hydrogen in the Early Universe

Without both atomic and molecular hydrogen, the early Universe would not have been able to cool to the temperatures needed to allow clouds of gas to collapse to form galaxies and stars. After the 'Big Bang', the early Universe began expanding and cooled enough to allow electrons to combine with positive ions to form, mostly, the neutral atoms hydrogen and helium [2]. This expansion ensured that not all the electrons were able to recombine with protons and so the Universe remained partially ionised, an important factor for the chemistry occurring in space. In order for the gases present in the early Universe to collapse under gravity to form stars and galaxies, cooling mechanisms for the hot gas were essential since the pressure of the hot gas resisted collapse. Initially, at temperatures above 10,000 K, hydrogen atoms were able to radiate away some of this heat through being ionised [2].

A new cooling mechanism for the clouds resulted following the formation of molecular hydrogen. Molecular hydrogen initially formed through electron and proton catalysed reactions such as:

$$\begin{aligned} H + e^- &\rightarrow H^- + h\nu \\ H^- + H &\rightarrow H_2 + e^- \end{aligned} \qquad (1.1.1)$$

or

$$\begin{aligned} H + H^+ &\rightarrow H_2^+ + h\nu \\ H_2^+ + H &\rightarrow H_2 + H^+ \end{aligned} \qquad (1.1.2)$$

Through collisions with atomic hydrogen, the kinetic energy in the gas resulted in vibrational levels in the molecules being populated. These vibrationally excited molecules could then emit radiation and allow the gas to cool. At the high temperatures of the gases in the early Universe, vibrational levels of H_2 were easily populated and so the molecule was a very effective coolant. Molecular hydrogen

also acted as a coolant in clouds with gas temperatures above 100 K through excitation of rotational levels within the molecule, followed by emission. Hence, hydrogen acts as an effective coolant over a wide gas temperature range. However, molecular hydrogen is not just important as a coolant in interstellar space and in fact it is largely responsible for the chemistry occurring in the interstellar medium.

1.2. Hydrogen in the ISM

As mentioned above there are three loosely classified regions of the ISM. Diffuse clouds have much lower densities than either dark clouds or HII regions. A typical diffuse cloud has a density on the order of 10^7 – 10^9 molecules m^{-3} and the gas temperature in these clouds is around 100 K. Diffuse clouds are reasonably well penetrated by radiation, such as photons and cosmic rays, and therefore most of the hydrogen is atomic, since molecular hydrogen is quickly dissociated [1, 2]. However, astronomical observations show that there is still a significant fraction of molecular hydrogen in these clouds, and in order for it to remain as H_2 in the face of such radiation bombardment, there must be a very efficient mechanism for its formation. Other simple molecular species are also found in diffuse clouds, such as HCN, CN, CH^+. Those species in the cloud with an ionisation potential less than atomic hydrogen, such as atomic carbon and sulphur, can be photoionised, whilst those with an ionisation potential greater than atomic hydrogen, such as atomic nitrogen and oxygen exist in a neutral state. These species remain neutral because the high energy radiation is absorbed by the large number of hydrogen atoms.

Dark (dense or molecular) clouds are where most of the molecules in the ISM are found and are formed, in contrast to the diffuse clouds. The higher densities of dust grains in dark clouds result in the molecules being shielded from the UV and cosmic ray radiation. To date, over 120 different molecules have been observed spectroscopically in dense clouds as shown in Table 1.1 below. In these dense regions, most of the hydrogen is molecular. These dark clouds have densities of

around $10^9 - 10^{10}$ molecules m^{-3} and are much cooler than diffuse clouds, with a gas temperature of approximately 10 K [1].

Table 1.1. The molecules observed in the ISM to date (adapted from http://www.ajmarkwick.com/achemnet/stats.php?mode=1&flat=0).

2 atoms	3 atoms	4 atoms	5 atoms	6 atoms	7 atoms	>7 atoms
AlF	C_3	c-C_3H	C_5	C_5H	C_6H	CH_3C_3N
AlCl	C_2H	l-C_3H	C_4H	C_5O	CH_2CHCN	$HCOOCH_3$
C_2	C_2O	C_3N C_3O	C_4Si	C_2H_4	CH_3C_2H	CH_3COOH
CH	C_2S	C_3S C_2H_2	l-C_3H_2	CH_3CN	HC_5N	CH_3C_4H
CH^+	CH_2	CH_2D^+	c-C_3H_2	CH_3NC	$HCOCH_3$	CH_3CH_2CN
CN	HCN	HCCN	CH_2CN	CH_3OH	NH_2CH_3	$(CH_3)_2O$
CO	HCO	HCNH.	CH_4	CH_3SH	c-C_2H_4O	CH_3CH_2OH
CO^+	HCO^+	HNCO	HC_3N	HC_3NH^+	CH_2CHOH	HC_7N
CP	HCS^+	HNCS	HC_2NC	HC_2CHO		C_8H
CS	HOC^+	$HOCO^+$	HCOOH	$HCONH_2$		CH_3C_5N
CSi	H_2O	H_2CO	H_2CHN	l-H_2C_4 C_5N		$(CH_3)_2CO$
HCl	H_2S	H_2CN	H_2C_2O			NH_2CH_2COOH
H_2	HNC	H_2CS	H_2NCN			HC_9N
KCl	HNO	H_3O^+ NH_3	HNC_3			$HC_{11}N$
NH	MgCN	SiC_3	SiH_4			CH_8 CH_2OHCHO
NO	MgNC		H_2COH^+			C_7H
NS	N_2H^+					H_2C_6
NaCl	N_2O					
OH	NaCN					
PN	OCS					
SO	SO_2					
SO^+	c-SiC_2					
SiN	CO_2					
SiO	NH_2					
SiS	H_3^+					
HF	AlCN					
SH						

Unlike many other molecules observed in the ISM, molecular hydrogen does not have a rich spectrum in the radio and microwave regions of the spectrum. Hence, when molecules such as OH and CO were first observed in space in the 1960s, using radio astronomy, H_2 was not detected despite its abundance. Many of molecular hydrogen's lowest energy transitions lie at infrared (IR) wavelengths to which the Earth's atmosphere is opaque [2]. Likewise, many of molecular hydrogen's highest energy transitions lie at UV wavelengths where again, atmospheric absorption is a problem. Because of its universal abundance, astronomers predicted that far more

H_2 than any other molecule would exist in astronomical sources and, even before it was observed, a detailed theory for its production and destruction was developed [3].

Molecular hydrogen outside the solar system was detected for the first time in 1970 by Carruthers [4]. This observation was performed by launching a UV spectrometer above the Earth's atmosphere on a rocket. The spectrometer was pointed in the direction of the star ξ Persei and detected the Lyman bands of interstellar molecular hydrogen between 100-110 nm. In the same study, the Lα absorption of atomic hydrogen was also detected.

A more detailed study of H_2 in interstellar space was carried out using the Copernicus satellite in 1975 [5]. This study again used a UV spectrometer directed towards nearby stars. A measurement of the rotational excitation of H_2 molecules was also carried out in this study, resulting in a determination of the gas temperature of 81 ± 13 K.

In 1976, the first infrared emissions from interstellar molecular H_2 were observed [6, 7] using ground based instruments, at wavelengths where the Earth's atmosphere can be penetrated by IR radiation (between 2.2 and 2.4 microns). These studies observed the quadrupole emission of molecular hydrogen. The rotational temperature of the gas was determined to be on the order of 2000 K in this study, much higher than expected. This temperature was attributed to high internal excitation of H_2 that had formed on the surfaces of dust grains. This formation on grain surfaces will be discussed in section 1.4.

Information about the abundance of H_2 in the ISM can be derived through the observations of other molecules, especially CO which is the second most abundant molecule in the ISM. In clouds where both H_2 and CO molecules can be observed, the H_2:CO ratio is typically $n(H_2) = 10^5\, n(CO)$ [1, 8]. In regions where H_2 cannot be directly observed, such as dark clouds, astronomers can infer its abundance through

determining the abundance of CO, since the H_2:CO ratio is believed to be constant throughout the ISM [1].

1.3. Chemistry in the ISM

Many of the molecules found in the ISM form through ion-neutral or neutral-neutral routes. Hydrogen dominates this interstellar gas phase chemistry because the other reactive elements, oxygen, nitrogen, carbon, iron, silicon and sulphur are very much less abundant than hydrogen. This abundance of hydrogen means that these other reactive species are much more likely to collide with atoms or molecules of hydrogen than with any other species [1]. Interstellar chemistry particularly depends on the amount of *molecular* hydrogen present, as a collision of any atom with a molecule of H_2 will result in a more efficient reaction than a collision of another atom with a H atom. Reactions with H_2 are more efficient than with H-atoms because atom-atom interactions occur on a timescale too fast to enable the excess energy on formation of a molecule to be radiated away. Hence, the atoms will come apart before they can adjust energetically and exist as a molecule [1]. In contrast, reactions between H_2 molecules and atoms of other reactive elements, or between any molecule and an H-atom, may be more efficient because of the rearrangements that can occur to remove the excess energy before the species fall apart. For example:

$$X + H_2 \rightarrow XHH \begin{cases} \nearrow XH + H \\ \searrow X + H_2 \end{cases} \qquad (1.3.1)$$

Larger molecules are often created through interaction with H_2, via the formation of the H_3^+ ion. Cosmic rays (c.r.), usually highly energetic protons, cause ionisation of H_2. The resulting H_2^+ ions then form H_3^+ ions by interaction with further H_2 molecules:

$$H_2 + c.r \rightarrow H_2^+ + e^- + c.r \qquad (1.3.2)$$

$$H_2^+ + H_2 \rightarrow H_3^+ + H \qquad (1.3.3)$$

The H_3^+ ion then leads to the formation of molecules such as water through reactions with O atoms *via* schemes such as:

$$\begin{aligned} H_3^+ + O &\rightarrow OH^+ + H_2 \\ OH^+ + H_2 &\rightarrow H_2O^+ + H \\ H_2O^+ + H_2 &\rightarrow H_3O^+ + H \\ H_3O^+ + e^- &\rightarrow OH + 2H \\ &\rightarrow H_2O + H \end{aligned} \qquad (1.3.4)$$

OH and H_2O are found in reasonably high abundances in the ISM and can lead to the creation of other molecules such as CO, the second most abundant molecule in interstellar space.

$$OH + C \rightarrow CO + H \qquad (1.3.5)$$

or

$$\begin{aligned} C^+ + OH &\rightarrow CO^+ + H \\ CO^+ + H_2 &\rightarrow HCO^+ + H \\ HCO^+ + e^- &\rightarrow CO + H \end{aligned} \qquad (1.3.6)$$

H_2 can also participate in radiative association reactions with, for example, C^+ to form simple hydrocarbons, *via*:

$$\begin{aligned} H_2 + C^+ &\rightarrow CH_2^+ + h\nu \\ CH_2^+ + H_2 &\rightarrow CH_3^+ + H \\ CH_3^+ + e^- &\rightarrow CH_2 + H \end{aligned} \qquad (1.3.7)$$

The formation of these molecules in the ISM, especially those with dipole moments such as CO, is important as they can act as coolants of interstellar clouds, leading to the collapse of these clouds to form stars [1, 2]. Molecular clouds collapse under their own gravity and form stars when their density is high enough for nuclear fusion to occur; that is, when the mass of the cloud is higher than a critical mass, M_{crit}. However, as the cloud starts to collapse, the gravitational potential energy released is transferred to kinetic energy amongst the molecules in the cloud. This kinetic energy, and the resulting increase in pressure and temperature, then results in a resistance to the collapse of the cloud. Therefore, molecules such as CO, H_2O and OH are useful to radiate away this energy and allow the cloud to cool and continue to collapse [1, 2].

At low cloud temperatures (10 – 100 K) CO is the most important molecular coolant, radiating excess energy in the millimetre wavelength range. As mentioned earlier, at higher cloud temperatures, H_2 itself can act as a coolant. H_2 does not posses a dipole moment so does not radiate by electric dipole transitions. Instead, H_2 radiates by electric quadrupole transitions and only $\Delta J = \pm 2$ transitions occur.

1.4. Hydrogen Formation in Interstellar Space

The previous section has emphasised the importance of hydrogen in the interstellar medium but one of the major problems for astronomers has been accounting for the abundance of hydrogen in interstellar space. The formation of molecular hydrogen must be very efficient since the background flux of photons can destroy H_2, and about 10% of absorptions of interstellar radiation by H_2 result in dissociation. By considering the rates of these reactions, it has been determined that a H_2 molecule in a diffuse cloud will have a lifetime of ~1000 years, which is very short on an astrophysical timescale [2].

As described in section 1.1, H_2 was formed in the early universe through electron and proton catalysed reactions. In interstellar clouds, electrons and protons are now

minor constituents and have abundances of less than 1 in 10,000 compared with hydrogen, hence proton or electron catalysed mechanisms of formation will be very slow [2, 9]. In fact, using these electron and proton mechanisms, it is impossible to explain an abundance of H_2 greater than ~1 part per billion with respect to the number of H-atoms, which is around 1000 times smaller than the lowest observed H_2 abundances [2]. Simple H + H gas phase reactions are also highly inefficient for forming H_2 in the current ISM since, as discussed earlier, the atoms will have flown apart before they are able to radiate away the ~4.5 eV of binding energy that is released on H_2 formation. Hence, the reaction:

$$H + H \rightarrow H_2 + h\nu \qquad (1.4.1)$$

rarely occurs in the ISM.

A three body reaction such as:

$$H + H + M \rightarrow H_2^* + M \qquad (1.4.2)$$

would be more efficient for H_2 formation as the third body, M, could remove the excess energy from H_2^*. However, the probability of three bodies colliding under the pressure conditions of the ISM is very low and this reaction is unimportant below H atom densities of ~10^{14} m^{-3} [1, 2]. The reason for this is clear when the rate coefficient for reaction 1.4.2 is considered; it has a value of 8.82×10^{-33} $cm^6 molec^{-2} s^{-1}$ [10]. This three body reaction does however occur in circumstellar environments, where the H-atom density is high enough, $\geq 10^{18}$ m^{-3}.

The current, widely accepted theory for the formation of molecular hydrogen in the ISM is that it forms through heterogeneous catalysis on the surfaces of cosmic dust grains [1, 2, 4, 6, 9, 11-46]. Specifically:

$$H + H_{ads} \rightarrow H_2 (v,J) + \text{grain} \leftarrow 2H_{ads} \qquad (1.4.3)$$

where H_{ads} indicates an H atom adsorbed on a dust grain. This catalytic process is thought to be highly efficient and it has been proposed that every H atom arriving at a grain surface leaves as part of a H_2 molecule [17, 20]. It is this formation process that is under investigation in this thesis.

1.5. Other Molecules in the ISM

As well as molecular hydrogen, the abundance of a number of other molecules in the ISM cannot be explained by simple gas phase chemistry alone. The composition of some interstellar ices is also a problem for astronomers. In dark clouds particularly, at the very low temperatures of the ISM, simple molecules can freeze out on the surfaces of dust grains causing icy mantles to form. The composition of these ices can vary in different regions of the ISM but they have been observed to include molecules such as H_2O, CO, CH_3OH, CH_4 and NH_3 [45]. However, in the gas phase, the only molecule in the above list abundant enough to account for the deposition of its ice by freeze-out in a short enough timescale is CO. Hence, an alternative mechanism is required for the formation of the other molecules detected in interstellar ices. In a similar manner to the formation of H_2, the formation of these molecules on the surfaces of dust grains, has been proposed as the solution to this ice problem, and many new experiments have been set up to investigate this in the laboratory [47-59].

The reaction of CO with H-atoms on surfaces to form ices has proven particularly controversial. It was shown initially by Hiroaka and co-workers [47] that reaction of CO with H-atoms led to the formation of both H_2CO and CH_3OH ices, although in low yields. Subsequently, further studies by the same group found that no CH_3OH could be detected but that H-atom abstraction from intermediates occurred [48]. The most recent study by the same group has looked at the reaction of H and D atoms with CH_3OH and H_2CO and found that both addition and abstraction reactions of H-atoms can occur [58]. Similar experiments investigating the reaction of H-atoms with CO have been carried out by Watanabe and co-workers [57]. This group found

reasonable yields of both CH_3OH and H_2CO through the reaction of H-atoms with CO-H_2O mixtures. They also showed that hydrogenation was efficient below a surface temperature of 12 K.

Experiments have also been set-up in the laboratory to investigate the interaction of molecules found in the ices in the ISM with surfaces. For example, experiments at Nottingham University [50] have investigated the thermal desorption of astrophysically relevant molecules from molecular ices and also the trapping of CO in interstellar ice analogues and the interaction of CO with water ice [49, 51, 52, 56]. These experimental results have also been used in astrophysical models of the evaporation of ices near massive stars [55]. Experiments investigating the thermal desorption of water ice resulted in the conclusion that thermal desorption of H_2O ice in the dense ISM could occur at higher temperatures than previously thought [49]. Studies on the entrapment of CO in interstellar ice analogues showed that CO could diffuse into the porous structure of H_2O at temperatures as low as 15 K, and that a phase transition between two amorphous forms of H_2O ice occurred over the temperature range 30-70 K, resulting in collapse of the pores and hence entrapment of the CO molecules [52]. A follow up study using both temperature programmed desorption (TPD) and reflection absorption infrared spectroscopy (RAIRS) was performed to construct a rate model for the desorption of CO over astronomically relevant timescales [51]. Studies of the desorption of a number of astronomically relevant molecules from interstellar ice analogues have also been carried out by the Nottingham group [56]. They found in this study that the species could be separated into three groups based on their desorption behaviour. These groups were water-like species, which showed a single relevant desorption close to that of water; CO-like species, which showed 'volcano desorption' and co-desorption of trapped molecules; and intermediate species, which showed two desorptions for trapped molecules and possibly a small monolayer desorption for molecules small enough to diffuse through porous amorphous H_2O ice.

Experiments based at Leiden University using 'SURFRESIDE' (SURFace REaction SImulation DEvice) have been used to study surface chemistry under interstellar and protostellar conditions [53]. The experiments have looked at the physical behaviour of CO and CH_3OH during thermal processing and deduced that CO can be trapped by methanol, in a similar manner to the way it can be trapped by water. More recently, the Leiden group have used infrared spectroscopy to look at adsorption of CO at bare grain surfaces, using zeolite wafers as grain analogues [59]. From their results, the Leiden workers proposed that the recently detected 2175 cm^{-1} infrared band at the European Southern Observatory could be due to CO chemisorbed at bare grain surfaces in the ISM, suggesting that gas-grain interactions in the ISM did not necessarily result in ice mantle formation.

New experiments investigating the interaction of methanol with a highly oriented pyrolitic graphite (HOPG) surface have been carried out in the surface science laboratory at UCL [60] again using both TPD and RAIRS techniques. These workers found that methanol could physisorb to HOPG cooled to ~100 K, at all the exposures investigated and that the desorption of crystalline CH_3OH was observed in the TPD spectra. These workers have also investigated the interaction of other important interstellar ice molecules with HOPG, including H_2O and NH_3 [61].

1.6. Interstellar Dust Grains

Not only are dust grains believed to be active sites for molecule formation, they are also important in establishing thermal equilibrium in interstellar clouds and in controlling the collapse of these clouds to form stars. In diffuse clouds, the surface temperature of the grains is ~15 K [19] as a result of a kinetic balance between emission and absorption of radiation. However, in dense clouds, which are much more shielded from background photons, the grain temperatures are much lower, around 5 – 10 K. The dust and gas in interstellar clouds can also be at very different temperatures, with the gas usually being warmer than the dust.

Dust grains were first observed, albeit unknowingly, in 1784 by William Herschel. Herschel noted regions in the sky where it appeared there was a complete absence of stars, which he called 'holes in the sky'. These regions were most obvious against the rich star-fields of the Milky Way [46, 62]. At the time, it was not clear whether something was blocking the light from the background stars or whether these regions were indeed devoid of stars. It is now well known that the medium obscuring the background starlight is in fact dust grains which not only absorb the radiation from the stars but also scatter it [46]. An example of a 'hole in the sky' is shown in Figure 1.1 below.

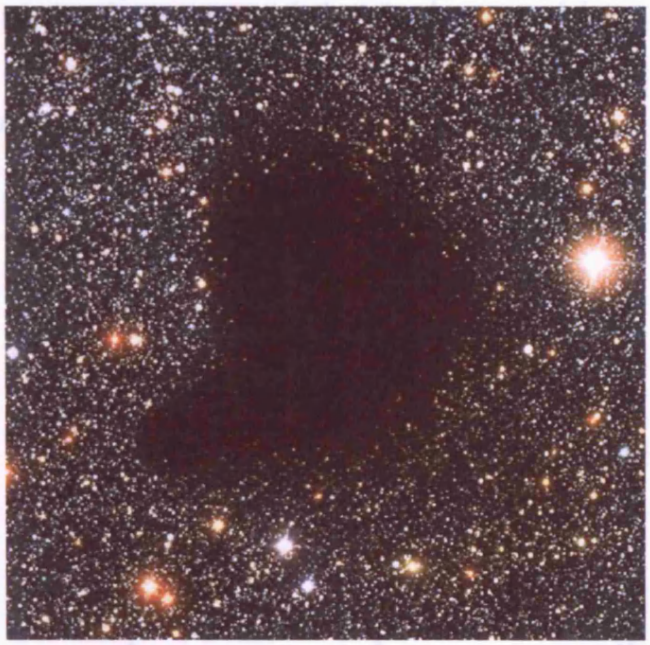

Figure 1.1. Barnard 68. The dust particles in this dense interstellar cloud result in the extinction of the background visible starlight. From http://antwrp.gfsc.nasa.gov/apod/ap990511

Since the first observation of these dark objects, many further pieces of evidence have been found to support the existence of dust grains. The obscuration of the starlight is called extinction and one piece of evidence for dust grains is the interstellar extinction curve. This curve is shown below in Figure 1.2 and illustrates the normalised rate of the extinction of starlight as a function of wavelength. It has

been shown that the extinction of light is most effective when there is an approximate match between the size of the grain particles and the wavelength of light they obscure [45]. The curve shows a steady rise from infrared wavelengths up to visible wavelengths, where a large bump is observed. After this bump, the curve continues to rise into the ultraviolet region of the spectrum.

This extinction curve can be readily modelled by a distribution of dust grain sizes, ranging from a few nanometres up to around 1 μm [46]. The curve can also give us information on the composition of the grains. Various dielectric materials have been used in models of the extinction curve, including silicates and materials made from carbon. It has also been suggested that the bump at 4.1 μm is mainly due to graphite, and Figure 1.2 shows the contribution to the extinction curve expected to be due to graphite.

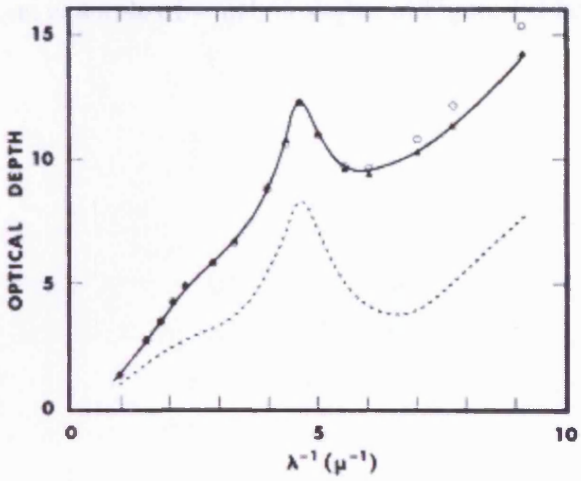

Figure 1.2. Plot of the interstellar extinction curve, taken from reference [63]. Dotted line shows the proposed contribution of graphite to the curve.

Further evidence for the existence of interstellar grains is the fact that the starlight is generally partially linearly polarised after passing through the dust in the clouds, and the amount of polarisation appears to be proportional to the amount of extinction. For this polarisation to occur in the ISM, the interstellar grains must not be spherical and must also have some degree of alignment, caused by the interstellar magnetic

field [1, 46]. The polarisation only exists to a few percent since the grains are rotating and their orientations will also be affected by collisions.

Yet more evidence for the existence and composition of grains is inferred from interstellar elemental depletion [45]. The relative abundances of elements in the sun are assumed to be typical of the galaxy, since the sun is assumed to have formed from a typical interstellar cloud. However, many elements are much less abundant in interstellar clouds compared with in the sun. This depletion can be explained if some of the gas in the circumstellar clouds is cooling and forming stable solids such as silicates, graphite and metal oxides which can then accrete to form dust grains. Dust grains are also believed to scatter diffuse starlight, since this scattering cannot be attributed to atoms or molecules but to species the size of dust grains. This scattered starlight can, in some cases, be detectable and this generally occurs near bright stars. These situations where the scattered light is detectable are called reflection nebulae, an example of which is shown in Figure 1.3 below.

Figure 1.3. The Corona Australis Nebula. This reflection nebula results from scattering of light from bright stars in a dusty cloud. Image © 1991-2002, Anglo-Australian Observatory.

One of the most effective tools for investigating the composition of dust grains in the ISM is infrared (IR) spectroscopy. Carrying out IR observations from the ground is extremely difficult because of the nature of the Earth's atmosphere, as discussed earlier in section 1.2. Most of the recent, accurate, observations have therefore been carried out using the European satellite the Infrared Space Observatory (ISO) [19, 46]. Using ISO, absorption of IR light by amorphous and crystalline silicates has been clearly identified, as well as absorption by molecular ices, including H_2O, CO_2, CO and CH_3OH. Carbon signatures and lines attributed to polycyclic aromatic hydrocarbons (PAHs) have also been observed, although individual PAHs have yet to be assigned [19, 46]. Observations towards diffuse interstellar clouds have shown little or no evidence of ices on the grains in this very low density environment [19, 46].

Using all of the evidence above, it is possible to build up a model of a typical interstellar grain. The size of the grains range between 0.1-10 μm, their cores are thought to be made from metals, silicates and carbonaceous materials and in dense clouds, they are thought to be covered in icy mantles. A schematic diagram of a grain is therefore shown in Figure 1.4 below.

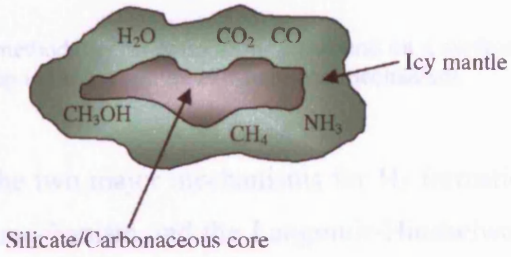

Figure 1.4. Schematic representation of a typical interstellar dust grain.

1.7. Formation Mechanisms

In order to study the formation of molecules on surfaces, such as those similar to interstellar dust grains, it is necessary to consider the surface processes that can occur. The chemistry on the surfaces of dust grains can be considered in a series of steps, from adsorption on the surface, through diffusion across the surface, reaction with another species on the surface, possible mantle accumulation and processing and then finally, desorption. It is highly likely that, at the extreme low temperatures of the ISM, almost all species that collide with a grain surface will stick to it, and many theoretical models of surface processes in the ISM have assumed a sticking probability of unity [15, 25]. The mobility of the species on the surface once it has adsorbed then needs to be considered, followed by the nature of the mobility, be it surface diffusion or quantum tunnelling as shown in Figure 1.5. It is thought that light adsorbates, such as hydrogen atoms, will be highly mobile on the surface of dust grains. The variation in the strength of the interaction of the adsorbate with the

surface, and therefore the mobility of the adsorbate, leads to different possible reaction mechanisms. These possible mechanisms will be described below.

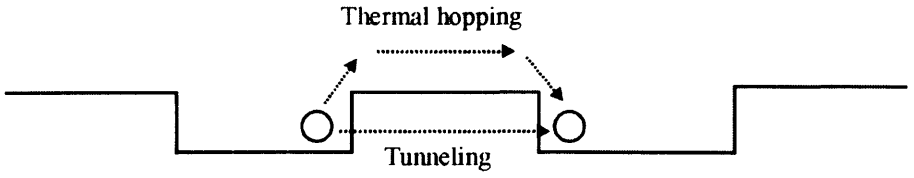

Figure 1.5. Possible methods for an atom to move around on a surface into other adsorption sites, a critical step in the Langmuir-Hinshelwood mechanism.

It is thought that the two major mechanisms for H_2 formation on dust grains are the Eley-Rideal (ER) mechanism and the Langmuir-Hinshelwood (LH) mechanism. A third possible mechanism is the 'hot atom' mechanism [27]. In the ER case, an atom already bound to the surface is approached by an atom from the gas phase and these two atoms bind to form a molecule which then desorbs from the surface. In the LH mechanism, both atoms are already thermalised on the surface and diffuse across the surface, either by tunnelling or thermal hopping, until they meet and recombine to form H_2 and then desorb. Both these mechanisms are shown schematically in Figure 1.6 below. The 'hot atom' mechanism is intermediate between the LH and ER types. In this scenario, one of the H atoms is trapped on the surface and the second, from the gas phase, is temporally trapped on the surface, but reacts with the bound atom before thermalisation with the surface can occur [27]. All three of these mechanisms have been studied theoretically [12-15, 17, 20, 24-32, 36, 39-42, 64-66] although the majority of theoretical studies have concentrated on the ER mechanism. However, it is the LH mechanism that is thought to be the most relevant in diffuse clouds, where a relatively low coverage of H atoms on the dust grains is expected [67].

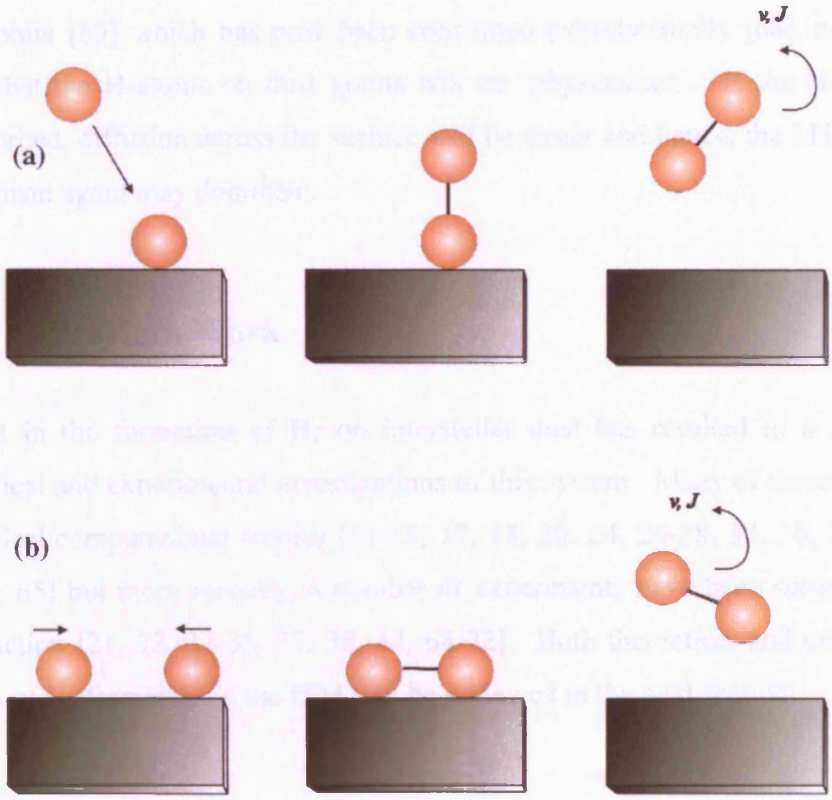

Figure 1.6. Representations of two of the possible formation mechanisms for H_2 on a surface. (a) shows the ER mechanism whilst (b) shows the LH mechanism.

The different formation mechanisms may affect the internal energy of the product H_2 molecules. The dominance of a particular formation mechanism over another may depend on the sticking probability of H on the surface and/or the grain and gas temperatures. The background gas may also affect the mechanism of formation. A high initial coverage of atoms on the surface may result in the ER mechanism for H_2 formation dominating, since the likelihood of an atom from the gas phase hitting an atom on the surface is enhanced if there are more atoms on the surface to begin with. However, at low coverages, it is much more likely that the LH mechanism will dominate since, the fewer atoms there are on the surface, the less likely it is that an atom from the gas phase will collide with another atom on the surface, react and desorb as a molecule.

Theoretical studies have shown that a barrier exists to the chemisorption of H-atoms on graphite [65] which has now been confirmed experimentally [68], and so it is likely that the H-atoms on dust grains will be 'physisorbed'. If the H-atoms are physisorbed, diffusion across the surface will be easier and hence, the LH formation mechanism again may dominate.

1.8. Previous Work

Interest in the formation of H_2 on interstellar dust has resulted in a number of theoretical and experimental investigations of this system. Many of these have been theoretical/computational studies [11-15, 17, 18, 20, 24, 26-28, 32, 36, 39, 40, 42, 43, 64, 65] but more recently, a number of experiments have been set-up to probe the reaction [21, 22, 33-35, 37, 38, 44, 68-72]. Both theoretical and experimental studies of H_2 formation in the ISM will be reviewed in the next section.

1.8.1. Theoretical Studies

Early theoretical studies by Gould and Salpeter [17] showed that H_2 recombination on 'dirty ice' type grains could be efficient for surface temperatures between 10-20 K. These calculations were improved upon by Hollenbach and Salpeter [20] who concluded that hydrogen recombination on grains with temperatures below ~25 K would be almost 100% efficient.

Most of the more recent theoretical studies of H_2 formation in the ISM have concentrated on the formation mechanism and on the type of surface. Parniex and Bréchignac [32] carried out a molecular dynamics study of the Eley-Rideal mechanism for H_2 formation on an ideal graphitic surface. They found that the nascent H_2 molecules desorbed from the surface with large translational energy and also in highly excited vibrational states.

A density functional theory (DFT) study by Jeloaica and Sidis [65] of the adsorption of H atoms on a coronene-like model of graphite showed a significant barrier to chemisorption on this type of surface, of the order of 0.2 eV. They found that the chemisorption site was located at an 'on-top' site of a carbon atom and that, in order for chemisorption to occur, significant surface relaxation was required. The physisorption region however, was site independent and compatible with a high mobility of H-atoms on the surface. The results of these calculations determined that the ER mechanism for H_2 formation could occur for both chemisorbed and physisorbed H atoms but the LH mechanism could only occur for physisorbed H atoms, as the chemisorbed atoms were restricted from diffusing across the surface.

Farebrother *et al* have studied the formation of H_2 on graphite *via* an Eley-Rideal mechanism, involving chemisorbed H-atoms. This group used DFT to create a potential energy surface (PES) on which they performed time-independent quantum reactive scattering calculations. In one study [15], they determined that H_2 was formed on the surface in high vibrational levels, with $v = 2$ being highly populated. This initial study did not consider rotational excitation of the product H_2 molecules but a further '3D' study did consider rotational degrees of freedom [25]. This latter study found the product molecules had less vibrational energy but there was significant rotational excitation, with maxima around $J = 14$. However, this '3D' study did not allow any surface relaxation and both studies assumed chemisorbed H-atoms on the surface, reacting *via* the ER mechanism.

Meijer *et al* have also looked at isotope effects in the formation of molecular hydrogen on a graphite surface, *via* the Eley-Rideal mechanism [66]. In this study, a time-dependent wave packet method was used for the calculations which looked at the associative desorption of HD(v,J) and D_2(v,J). The group found that the product molecules were ro-vibrationally excited and translationally hot, and also determined significant isotope effects and possible resonant transitions during the recombination reaction. A further study by the same group was performed to investigate the effect that other light atoms or molecules adsorbed on the graphite surface have on the

internal energy of a newly formed H_2 molecule, again *via* the ER mechanism [26]. The workers found that, in contrast to previous studies in which they ignored any other species on the surface, the highest excited states of the newly formed molecule was between $v = 2$ and $v = 3$.

A molecular dynamics study by Rutigliano [39] and co-workers also looked at H-atom recombination on graphite at 10 K *via* the ER mechanism. They varied the collision energy of the gas-phase H-atom with that on the surface and also found that the product H_2 was formed in highly vibrationally excited levels.

Jackson and Lemoine [64] have looked at the ER reaction mechanism for H-atoms adsorbed on a variety of surfaces, both metal and graphite. This study found that the collision cross-sections for the single-collision ER mechanism on metal surfaces were small, suggesting hot-atom processes are important for H_2 formation. However, for graphite surfaces, they found that the cross-sections were generally large for the reaction of $H_{(g)}$ with H adsorbed on the surface.

Sha and co-workers have also studied the ER reaction between H atoms on a graphite surface by electronic structure studies and quantum scattering calculations [40]. This group looked at H-atoms that were originally chemisorbed and physisorbed before reacting with an H-atom from the gas phase. The study considered two scenarios for the chemisorbed case: (a) where the graphite lattice is held fixed in a puckered position during the reaction and (b) where the lattice is allowed to fully relax. The group found the reaction cross sections to be 'large' except for two cases. Firstly, when the H-atom was chemisorbed, there was a small barrier in the entrance channel, making the reaction cross-section go to zero for small incident energies. Secondly, for the physisorbed H-atom, the reaction cross-section dropped rapidly as the incident energy of the approaching gas phase atom increased. They found that all the reactions led to sizeable vibrational excitation but little rotational excitation. The study also found that, although there was ~1 eV of

translational energy for H_2 that had formed from the chemisorbed state, product molecules from the physisorbed state had almost zero translational energy.

A further study by Sha *et al* used DFT calculations to look at the trapping of H-atoms on a graphite surface [41]. The group found that a significant fraction of H and D atoms can be trapped on the surface, at energies above 0.2 eV. By extrapolating their results, this group was able to conclude that H atoms should have a sticking probability on graphite on the order of 0.1.

Ree and co-workers have looked at the formation of vibrationally excited H_2 on graphite [24] and also studied the dynamics of H_2 formation on graphite [36]. In their first study, they used a classical dynamics calculation to investigate the ER mechanism of H_2 formation on graphite, looking at both strong (chemisorption) and weak (physisorption) interactions between the H-atoms and the surface. They found that, for chemisorbed H-atoms, the maximum vibrational energy of the desorbed molecules was distributed between $v = 0$ and $v = 3$. For the physisorbed atoms, the resulting molecules were released with much higher internal energy. A similar result was found in a second study, with high vibrational energy in the resultant molecules formed by reaction of a gas phase atom with a physisorbed H-atom on a graphite surface.

Cazaux and Tielens have modelled H_2 formation on 'grain surfaces' under 'astrophysically relevant conditions' [13, 14]. This group found that H_2 can form efficiently on such grains over a range of surface temperatures, from ~6 K to ~300 K. They determined that up to ~100 K, H_2 forms by recombination of a physisorbed H atom with a chemisorbed H atom and that this process is highly efficient. At higher temperatures, it was found that physisorbed H atoms desorbed from the surface too quickly to react and form H_2, and that two chemisorbed H-atoms were required to form molecular hydrogen. This reaction between two chemisorbed H-atoms was found to be less efficient than the reaction between a physisorbed and chemisorbed atom [13]. These workers have also developed a

model for hydrogen formation on grain surfaces which takes into account physisorbed and chemisorbed atoms and also quantum mechanical diffusion and thermal hopping, and compared their results with the experiments of Pironello *et al* [33-35]. They found that the time evolution of the system was governed by binding energies and barriers against the diffusion of the adsorbed species. At low temperatures, physisorbed H-atoms reacting with trapped, i.e. chemisorbed, H-atoms was found to be highly efficient; while at higher temperatures the chemisorbed atoms became mobile and could recombine. Both these studies therefore investigate the efficiency of the LH mechanism for H_2 formation on grains.

A number of studies by Morisset and co-workers have looked at the formation of H_2 on graphite, both *via* the Eley-Rideal and Langmuir-Hinshelwood mechanisms [27-30]. This group have considered both the dynamics of the reaction [27, 28, 30] and the role of surface relaxation [29]. For the ER studies, it was found that a large amount of the energy released upon formation of H_2 goes into vibrational modes of the molecule, with the maximum populated vibrational level around $v = 7$. The LH study considered H-atoms, which were initially physisorbed on the surface, diffusing across the surface and reacting before desorbing as H_2. Again, it was determined that a large amount of the energy of formation goes into vibration of the H_2 molecule.

It is important to note with all the theoretical studies, that the grain surfaces are modelled as 'perfect' or 'ideal' grains, which will affect the accuracy of the results when applied to the conditions in the ISM, and also when compared with experimental results.

1.8.2. Experimental Studies

A number of experimental investigations into the formation of molecular hydrogen in the ISM have been carried out by Pirronello and co-workers [23, 33-35, 37, 38, 44]. This group have looked at both silicate surfaces, modelled by an olivine

sample, amorphous carbon surfaces and, more recently, amorphous water-ice surfaces.

Pirronello *et al* initially looked at the recombination rate of hydrogen on olivine, a silicate surface [34], carrying out temperature programmed desorption (TPD) experiments. The experiments they performed involved studying the formation of HD, using two atom beams, one of radio frequency dissociated H_2 and one of radio frequency dissociated D_2. This method allows a background-free measurement, preventing undissociated H_2 (or D_2) from the source affecting the results since the only source of HD in the chamber will be that which has formed on the surface. The measurements gave a lower recombination efficiency (defined as the sticking probability, s, of an H atom on the surface multiplied by the probability of recombination upon H-H encounter, γ) than model-based estimates. These workers found that the recombination efficiency increased as the surface temperature of the sample was decreased, however, their result at astrophysically relevant grain temperatures of 10-15 K was ~0.03-0.05, much lower than the result determined by Hollenbach and Salpeter of 0.3 [20]. Pirronello *et al* proposed that their results could be reconciled with average estimates of the recombination rate if they assumed that the surface of an average grain is much rougher and has a larger surface area than that considered in models.

A follow up study by Pirronello and co-workers, again carried out on an olivine slab as a function of surface temperature, found that there are two main regimes of H coverage that are astrophysically important [33]. These are low coverage (at low surface temperatures) and higher coverage (below monolayer coverage). In the low coverage regime, the desorption kinetics were found to be second order, implying that the atoms remain on the surface as atoms, and also remain localised without recombining. The higher coverage regime was found to exhibit first order desorption kinetics, implying that molecular hydrogen that has formed at a low temperature does not desorb until the temperature is raised. This suggests that the ~4.5 eV of binding energy released on formation of H_2 does not necessarily restore

the H_2 immediately to the gas phase, and a considerable amount of energy may be deposited into the surface.

A study of molecular hydrogen formation on 'carbonaceous grains' was also carried out by the Pirronello group [24]. As in the case with olivine, they found that HD recombination was thermally activated. However, they also found that the required activation temperature was significantly higher than on olivine and also that the recombination efficiency was higher, despite the experiments being carried out under the same conditions as the olivine experiments. They determined that, although the energy barrier for H_2 formation on carbonaceous surfaces was slightly higher than olivine, H is more strongly bound to a carbonaceous surface than an insulating surface, such as a silicate. Hence, the residence time of H atoms will be longer on the carbonaceous surface, allowing them to overcome the barrier for recombination if they have enough energy.

Pirronello *et al* have also developed a rate equation model to analyse the results of their experiments to form H_2 (HD) on olivine and amorphous carbon surfaces [23]. The workers assumed that the mechanism of formation was the LH mechanism and therefore that the creation of H_2 was diffusion-limited. They found that a model in which HD desorbed from the surface immediately upon formation could not reproduce the experimental desorption curves. A difference in recombination efficiency for the silicate surface compared with the amorphous carbon surface was also determined, with the silicate surface being efficient at much lower temperatures than are astrophysically important in interstellar clouds. The amorphous carbon surfaces however were found to enable most efficient hydrogen recombination at temperatures of ~8-14 K, much more astrophysically relevant grain temperatures.

More recently, the Pirronello group have looked at the influence of amorphous water ice on the formation of molecular hydrogen [37, 38]. In the first study, [37], both low density and high density amorphous ice were considered. Low density amorphous-ice has a density of 0.94 ± 0.03 g cm^{-3} and can be obtained by depositing

water vapour on an inert surface at 77 K. This low density type of amorphous ice has been found to be microporous in nature, increasing the effective surface area of the film. High density amorphous water-ice, 1.1 ± 0.1 g cm^{-3} was obtained by depositing water vapour on a substrate held at ~10 K. These workers found that the recombination efficiency of hydrogen on this surface was affected by the structure of the ice surface, that is whether the surface was low density or high density ice, and that the difference in recombination efficiency increased when the surface temperature was ~10 K. They concluded that H_2 formation could be more efficient on low density amorphous water-ice. The second study [38] looked at the kinetic energy of D_2 molecules that desorbed from amorphous water ice, using TPD data. The group deduced from their data that the molecules desorb from the ice surface as if they were thermally accommodated.

Gough *et al* have studied the formation of vibrationally excited hydrogen molecules (H_2) on carbon surfaces at temperatures ranging from 90 – 300 K [16]. This group found that molecular hydrogen could form in vibrationally excited states and detected it in states up to $v = 7$. These experiments used a technique based on 'dissociative attachment of low energy electrons to ro-vibrationally excited H_2'. The workers looked at the H^- ion yield from dissociative attachment of electrons to $H_2(v, J)$. Although the temperatures considered are much higher than grain temperatures in the ISM, they concluded that H_2 could be expected to form ro-vibrationally excited on the surfaces of dust grains in interstellar space.

Zecho *et al* have carried out a series of experimental studies investigating the ER mechanism of H_2 (HD) formation on HOPG in the laboratory, using the surface science techniques of thermal desorption spectroscopy (TDS), electron energy loss spectroscopy (EELS) and high-resolution electron energy-loss spectroscopy [68, 71]. In these experiments Zecho *et al* employed 2000 K H(D) atom sources in order to obtain chemisorbed atoms on the graphite surface. In one group of experiments chemisorbed D atoms were reacted with a beam of incident H-atoms and the HD product was monitored with a quadrupole mass spectrometer at a surface

temperature of 150 K. These experiments determined initial sticking coefficients for H and D atoms of 0.4 ± 0.2 and confirmed the existence of the 0.2 eV barrier to chemisorption that had been calculated theoretically. A further study by this group investigated the effect of adsorbed water on the graphite surface on the ER reaction of H with D atoms [72]. These experiments showed that a water monolayer prevented adsorption of 2000 K H-atoms onto the surface and that an overlayer of water above a chemisorbed layer of D atoms also prevented reaction. This group have also used low energy electron diffraction (LEED) and scanning tunnelling microscopy (STM) to look at the adsorption of H and D atoms on graphite [70] and have looked at the adsorption of H and D atoms on surfaces that have been bombarded with Ar ions [69]. The LEED study showed that the atoms adsorb randomly on the surface. The STM study showed randomly distributed C atoms puckered out of the plane on surfaces which were covered in D-atoms, as predicted by theory. A further TDS study, also by Zecho and co-workers, looked at the adsorption of chemisorbed D-atoms on terraces and terrace edges of HOPG and natural graphite surfaces [73]. From this study, the group found that the desorption spectra of D-atoms adsorbed on (0001) terraces showed 2 peaks and a shoulder which were intrinsic to D-atoms on terraces and not related to any defects in the surface. They also determined that reaction occurred between the D-atoms and the graphite at the terrace edge, resulting in the formation of hydrocarbons which then desorbed in the TDS runs.

Hornekaer *et al* have investigated the influence of the morphology of the surface on both H_2 formation in the ISM and on D_2 desorption kinetics, using TPD techniques. In both studies, the surface consisted of films of amorphous solid water (ASW) on a copper substrate [21, 22]. This group found that the morphology of the ice surface had a significant effect on what happens to the binding energy released on the formation of H_2. The TPD data showed a large HD signal obtained from a porous ice surface, however when the surface was non-porous, little or no HD signal was observed in the mass spectrum. These results were explained by HD molecules that had formed in the porous structure, thermalising with the surface within the pores

and then desorbing when the surface temperature was raised in the TPD run. For non-porous surfaces, the workers inferred from the lack of HD signals in the mass spectrum, that the molecules which had formed were not trapped on the surface. They concluded that these molecules had immediately desorbed upon formation, probably in highly vibrationally and rotationally excited states.

Perry and co-workers have designed and commissioned the experiment used in this laboratory to investigate the ro-vibrational distribution of H_2 molecules formed on a cold (30-50 K) HOPG surface [74, 75]. Using the laser technique of resonance enhanced multiphoton ionisation (REMPI), they successfully measured H_2 formed in ro-vibrationally excited states v = 1, J = 0-3. The excited molecules were determined to have rotational temperatures much higher than the temperature of the surface on which they were formed. The results also suggested that a considerable proportion of the binding energy released on the formation of H_2 was deposited into the HOPG surface. These results compare reasonably well with aspects of both the results of the Pirronello group and the Hornekaer group. The result that some of the energy is deposited into the surface is in agreement with the result from the Pirronello group that the molecules do not desorb immediately on formation [33]. However, the detection of ro-vibrationally excited molecules suggests that some of the molecules must desorb immediately on formation, as proposed by the results from the Hornekaer group for non-porous surfaces [21].

Prior to the experiments of Pirronello and co-workers, and to all the subsequent studies reviewed above, experiments on the adsorption of hydrogen on cold (4 K) surfaces were carried out by Govers *et al* [76], although not initially with the idea of applying the results to the chemistry of the ISM. This group used molecular beams of H_2 and D_2, incident on a liquid helium cooled (4 K) bolometer as an energy detector, to investigate the sticking and accommodation of molecular hydrogen and deuterium on low temperature substrates. The workers also investigated the recombination of atomic hydrogen physisorbed on low temperature substrates, taking into account the surface coverage of molecular hydrogen [77]. These workers

were able to extract the sticking probability and accommodation coefficient of H_2 on the cryodeposit on the bolometer surface as a function of H_2 coverage. These results were obtained by monitoring the energy deposited in the bolometer as a function of time, and the associated temporal behaviour of the nascent H_2 signal monitored by a mass spectrometer. Similarly when H atoms were incident on a surface pre-dosed with D_2, the sticking probability and reaction probability of the incident atoms were determined as a function of D_2 coverage. In contrast to the results of the Pirronello group, Govers and co-workers found that atomic hydrogen is highly mobile on a surface, even at temperatures as low as 4 K, and that recombination also occurred at this low temperature. This result therefore throws doubt on the assumption by the Pirronello group that any H or D-atoms adsorbed on their surface at a temperature of ~4 K will be immobile on the surface, and that no reaction can occur until they begin heating the surface in the TPD experimental runs. This result also further backs up the interpretation of the experiments of Hornekaer *et al* in that they observe a much reduced HD signal from their non-porous surface. If, in the experiments of Hornekaer *et al*, the atoms have recombined and desorbed at the low surface temperature, no signal would be expected in the mass spectrum when the TPD run is performed.

1.9. The UCL Cosmic Dust Experiment

As has been shown in the previous sections, there are still a large number of questions to be answered about the formation of molecular hydrogen on interstellar dust grains. In particular, there is little experimental data on how the ~4.5 eV of binding energy is distributed when H_2 forms. For example, how much of this binding energy goes into rotational, vibrational or translational excitation of the product and how much is deposited into the grain? These questions may have a significant impact on the energy budget and chemistry of interstellar clouds. For example, faster reaction rates may occur for reactions with H_2 molecules in vibrational levels higher than the ground vibrational level. Highly excited H_2 will also be easier to ionise, either directly or by charge transfer with H^+, which is usually

an endothermic reaction. This may lead to further routes for the formation of H_3^+, an important interstellar ion as described in section 1.3. In fact, the abundance of H_3^+ in diffuse interstellar clouds is also a problem for astronomers as 'surprisingly large' column densities of H_3^+ have been detected in the diffuse ISM [78]. It has been proposed that an enhanced rate of H_2 ionisation may be able to account for this increased H_3^+ abundance [78], which may be possible if the H_2 molecules are formed vibrationally excited. Other possible suggestions for the enhanced H_3^+ abundance in the diffuse ISM are a reduced electron fraction and a smaller value for the H_3^+ dissociative recombination rate constant than implied by laboratory experiments [78]. Furthermore, large amounts of translational energy in the H_2 molecules may result in localised heating of interstellar clouds through inelastic scattering.

The UCL cosmic dust experiment has been constructed over the past seven years and is now starting to produce results of interest to astronomers. The experiment has been designed to probe the ro-vibrational distribution of H_2, and other small molecules, which have formed on the surfaces of cosmic dust grain analogues. The experiment uses the well established laser technique of resonance enhanced multiphoton ionisation (REMPI), and the detection technique of time-of-flight (TOF) mass spectrometry, to state-selectively ionise and detect the newly formed H_2 molecules. The experiments are carried out under conditions designed to mimic those of the interstellar medium.

1.10. Summary

This chapter has introduced the background to the UCL Cosmic Dust experiment. It has given an overview of what is currently known in the field of astrochemistry and highlighted the need for more experimental data, particularly on the formation of molecular hydrogen in the ISM.

The following chapters will describe the experimental apparatus, including improvements to the original design [74], and new results that describe the internal energy distribution of molecular hydrogen which has formed on graphite, under conditions designed to mimic those of interstellar space.

1.11. References

1. Dyson, J.E. and Williams, D.A., *The Physics of the Interstellar Medium*. 2 ed. 1997: Institute of Physics publishing. 165.

2. Hartquist, T.W. and Williams, D.A., *The Chemically Controlled Cosmos*. 1 ed. 1995: Cambridge University Press. 169.

3. Field, G.B., Somervil.Wb, and Dressler, K., *Annu. Rev. Astron. Astrophys.*, 1966. **4**: p. 207-&.

4. Carruthers, G.R., *Astrophys. J*, 1970. **161**: p. L81-L85.

5. Spitzer, L. and Jenkins, E.B., *Annual Review of Astronomy and Astrophysics*, 1975. **13**: p. 133-164.

6. Gautier III, T.N., Fink, U., Treffers, R.R., and Larson, H.P., *Astrophys. J*, 1976. **207**: p. L129-L133.

7. Treffers, R.R., Fink, U., Larson, H.P., and Gautier III, T.N., *Astrophys. J*, 1976. **209**: p. 793-799.

8. Richter, P., Bluhm, H., Marggraf, O., and Boer, K.S.D. *H_2 absorption line measurements with ORFEUS.* in *Molecular Hydrogen in Space*. 2000: Cambridge University Press: p. 165.

9. Duley, W.W. and Williams, D.A., *Interstellar Chemistry*. London ed. 1984: Academic Press.

10. Baulch, D.L., Cobos, C.J., Cox, R.A., Esser, C., Frank, P., Just, T., Kerr, J.A., Pilling, M.J., Troe, J., Walker, R.W., and Warnatz, J., *J. Phys. Chem. Ref. Data*, 1992. **21**(3): p. 411-734.

11. Biham, O., Furman, I., Katz, N., Pirronello, V., and Vidali, G., *Mon. Not. Roy. Astron. Soc.*, 1998. **296**(4): p. 869-872.

12. Cazaux, S. and Tielens, A., *Astrophys. J.*, 2002. **577**(2): p. L127-L127.

13. Cazaux, S. and Tielens, A., *Astrophys. J.*, 2002. **575**(1): p. L29-L32.

14. Cazaux, S. and Tielens, A., *Astrophys. J.*, 2004. **604**(1): p. 222-237.

15. Farebrother, A.J., Meijer, A., Clary, D.C., and Fisher, A.J., *Chem. Phys. Lett.*, 2000. **319**(3-4): p. 303-308.

16. Gough, S., Schermann, C., Pichou, F., Landau, M., Cadez, I., and Hall, R.I., *Astron. Astrophys.*, 1996. **305**(2): p. 687-693.

17. Gould, R.J. and Salpeter, E.E., *Astrophys. J.*, 1963. **138**: p. 393-407.

18. Gould, R.J. and Salpeter, E.E., *Astrophys. J.*, 1963. **138**(2): p. 393-&.

19. Greenberg, J.M., *Surf. Sci.*, 2002. **500**(1-3): p. 793-822.

20. Hollenbach, D. and Salpeter, E.E., *Astrophys. J.*, 1971. **163**: p. 155-164.

21. Hornekaer, L., Baurichter, A., Petrunin, V.V., Field, D., and Luntz, A.C., *Science*, 2003. **302**(5652): p. 1943-1946.

22. Hornekaer, L., Baurichter, A., Petrunin, V.V., Luntz, A.C., Kay, B.D., and Al-Halabi, A., *J. Chem. Phys.*, 2005. **122**(12): p. art. no.-124701.

23. Katz, N., Furman, I., Biham, O., Pirronello, V., and Vidali, G., *Astrophys. J.*, 1999. **522**(1): p. 305-312.

24. Kim, Y.H., Ree, J., and Shin, H.K., *Chem. Phys. Lett.*, 1999. **314**(1-2): p. 1-8.

25. Meijer, A.J.H.M., Farebrother, A.J., Clary, D.C., and Fisher, A.J., *J. Phys. Chem. A*, 2001. **105**(11): p. 2173-2182.

26. Meijer, A.J.H.M., Fisher, A.J., and Clary, D.C., *J. Phys. Chem. A*, 2003. **107**(50): p. 10862-10871.

27. Morisset, S., Aguillon, F., Sizun, M., and Sidis, V., *Chem. Phys. Lett.*, 2003. **378**(5-6): p. 615-621.

28. Morisset, S., Aguillon, F., Sizun, M., and Sidis, V., *Phys. Chem. Chem. Phys.*, 2003. **5**(3): p. 506-513.

29. Morisset, S., Aguillon, F., Sizun, M., and Sidis, V., *J. Phys. Chem. A*, 2004. **108**(41): p. 8571-8579.

30. Morisset, S., Aguillon, F., Sizun, M., and Sidis, V., *J. Chem. Phys.*, 2004. **121**(13): p. 6493-6501.

31. Morisset, S., Aguillon, F., Sizun, M., and Sidis, V., *J. Chem. Phys.*, 2005. **122**(19): p. art. no.-194702.

32. Parneix, P. and Brechignac, P., *Astron. Astrophys.*, 1998. **334**(1): p. 363-375.

33. Pirronello, V., Biham, O., Liu, C., Shen, L.O., and Vidali, G., *Astrophys. J.*, 1997. **483**(2): p. L131-L134.

34. Pirronello, V., Liu, C., Shen, L.Y., and Vidali, G., *Astrophys. J.*, 1997. **475**(1): p. L69-L72.

35. Pirronello, V., Liu, C., Roser, J.E., and Vidali, G., *Astron. Astrophys.*, 1999. **344**(2): p. 681-686.

36. Ree, J., Kim, Y.H., and Shin, H.K., *Chem. Phys. Lett.*, 2002. **353**(5-6): p. 368-378.

37. Roser, J.E., Manico, G., Pirronello, V., and Vidali, G., *Astrophys. J.*, 2002. **581**(1): p. 276-284.

38. Roser, J.E., Swords, S., Vidali, G., Manico, G., and Pirronello, V., *Astrophys. J.*, 2003. **596**(1): p. L55-L58.

39. Rutigliano, M., Cacciatore, M., and Billing, G.D., *Chem. Phys. Lett.*, 2001. **340**(1-2): p. 13-20.

40. Sha, X.W., Jackson, B., and Lemoine, D., *J. Chem. Phys.*, 2002. **116**(16): p. 7158-7169.

41. Sha, X.W., Jackson, B., Lemoine, D., and Lepetit, B., *J. Chem. Phys.*, 2005. **122**(1): p. art. no.-014709.

42. Sha, X.W. and Jackson, B., *Surf. Sci.*, 2002. **496**(3): p. 318-330.

43. Takahashi, J., Masuda, K., and Nagaoka, M., *Mon. Not. Roy. Astron. Soc.*, 1999. **306**(1): p. 22-30.

44. Vidali, G., Roser, J.E., Manico, G., and Pirronello, V., *Experimental study of the formation of molecular hydrogen and carbon dioxide on dust grain analogues*, in *Space Life Sciences: Steps toward Origin(S) of Life*. 2004. p. 6-13.

45. Millar, T.J. and Williams, D.A., *Dust and Chemistry in Astronomy*. 1 ed. Graduate Series in Astronomy, ed. R.E.W. R J Tayler. 1993: Institute of Physics. 335.

46. Williams, D.A. and Herbst, E., *Surf. Sci.*, 2002. **500**(1-3): p. 823-837.

47. Hiraoka, K., Ohashi, N., Kihara, Y., Yamamoto, K., Sato, T., and Yamashita, A., *Chem. Phys. Lett.*, 1994. **229**(4-5): p. 408-414.

48. Hiraoka, K., Sato, T., and Takayama, T., *Science*, 2001. **292**(5518): p. 869-870.

49. Fraser, H.J., Collings, M.P., McCoustra, M.R.S., and Williams, D.A., *Mon. Not. Roy. Astron. Soc.*, 2001. **327**(4): p. 1165-1172.

50. Fraser, H.J., Collings, M.P., and McCoustra, M.R.S., *Rev. Sci. Instrum.*, 2002. **73**(5): p. 2161-2170.

51. Collings, M.P., Dever, J.W., Fraser, H.J., and McCoustra, M.R.S., *Astrophys. Space Sci.*, 2003. **285**(3-4): p. 633-659.

52. Collings, M.P., Dever, J.W., Fraser, H.J., McCoustra, M.R.S., and Williams, D.A., *Astrophys. J.*, 2003. **583**(2): p. 1058-1062.

53. Fraser, H.J. and van Dishoeck, E.F., *SUIRFRESIDE: a novel experiment to study surface chemistry under interstellar and protostellar conditions*, in *Space Life Sciences: Steps toward Origin(S) of Life*. 2004. p. 14-22.

54. Hidaka, H., Watanabe, N., Shiraki, T., Nagaoka, A., and Kouchi, A., *Astrophys. J.*, 2004. **614**(2): p. 1124-1131.

55. Viti, S., Collings, M.P., Dever, J.W., McCoustra, M.R.S., and Williams, D.A., *Mon. Not. Roy. Astron. Soc.*, 2004. **354**(4): p. 1141-1145.

56. Collings, M.P., Anderson, M.A., Chen, R., Dever, J.W., Viti, S., Williams, D.A., and McCoustra, M.R.S., *Mon. Not. Roy. Astron. Soc.*, 2004. **354**(4): p. 1133-1140.

57. Watanabe, N., Nagaoka, A., Shiraki, T., and Kouchi, A., *Astrophys. J.*, 2004. **616**(1): p. 638-642.

58. Hiraoka, K., Wada, A., Kitagawa, H., Kamo, M., Unagiike, H., Ueno, T., Sugimoto, T., Enoura, T., Sogoshi, N., and Okazaki, S., *Astrophys. J.*, 2005. **620**(1): p. 542-551.

59. Fraser, H.J., Bisschop, S.E., Pontoppidan, K.M., Tielens, A., and van Dishoeck, E.F., *Mon. Not. Roy. Astron. Soc.*, 2005. **356**(4): p. 1283-1292.

60. Bolina, A.S., Wolff, A.J., and Brown, W.A., *J. Chem. Phys.*, 2005. **122**(4): p. art. no.-044713.

61. Bolina, A.S., Wolff, A.J., and Brown, W.A., *J. Phys. Chem. B*, 2005. **109**(35): p. 16836-16845.

62. Li, A.G. and Greenberg, J.M., *Astron. Astrophys.*, 1997. **323**(2): p. 566-584.

63. Mathis, J.S., Rumpl, W., and Nordsieck, K.H., *Astrophys. J.*, 1977. **217**(2): p. 425-433.

64. Jackson, B., *Abstr. Pap. Am. Chem. Soc.*, 2001. **221**: p. 36-COLL.

65. Jeloaica, L. and Sidis, V., *Chem. Phys. Lett.*, 1999. **300**(1-2): p. 157-162.

66. Meijer, A.J.H.M., Farebrother, A.J., and Clary, D.C., *J. Phys. Chem. A*, 2002. **106**(39): p. 8996-9008.

67. Pirronello, V., Biham, O., Manico, G., Roser, J.E., and Vidali, G. *Laboratory studies of Molecular Hydrogen formation on Surfaces of Astrophysical Interest.* in *H2 in Space*. 1999: p. 71-83.

68. Zecho, T., Guttler, A., Sha, X.W., Jackson, B., and Kuppers, J., *J. Chem. Phys.*, 2002. **117**(18): p. 8486-8492.

69. Guttler, A., Zecho, T., and Kuppers, J., *Surf. Sci.*, 2004. **570**(3): p. 218-226.

70. Guttler, A., Zecho, T., and Kuppers, J., *Chem. Phys. Lett.*, 2004. **395**(1-3): p. 171-176.

71. Zecho, T., Guttler, A., Sha, X.W., Lemoine, D., Jackson, B., and Kuppers, J., *Chem. Phys. Lett.*, 2002. **366**(1-2): p. 188-195.

72. Zecho, T., Guttler, A., and Kuppers, J., *Chem. Phys. Lett.*, 2003. **370**(3-4): p. 366-370.

73. Zecho, T., Guttler, A., and Kuppers, J., *Carbon*, 2004. **42**(3): p. 609-617.

74. Perry, J.S.A., Gingell, J.M., Newson, K.A., To, J., Watanabe, N., and Price, S.D., *Meas. Sci. Technol.*, 2002. **13**: p. 1414-1424.

75. Perry, J.S.A. and Price, S.D., *Astrophys. Space Sci.*, 2003. **285**(3-4): p. 769-776.

76. Govers, T.R., Mattera, L., and Scoles, G., *J. Chem. Phys.*, 1980. **72**(10): p. 5446-5455.

77. Govers, T.R., Mattera, L., and Scoles, G., J. *presented at the Astrosurf Meeting, University College London, April 18-19, 2005, and to be published (see: http://www.chem.ucl.ac.uk/astrosurf/challenges/programme.html and http://hal.ccsd.cnrs.fr/ccsd-00004273/en/).*

78. McCall, B.J., Hinkle, K.H., Geballe, T.R., Moriarty-Schieven, G.H., Evans, N.J., Kawaguchi, K., Takano, S., Smith, V.V., and Oka, T., *Astrophys. J.*, 2002. **567**(1): p. 391-406.

1.12.

Chapter 2. Experimental Apparatus

2.1. Overview

The UCL cosmic dust experiment has been designed to probe the internal ro-vibrational energy distribution of hydrogen, and other small molecules, that have formed on the surfaces of cosmic dust grain analogues. The importance of measuring this distribution has already been described in Chapter 1. In this experiment, a single H-atom beam or two beams, one of H-atoms and a one of D-atoms, are directed onto a surface analogous to cosmic dust. These atoms then recombine to form H_2, D_2 or HD, through one of the surface mechanisms described in Chapter 1, either the Eley-Rideal or Langmuir Hinshelwood mechanisms or variants thereof.

It is not possible to use actual interstellar dust grains and so the surface used in these experiments is highly oriented pyrolitic graphite (HOPG). HOPG is a well defined and high purity graphite surface. This surface is used in order to mimic the carbonaceous grains found in the ISM, to a first approximation, and to compare our experimental results with theoretical calculations of H_2 formation on the same surface. The dimensions of the HOPG sample used are 10 mm × 20 mm × 2 mm (Goodfellows Ltd. UK). The mosaic spread of the sample used is 3.5° ± 1.5°. The mosaic spread refers to how ordered the atomic layers in the graphite are with respect to each other, hence a more ordered sample has a lower mosaic spread. The layered structure of the graphite means it is easy to cleave, to give a fresh surface for new experiments (see Figure 2.1)

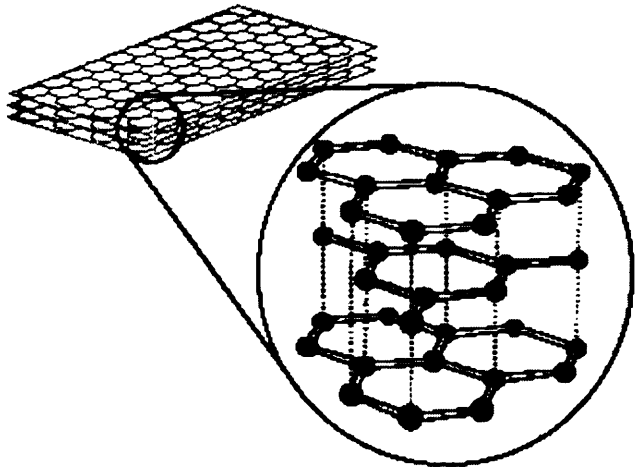

Figure 2.1. Diagram to show the layered structure of a HOPG sample. Taken from: http://www.chem.wisc.edu/~newtrad/CurrRef/BDGTopic/BDGtext/BDGGraph.html.

The experiment uses the well established laser technique of Resonance Enhanced Multi-Photon Ionisation (REMPI) in order to ionise the newly formed molecules from a particular (v,J) ro-vibrational quantum state [1]. This laser technique will be described in detail in Chapter 3. The ions formed are then detected using time-of-flight mass spectrometry (TOFMS), which will be described in this Chapter. The experiments are carried out under conditions designed to mimic those of the ISM, which means under ultrahigh vacuum conditions and very low grain surface temperatures (10-15 K), achieved by using cryogenic cooling methods. This chapter will describe the various parts of the experimental set-up.

The original design of the experiment [2] used one atomic beam of hydrogen. This allowed the study of H_2 molecules formed in ro-vibrationally excited states $v'' \geq 1$ but did not allow the ground vibrational state to be investigated. This was because the method used to create the H-atom beam from molecular hydrogen is not 100% efficient and so undissociated H_2 in the $v = 0$ state from the source gas could not be distinguished from any newly formed H_2 in the $v = 0$ state from the HOPG surface. Clear evidence was obtained to show that no ro-vibrationally excited $(v'' \geq 1)$ H_2 from the source gas was entering the target chamber since any ro-vibrationally excited H_2 that had formed in the source gas cell had been vibrationally relaxed

before reaching the target chamber, as described in Chapter 4 and reference [2]. Furthermore, no signal was observed for H_2 formed in $v'' \geq 1$ when the transport tube for the H-atoms was directed out of the line of sight of the laser, indicating that no ro-vibrationally excited molecular hydrogen that had formed anywhere other than on the HOPG surface could be detected by the time-of-flight mass spectrometer. Hence, it was possible to probe the distribution of the ro-vibrationally excited states of H_2 that had formed on the HOPG surface using a single H-atom beam [2, 3]. Some new results for the formation of H_2 on HOPG, which were taken prior to any of the changes to the microwave generator described below, will be discussed in Chapter 5.

During the course of this thesis, it was decided that in order to try to increase the flux of H-atoms into the target area it was necessary to purchase a more powerful microwave generator. The formation of H-atoms *via* microwave dissociation of molecular hydrogen is described in section 2.3. It was hoped that by using a more powerful microwave generator, the REMPI signals would be stronger and therefore it would be possible to detect any higher rotational states that had so far not been observed, that is, $J'' \geq 4$. This new generator, a Sairem 300 W generator, produced microwaves of a narrower bandwidth than the original generator, resulting in the energy of these microwaves being coupled much more efficiently into the source gas. This subsequently resulted in vibrationally excited molecular hydrogen ($v = 1$) entering the target chamber with the H-atom beam, making it impossible to distinguish between the signal from the source gas and that from any H_2 that had formed on the surface.

Various attempts to overcome this new problem of excited H_2 ($v'' > 0$) from the source gas beam entering the target chamber, without having been vibrationally relaxed, were unsuccessful as will be described in Chapter 4. Because of this, it was decided to adapt the apparatus to use two atomic beams, one of atomic hydrogen and one of atomic deuterium, in order to form HD on the target surface. HD cannot form in the source region as the two beams are formed in separate cells and transported in separate polytetrafluoroethylene (PTFE) lines, so the only way HD can form is

through recombination on the HOPG surface. The use of two atom beams therefore allows a background free study of HD formed ro-vibrationally excited on an HOPG surface, and also allows us to investigate any isotope effects which have been predicted theoretically [4].

This thesis will describe results obtained for both H_2 and HD formed ro-vibrationally excited on a HOPG surface under conditions similar to those of the ISM. The H_2 results were taken before the change in microwave generator, whereas all the HD results were taken with the new microwave generator in place. This chapter will describe the experimental arrangement as it currently stands, with the two atom sources in place. The improvements made to the apparatus throughout the course of this thesis will be discussed in detail and the time-of-flight (TOF) mass spectrometer will also be described. Chapter 3 will describe the laser system and the REMPI technique used to carry out the experiments. Chapter 4 will describe the commissioning of the new D-atom source.

2.2. Vacuum Set-up

The current experimental set-up is an adaptation of that described previously by Perry *et al* [2]. Currently the vacuum system consists of two ultrahigh vacuum (UHV) stainless steel chambers sealed with conflat flanges. These chambers are shown schematically in Figure 2.2. The first chamber will be referred to as the 'source chamber' since this is where the H and D atom sources are housed. The second chamber is the 'target chamber' as this is where the HOPG target is held. In the laboratory it is not possible to accurately mimic the pressure conditions in the ISM as this would require base pressures of approximately 1×10^{-13} Torr [5]. In our set-up it is possible to achieve base pressures of around 1×10^{-10} Torr without either of the atom sources in use. This is done by using turbomolecular pumps, with pumping speeds of 400 l s^{-1} backed by two-stage rotary pumps on both chambers. There is also a titanium sublimation pump (TSP) on the target chamber, as ensuring the pressure in this chamber remains as low as possible is vital to the experiments.

The pressures in the two chambers are monitored by a Penning gauge on the source chamber and an ion gauge on the target chamber.

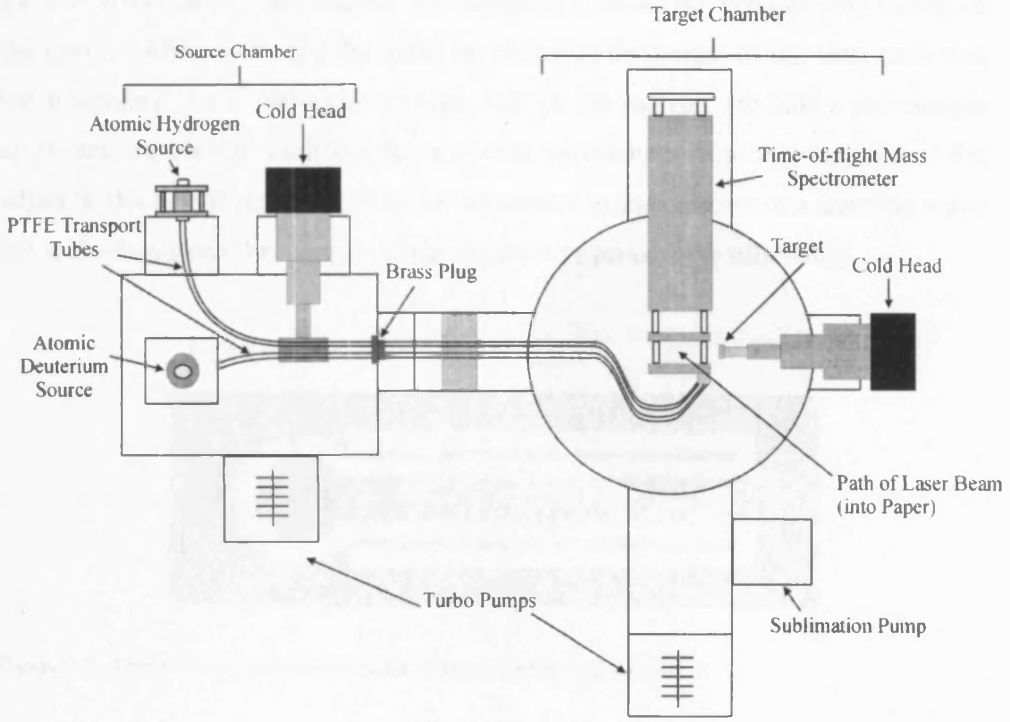

Figure 2.2. Schematic diagram of vacuum chamber set-up (not to scale).

2.3. H-atom and D-atom Generation

The hydrogen and deuterium atom beams are both produced in the same manner, *via* microwave dissociation of high purity H_2 and D_2 gases in separate Pyrex cells. The gases are piped into the Pyrex cells (260 mm long, outer diameter 25.5 mm) which are surrounded by cylindrical 2-piece slotted copper radiators, as designed by McCullough *et al* [6, 7]. The radiators are designed to fit snugly around the Pyrex cells, allowing efficient coupling of the microwaves into the gas.

The radiators operate by establishing a potential difference between the walls of the slots when the microwaves are fed into the radiator. There are two sets of slots in each half of the radiator and so the superposition of the potential differences from

the four radiator slots causes an electric field inside the Pyrex cell. The electrons in this field oscillate back and forth and cause the molecular hydrogen or deuterium gases to dissociate. The radiators are designed to avoid the need for any tuning of the cavities which surround the cells, by choosing the length of the slots such that the midpoints of the two slots on each half of the radiator are half a wavelength apart, and the ends of each slot are a quarter wavelength from the midpoint of the adjacent slot (see Figure 2.3). This set-up results in the creation of a standing wave in the discharge cell that couples in the microwave power very efficiently.

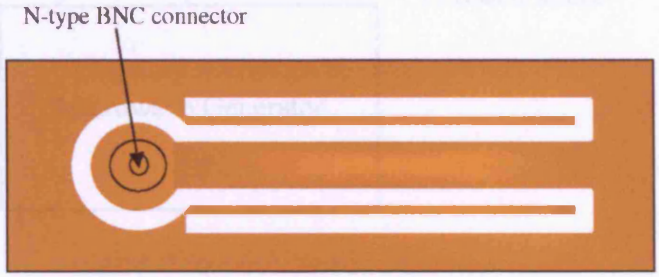

Figure 2.3. One half of a microwave radiator showing two sets of slots.

The microwaves, (2.45 GHz, 180 W), are supplied to the radiator, and hence the gases, by a Sairem microwave generator using two Sucoflex waveguides attached to each side of the radiator. Both sources are supplied with microwaves from the same generator. Any gaps around the copper radiators are sealed with copper tape to prevent any microwaves from leaking out. The radiators have water-cooled copper flanges at each end to keep the atomic discharges cool, since the probability of hydrogen recombination on Pyrex increases with temperature [8]. The copper flanges are also useful in preventing the cells from overheating due to the microwave radiation. On first use of the microwave generator, the reflected power back to the generator was around 50 %. It was found that in order to minimise this reflected power to a level below 10 %, it was necessary to connect a second, external reflected power meter to the microwave generator, from which both sets of sucoflex waveguides were connected to the sources. This set-up is shown schematically

below. Using this set-up, when the generator is set to 180 W output power, the reflected power is less than 10 %.

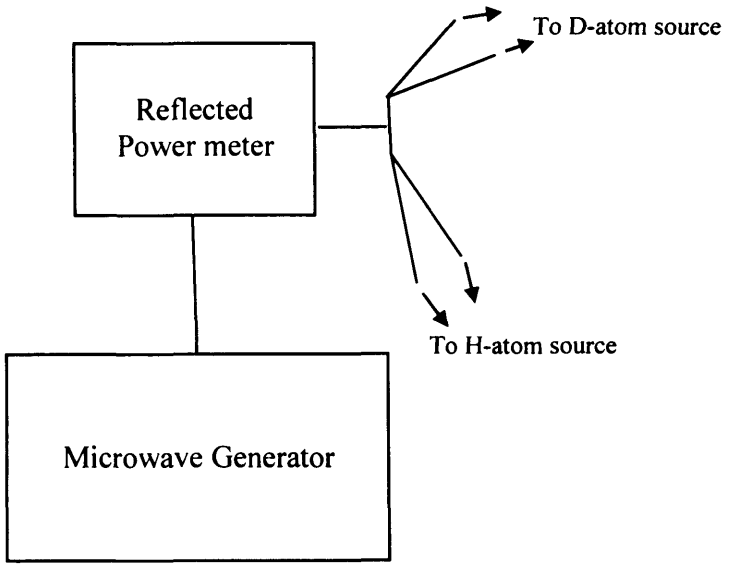

Figure 2.4. Schematic diagram showing the arrangement of the microwave generator and the external reflected power meter, resulting in a reflected power of < 10 %.

Figure 2.5 shows a schematic diagram of an atom source. H_2 and D_2 gases are piped through separate gas manifold lines into separate Pyrex cells. The tubing in the manifold is a mixture of ¼ inch PTFE, copper and glass. A Cajon o-ring seal connects the gas line tubing to the glass-to-metal seal at the top of each cell. Both gas lines can be pumped by a rotary pump.

The H and D atoms leave their respective cells through a 1 mm diameter capillary, 4 cm long, at the base of the cells and are then piped through PTFE tubing up to the target, after being differentially pumped as described in section 2.4. PTFE is used because it is known to have low recombination efficiency for hydrogen on its surface [8] and it is also safe to use under UHV conditions. Before they are installed in the experimental set-up, the cells are soaked in concentrated ortho-H_3PO_4 for at least 12 hours and then rinsed in distilled water. This process is carried out in order

to passivate the glass surface and minimise the possibility of any recombination of H or D atoms [9].

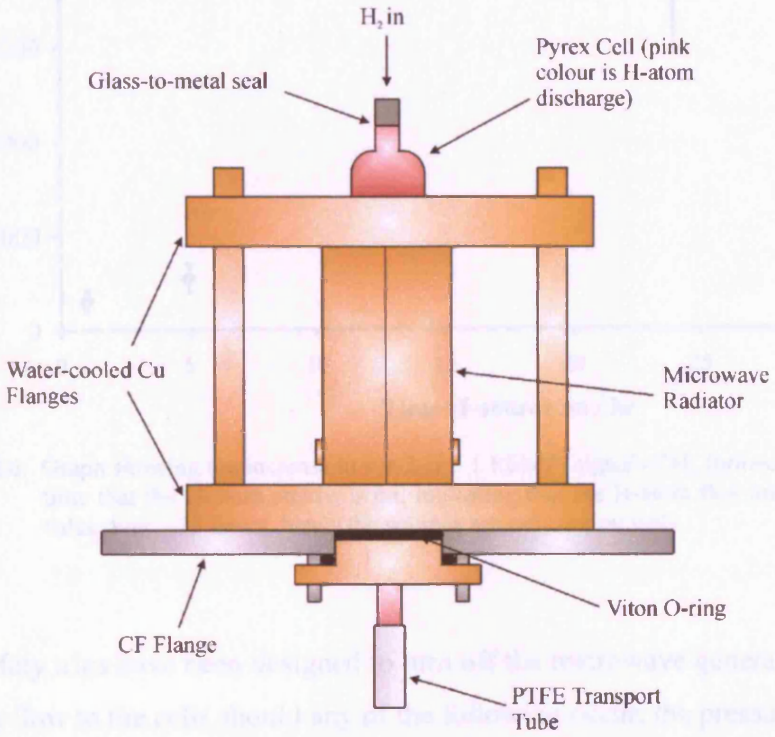

Figure 2.5. Schematic diagram of a H-atom or D-atom source.

It has been shown that the sources require 'conditioning' over 2 – 3 days to achieve optimum H or D atom production (see Figure 2.6). For this reason, the sources are run continuously with appropriate safety trips (see below) and are only turned off when it is essential.

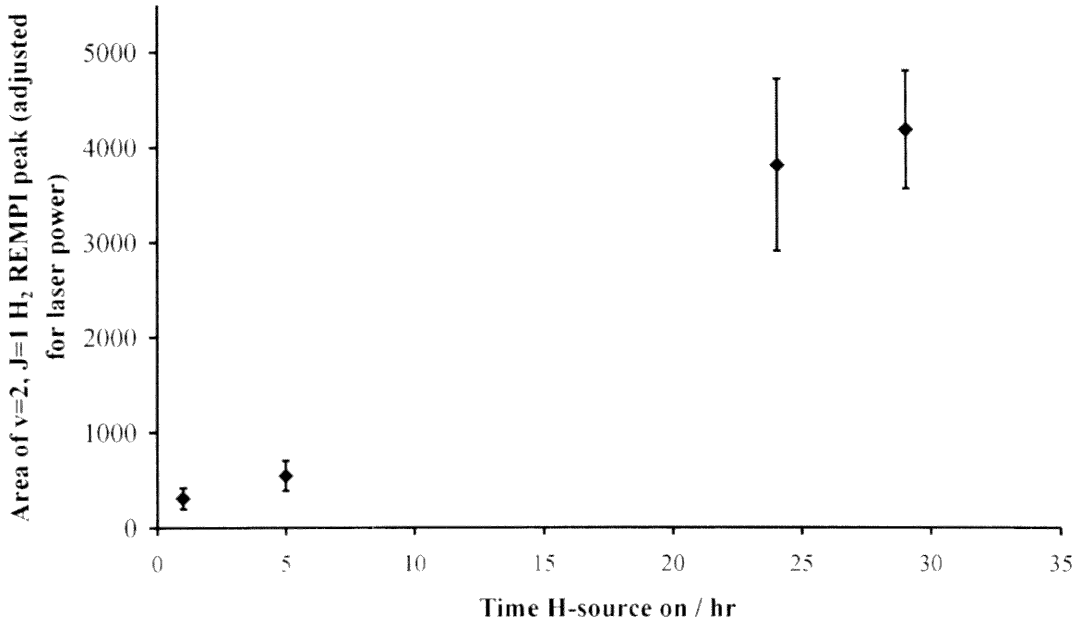

Figure 2.6. Graph showing the increase in $v = 2$, $J = 1$ REMPI signal of H_2 formed on HOPG against time that the H-atom source is on, indicating that the H-atom flux improves to a steady value over ~35 hours, hence the sources are run continuously.

The safety trips have been designed to turn off the microwave generator and shut off the gas flow to the cells should any of the following occur: the pressure in the source chamber reach $\geq 6 \times 10^{-5}$ Torr, the pressure in the target chamber reach $\geq 1 \times 10^{-5}$ Torr, the cells reach a temperature above 25 °C or the brightness of the plasma in the cells fall below a certain threshold. There are temperature and light sensors positioned on both the cells to monitor the temperature and brightness. The output from these sensors is fed to an interlock unit which uses relays to control the mains supply to the microwave generator, and also to the solenoid valves fitted to the gas lines. Should the temperature or brightness conditions fall below the optimum settings, the microwave generator and solenoid valves will be shut off. The trips can be bypassed if necessary. Figure 2.7 below shows a basic circuit diagram for one set of the safety trips.

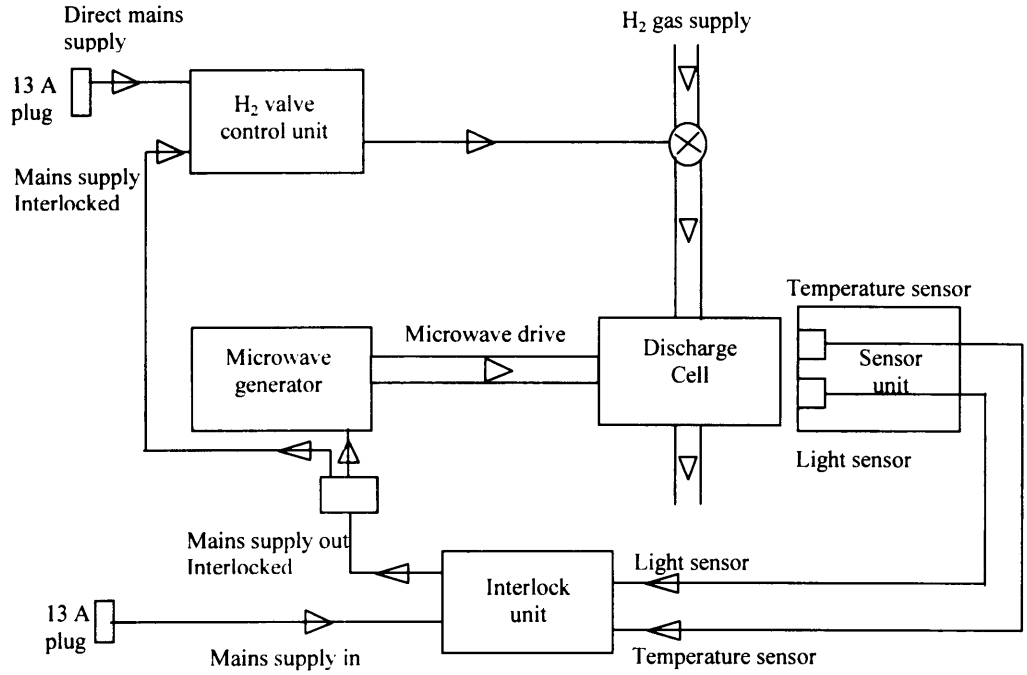

Figure 2.7. Basic circuit diagram to show set-up of safety trips on the atom sources.

2.4. Atom Beam Transport

As mentioned in section 2.3, the H and D atoms leave the cells through a narrow capillary and are piped through PTFE tubing up to the target. In the original design of the experiment, a single H-atom beam was to have impinged on the HOPG target as a pulsed, free-flight beam. This would have been achieved by the atom beam passing through a chamber equipped with tuning fork 'choppers' which would pulse the beam and allow time-resolved experiments to be performed. However, it was decided that a pulsed beam was unnecessary for determining the ro-vibrational distribution of the newly formed molecules, and was impractical for the 2-atom beam experiments. Hence, the beams are piped separately through PTFE tubing directly onto the HOPG target surface. Piping in this way also allows us to achieve sufficient atom fluxes to form reasonable amounts of H_2, HD and D_2.

The PTFE tubing leading from the capillary at the base of each cell is 6 mm outer diameter and is connected to a PTFE block, of 5 mm inner diameter by means of a PTFE plug. Originally, a cold (120 K) aluminium block was used instead of the PTFE block but this has been replaced. The reasons for this replacement will be described in Chapter 4. The results for H_2 formation described in Chapter 5 were carried out with the Al block in use. The PTFE plug has two 'pumping' holes of 2 mm diameter drilled through it which allows a large amount of the gas beam to escape into the source chamber, so that the two chambers are differentially pumped. This ensures that the pressure in the target chamber remains low whilst allowing the discharge cells to be maintained at the optimum pressure for maximum dissociation (see Chapter 4). The PTFE block is then attached to another length of PTFE tubing, of outer diameter 3 mm by a second PTFE plug. This second PTFE plug does not have any 'pumping holes' through it and the diameter of the exit aperture from the plug is 1 mm. This tubing is then passed through a hole in a brass seal which separates the source chamber from the target chamber, so that only the gas in the tube enters the target chamber. This set-up is shown in Figure 2.8. The resulting pressure in the source chamber is approximately 6×10^{-6} Torr and in the target chamber, the pressure is below $\sim 5 \times 10^{-8}$ Torr when both sources are turned on.

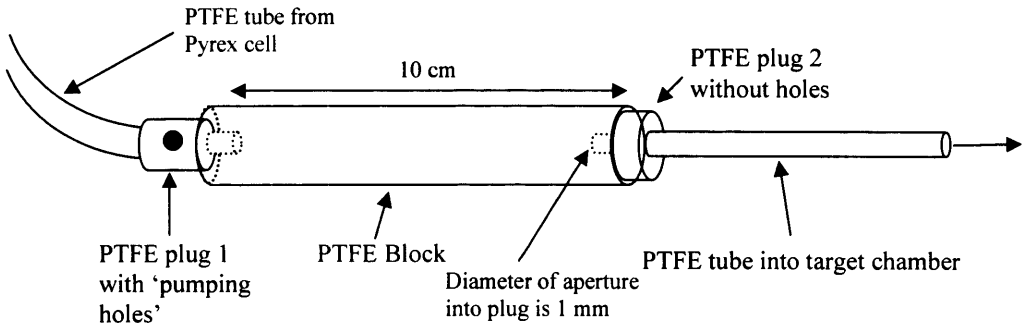

Figure 2.8. Schematic diagram to show how the gases are piped through the PTFE tubing and block. The pumping holes in the PTFE plug allow some gas to escape into the source chamber so that the target chamber pressure remains low, but the Pyrex cell pressures can be maintained at the maximum value for efficient H and D-atom production.

2.4.1. Design of PTFE tube mount

A crucial part of the experiment is to ensure that the flux of D-atoms and H-atoms is sufficient such that any recombination of the atoms to form HD can be observed, and also to ensure that these atoms are directed at the target surface. This requires a suitable mount in which to place the PTFE tubes that transport the atoms from the source region, so that the atoms impinge directly onto the HOPG surface. Originally, there was a single PTFE tube transporting the single H-atom beam up to the target surface. This tube was directed around the time-of-flight set-up and into a copper holder which resulted in the end of the tube being directed at the target surface, as shown in Figure 2.9. This way of mounting the tube worked reasonably well and the results for H_2, described in Chapter 5, were taken using this set-up.

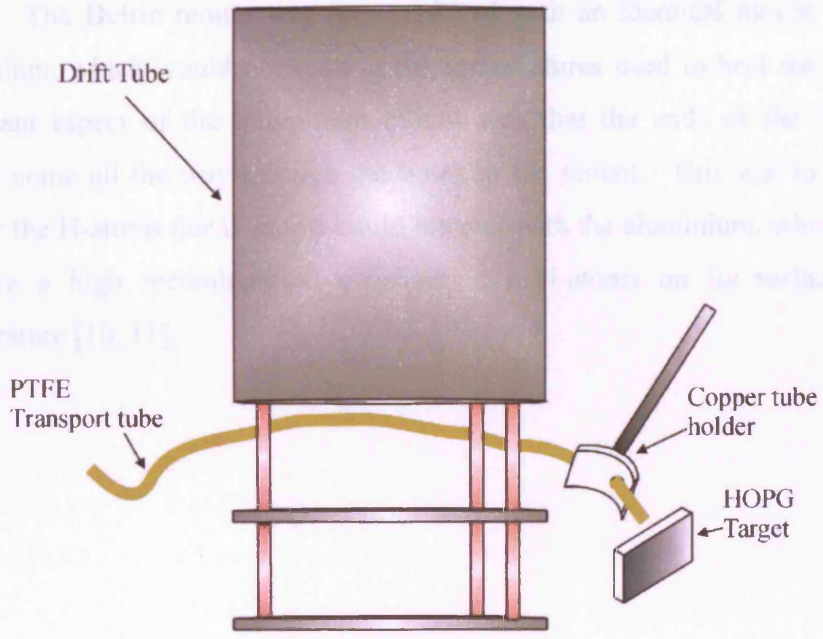

Figure 2.9. Schematic diagram showing the original copper holder for the H-atom beam PTFE transport tube.

When the second, D-atom, source was introduced, it became clear that a new mount design for the PTFE tubes was required. The physical dimensions of the target

vacuum chamber made it very difficult to install a similar copper holder for the PTFE tube carrying the D-atom beam, and it was not possible to put both tubes into the original copper holder that held the tube for the H-atom beam. The solution was to design a mount that could be used for both tubes, and attach it to the repeller plate of the time-of-flight mass spectrometer. This meant that both tubes could be directed towards the target surface at the same angle and at the same distance from the surface. This new mount has two holes, one for each PTFE tube transporting each atom beam, and directs the two atom beams straight onto the HOPG target. There is a gap of approximately 2 mm between the end of the tubes and the HOPG target. The set-up is shown in Figure 2.10 below. The new mount was originally made from Delrin, a plastic suitable for use under ultrahigh vacuum. However, when the target was heated with this plastic mount in place, prior to experiments, the proximity of the target to the transport tube mount resulted in the Delrin starting to soften. The Delrin mount was then replaced with an identical mount made from aluminium, which would not melt at the temperatures used to heat the target. An important aspect of the aluminium mount was that the ends of the PTFE tubes should come all the way through the holes in the mount. This was to ensure that neither the H-atoms nor D-atoms could interact with the aluminium, which is known to have a high recombination efficiency for H-atoms on its surface at room temperature [10, 11].

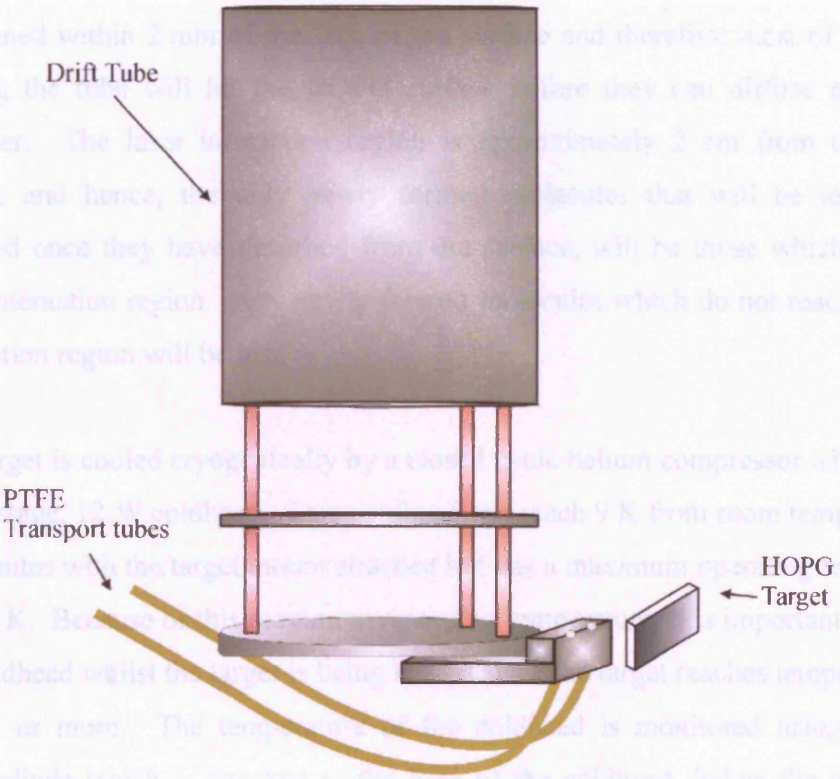

Figure 2.10. Schematic diagram to show how the PTFE transport tubes are set-up to direct the H-atom and D-atom beams onto the HOPG target.

2.5. Target Mount and Coldhead

It is necessary to mount the targets used in the cosmic dust experiment in such a way that they can be cooled to temperatures in the region of 10-20 K, to simulate the temperatures of the ISM [12], but also heated to around 500 K to clean them *in situ*. Using our experimental arrangement, it is possible to heat the target to temperatures exceeding 500 K however, it has been shown that any impurities on the surface are removed once the target has reached 500 K and so heating to this temperature is therefore sufficient [13, 14]. The targets also need to be oriented in the chamber close enough to the laser interaction region and mass spectrometer so that the molecules which have formed on them are detectable as soon as they leave the surface and cannot interact with the walls of the chamber first. As described in

section 2.4, the ends of the PTFE tubes that transport the atoms to the surface are positioned within 2 mm of the face of the surface and therefore most of the atoms leaving the tube will hit the HOPG surface before they can diffuse around the chamber. The laser interaction region is approximately 2 cm from the HOPG surface and hence, the only newly formed molecules that will be ionised and detected once they have desorbed from the surface, will be those which enter the laser interaction region. Any newly formed molecules which do not reach the laser interaction region will be lost.

The target is cooled cryogenically by a closed cycle helium compressor which drives a two-stage, 12 W coldhead. This coldhead can reach 9 K from room temperature in 45 minutes with the target mount attached but has a maximum operating temperature of 330 K. Because of this maximum operating temperature, it is important to protect the coldhead whilst the target is being heated since the target reaches temperatures of 500 K or more. The temperature of the coldhead is monitored using a silicon thermodiode which is attached to the base of the coldhead, below the copper rod described later in this section.

2.5.1. Target Mount Development

The target mount has undergone a series of developments to reach its current form, which allows the target to reach a minimum temperature of 10 K. The original target mount design only allowed the target to be cooled to $\geq$ 30 K, a temperature which although extremely cold, was not quite within the range of astrophysically relevant temperatures of ~10-20 K. The original target mount design is shown schematically in Figure 2.11 below. The target is attached to a removable mount on the end of a copper rod which is fixed to the coldhead. Given that the coldhead itself consistently reaches temperatures of 8-10 K, it seemed that the reason the target surface was only reaching temperatures of $\geq$ 30 K must be because of poor thermal conductivity through the various metal foils and copper parts attached to the coldhead, on which the target is mounted.

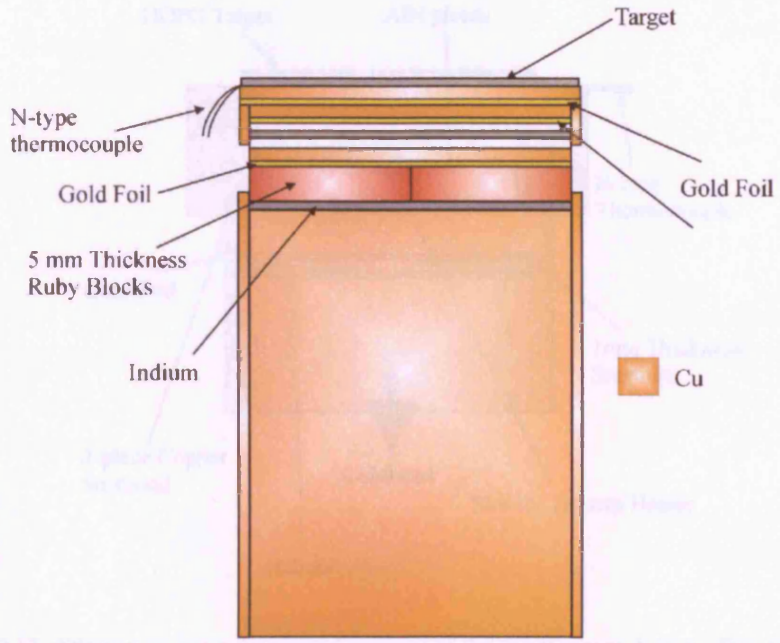

Figure 2.11. Schematic diagram showing the design of the original target mount arrangement. This setup resulted in target temperatures of ≥ 30 K. Tungsten tensioning wires that hold the arrangement tightly in place are not shown.

The first developmental redesign was to replace the 5 mm thickness ruby blocks with a piece of sapphire 1 mm thick. The ruby or sapphire interface between the target mount and the copper rod leading to the coldhead is essential as the thermal properties of the sapphire protect the coldhead when the target is heated, as discussed later on in this section. This replacement by itself did not improve the target temperature significantly and so the next step was to redesign the copper attachments above the sapphire.

The first redesign of the copper sections, shown in Figure 2.12 below, moved from three separate pieces of copper above the sapphire to just two pieces, which fitted around the AlN pieces with the tantalum strip heater in between. The AlN pieces replaced the original alumina pieces shown in Figure 2.11. This new design achieved a minimum target temperature of 23 K, an improvement on the original set-up but still not as low as required.

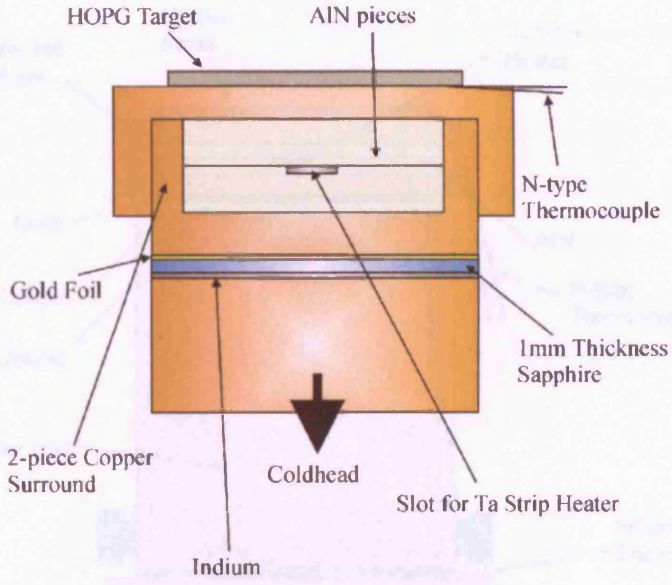

Figure 2.12. Diagram to show the second revision of the target mount design. This design achieved target temperature of 23 K.

Again, it seemed clear that the thermal contact between the layers above the coldhead still needed improvement. Hence, it was decided to make a copper surround for the AlN pieces that was just one piece of copper, rather than two-pieces slotted together. This meant that there was less opportunity for heat loss between the coldhead and the target since there would be no 'bad joints' between the copper sections if it was just a single piece. This new and final design is shown below in Figure 2.13. The minimum target temperature achieved with this new design is 10-15 K, well within the range required to be astrophysically relevant [12].

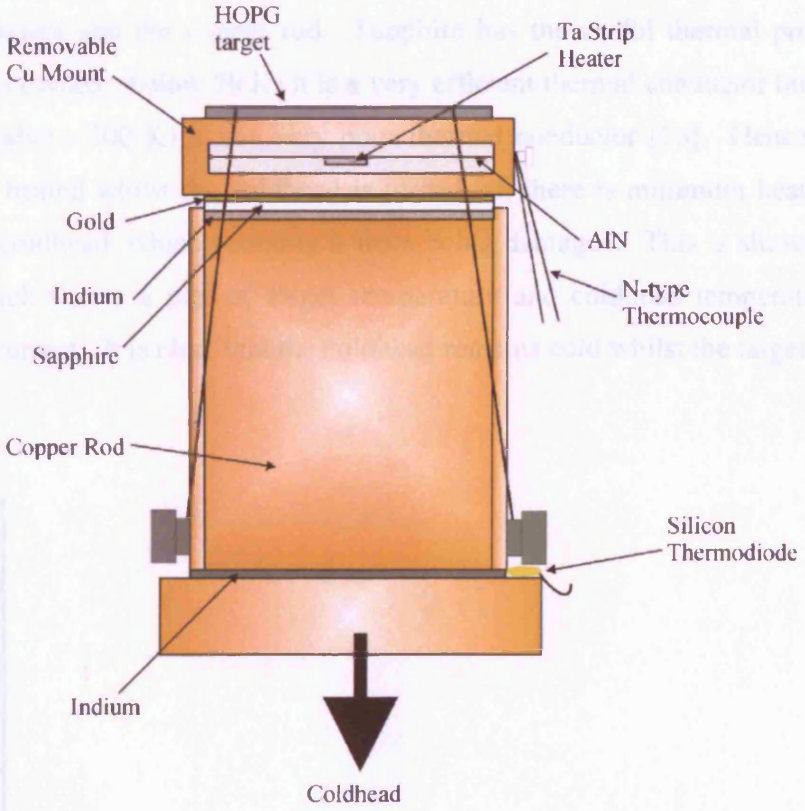

Figure 2.13. Schematic diagram of the current target mount set-up.

With this new design, the target is attached to the removable copper mount on the end of the copper rod which is fixed to the coldhead. As described above, the removable copper mount surrounds two pieces of AlN, between which a tantalum strip heater is held. This allows resistive heating of the target to remove any unwanted adsorbed species prior to the experiments. Before being placed in the chamber, the target is cleaned by the 'scotch tape' method in order to cleave a fresh graphite surface [15]. Once the chamber has been evacuated, the target can then be heated in situ with the Ta strip heater before each experiment.

As discussed above, the heater allows the target to be heated to temperatures greater than 500 K but this high temperature would damage the coldhead which cannot be heated in excess of 330 K. Again, as previously mentioned, this problem is solved

by using a piece of sapphire, 1 mm thickness, sandwiched between the removable copper mount and the copper rod. Sapphire has the useful thermal property that, when it is cooled, (below 50 K) it is a very efficient thermal conductor but when it is heated, (above 200 K) it is a very poor thermal conductor [16]. Hence, when the target is heated whilst the coldhead is turned on, there is minimum heat flow back into the coldhead, which prevents it from being damaged. This is shown in Figure 2.14 which shows a plot of target temperature and coldhead temperature against heating current. It is clear that the coldhead remains cold whilst the target is heated.

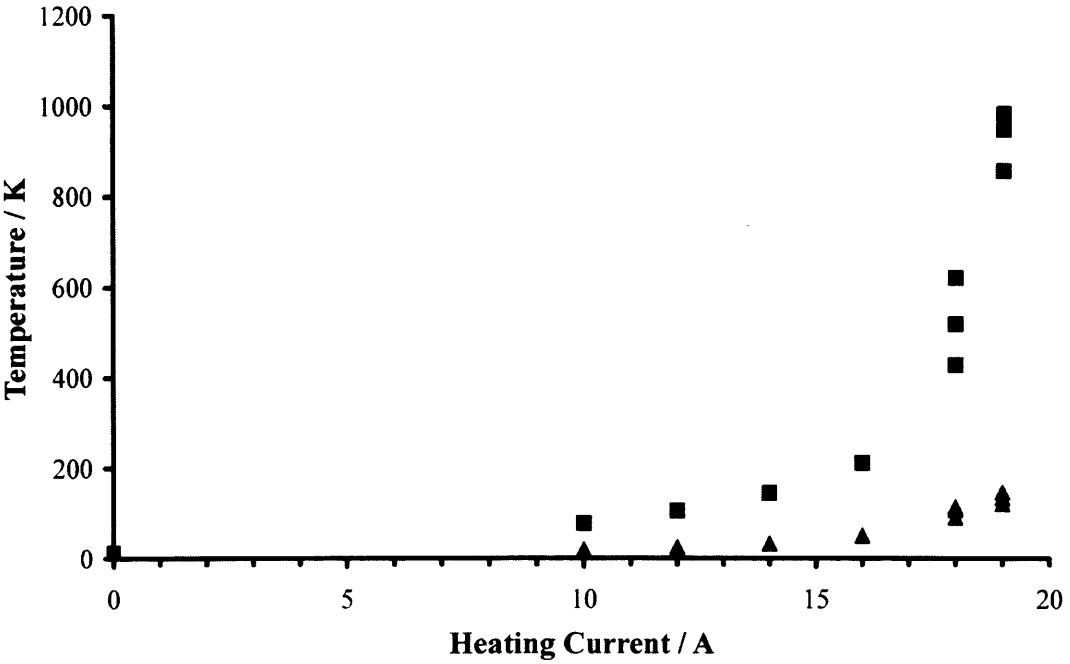

Figure 2.14. Graph showing the temperatures of the coldhead (▲) and the target (■) against heating current [2].

A strip of indium metal is placed between the sapphire and the copper rod and a length of gold foil is placed between the sapphire and the removable copper mount. Both these metals are used to improve the thermal contact between the various sections of the mount and the coldhead, to ensure the target temperature is as close as possible to that of the coldhead itself. Indium is very malleable and hence can be moulded to the copper rod and the sapphire; however indium has a relatively low

melting temperature (157 °C) and so cannot be used on the side of the sapphire in contact with the removable copper mount, as it would melt when the target was heated.

The target is secured to the top of the mount using Ni tensioning wires which are held taut with a set of 'sprung' washers and nuts (see Figure 2.15). Because they are 'sprung', the washers keep the wires tight should anything loosen on the mount, for example when it is heated.

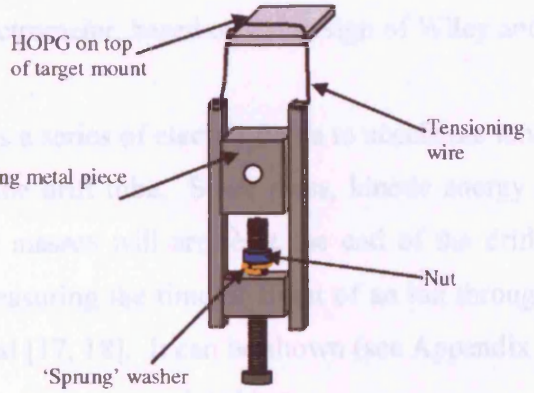

Figure 2.15. Diagram showing metal clamp for the tensioning wires. The 'sprung' washer is show in orange for clarity. One clamp is used on either side of the HOPG target.

An n-type thermocouple (Nickel-Chromium-Silicon) is attached to the side of the copper mount by means of a stainless steel screw, to monitor the temperature of the target. There is also a second n-type thermocouple which can be attached to various places on the mount in order to monitor the temperature of different regions. This second thermocouple can be used to help with diagnosing any problems with the heat transfer through the set-up, should the target fail to cool sufficiently. An aluminium radiation shield is attached to the end stage of the coldhead and surrounds the target mount set-up. This prevents any radiative heating of the target from the chamber and helps keep the target temperature at around 10 K.

2.6. Time of Flight Mass Spectrometry

As mentioned above, any new molecules which form on the HOPG surface can enter the laser interaction region and be ionised. Once the newly formed molecules have been ionised, the ions are detected using time-of-flight mass spectrometry (TOFMS). This technique is highly effective, in particular for detecting ions from pulsed sources such as those provided by a pulsed laser, as is the case in this experiment. Time-of-flight mass spectrometers also have advantages over other types of mass spectrometers in that they do not require accurate magnetic fields, they are compact in size and have no complex moving parts. The TOFMS used in this experiment is a conventional spectrometer, based on the design of Wiley and McLaren [17].

The TOFMS uses a series of electric fields to accelerate ions into an area of uniform potential called the drift tube. Since mass, kinetic energy and velocity are related, ions of different masses will arrive at the end of the drift tube at different times. Therefore, by measuring the time of flight of an ion through the drift tube, its mass can be determined [17, 18]. It can be shown (see Appendix A) that the time of flight of an ion t and its mass m are related by:

$$t = k\sqrt{m} + C \qquad 2.1$$

where k is a constant related to the magnitude of the electric fields and physical dimensions of the spectrometer and C is a constant from the electronic timing system. A schematic diagram of the TOFMS used in the cosmic dust experiment is shown in Figure 2.16.

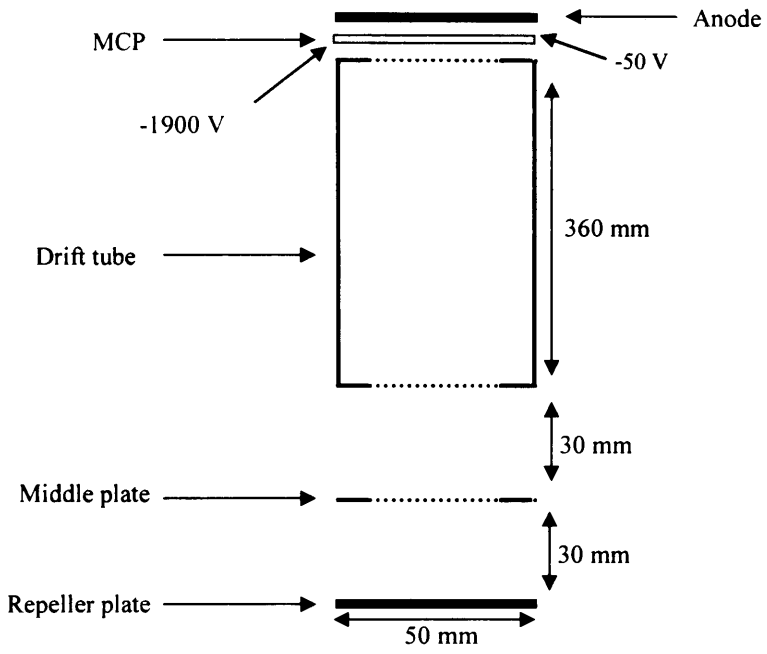

Figure 2.16. Schematic diagram of physical arrangement of the TOFMS.

The spectrometer consists of a repeller plate of 50 mm diameter, a middle plate, also of 50 mm diameter mounted 30 mm above the repeller plate, and a drift tube. The middle plate has a grid of fine Ni mesh secured across it to ensure the electric field applied remains uniform. The grid allows 98% transmission of the ions. The drift tube is mounted 30 mm above the middle plate, is 360 mm long and also has grids at either end to ensure a uniform electric potential throughout its length.

Mounted above the exit of the drift tube is the Micro Channel Plate (MCP) which is a surface made up of many 10 μm wide glass channels. The channels are coated in a compound with a very low work function. When ions hit the MCP, they collide with the walls of the channels and release electrons. These electrons release further electrons through collisions with the channel walls, until a cascade of electrons leaves the surface of the MCP. In general, $\sim 1 \times 10^4$ electrons are released per ion. A small negative potential, -50 V, repels the electrons away from the MCP until they hit an anode mounted 5 mm above the MCP and are detected.

To record a mass spectrum with the TOFMS, a series of amplification and counting electronics are utilised. With the laser as a pulse generator, it is not necessary to pulse the repeller plate, a common technique in other TOFMS experiments [18, 19]. The laser sends a 'start' signal to a multi-stop time-to-digital converter (TDC) which initiates a 'look window' in which to look for ion events. After a certain time, typically 9 μs, the pulse generator sends a 'reset' signal to the TDC which stops it recording ions for that laser pulse. During the look window, the TDC receives ion signals from the TOFMS. Before it reaches the TDC, the ion signal passes through a fast pre-amplifier (Ortec VT120). The signal then goes *via* an impedance matching circuit to an amplifier (Ortec 573) and a constant fraction discriminator (CFD) (Ortec 935) to give pulses suitable for the TDC. The counts from the TDC are then sent via a CAMAC/GPIB interface to a PC where they are displayed. Figure 2.17 below shows a diagram of the timing electronics.

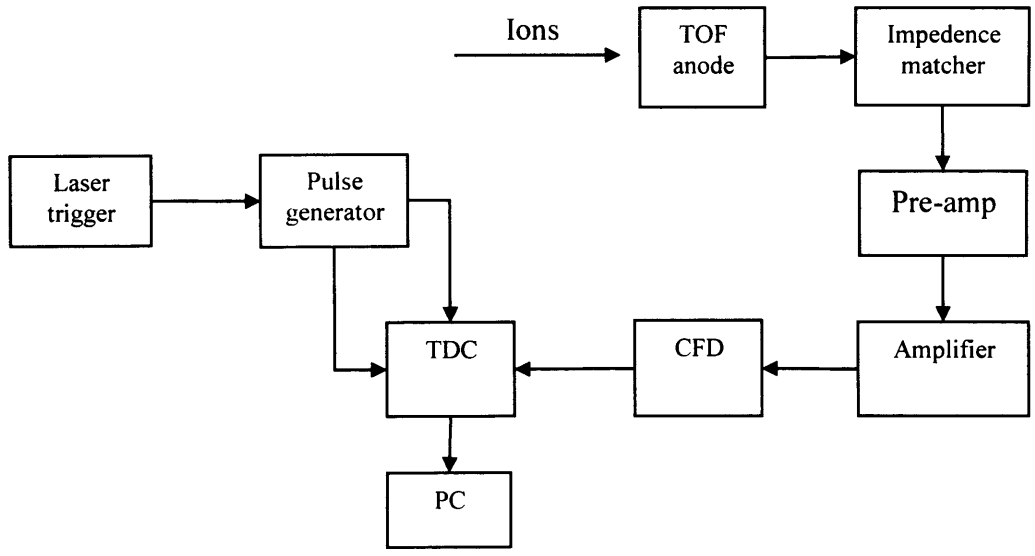

Figure 2.17. Block diagram to show the timing electronics for the TOFMS.

2.6.1. Focussing Conditions for the TOFMS

Two focusing conditions affect the resolution of a TOFMS. These are space-focusing and energy-focusing. Space-focusing addresses the problem that not all of the ions entering the drift tube are likely to have been ionised at a constant distance, s_0 away from it. An ion that is accelerated after being ionised a distance less than or equal to s_0 away from the drift tube will eventually be overtaken by an ion that was accelerated at a distance greater than s_0 away from the drift tube. This result is because ions which were formed a distance greater than s_0 away from the drift tube will have been accelerated for longer and hence, have higher corresponding kinetic energies. This difference in kinetic energies results in ions of the same mass having a spread of energies and therefore also a spread of flight times, which makes it hard to separate ions of similar mass.

To find the position at which ions with initial positions $s = s_0 \pm \frac{1}{2}\delta s$ pass each other, it is necessary to set $\left(\frac{dt}{ds}\right)_{s_0} = 0$, where t is time. The electric fields outside the drift tube can then be adjusted to focus ions of the same mass so that they arrive at the MCP with a small spread of flight times [17].

Space focussing is not such an issue in this experiment since the molecules are ionised in a very localised volume by the focussed laser.

Energy-focusing is a way of overcoming the problem of ions of the same mass having different initial kinetic energies. If two ions of the same mass and kinetic energy are travelling in opposite directions when the electric field is applied, the ion moving away from the drift tube will be decelerated until it stops. This ion will then be accelerated in the direction of the drift tube, until it travels at the same speed as the ion that was initially travelling in the direction of the drift tube when the field was applied. This results in a characteristic time lag between the two ions which can be minimised by energy focusing. Energy focusing requires adjusting the physical

dimensions of the spectrometer itself, namely the drift tube length and the magnitude of the ionisation and acceleration regions and can be at the expense of space-focusing [17]. Energy focusing is not important in this experiment since any spread in energies of the ions can be used to give information on the translational energies of the newly formed molecules.

For the experiments described here, the repeller plate is grounded to prevent any stray photoelectrons from the chamber walls hitting the plate and creating ions that would disrupt the mass spectrum. The middle plate is set to – 200 V, the drift tube is set to -800 V and the MCP is set to between -1700 and -1900 V depending on the signal strength. The procedure for taking a spectrum will be described in Chapter 5.

2.7. Summary

This chapter has described the current experimental arrangement used to study the ro-vibrational distribution of H_2 and HD that have formed on a cosmic dust analogue target under similar conditions to those found in interstellar space. The improvements to the original design of the apparatus have been described in detail. The following chapters will describe the laser and REMPI systems used in the experiments and also the commissioning of the new D-atom source referred to in this chapter.

2.8. References

1. Marinero, E.E., Rettner, C.T., and Zare, R.N., *Phys. Rev. Lett.*, 1982. 48(19): p. 1323-1326.

2. Perry, J.S.A., Gingell, J.M., Newson, K.A., To, J., Watanabe, N., and Price, S.D., *Meas. Sci. Technol.*, 2002. 13: p. 1414-1424.

3. Perry, J.S.A. and Price, S.D., *Astrophys. Space Sci.*, 2003. 285(3-4): p. 769-776.

4. Meijer, A.J.H.M., Farebrother, A.J., and Clary, D.C., *J. Phys. Chem. A*, 2002. 106(39): p. 8996-9008.

5. Dyson, J.E. and Williams, D.A., *The Physics of the Interstellar Medium*. 2 ed. 1997: Institute of Physics publishing. 165.

6. Higgins, D.P., McCullough, R.W., Geddes, J., Woolsey, J.M., Schlapp, M., and Gilbody, H.B., 1995. 99-1: p. 177-183.

7. McCullough, R.W., *Characterisation and Applications of a New Reactive Atom Beam Source*, in *Application of Accelerators in Research and Industry*, J.L. Duggan and I.L. Morgan, Editors. 1997, AIP Press: New York. p. 275-278.

8. Wise, H. and Wood, B.J., *Advances in Atomic and Molecular Physics*, 1967. 3: p. 291-353.

9. Donnelly, A., Hughes, M.P., Geddes, J., and Gilbody, H.B., *Meas. Sci. Technol.*, 1992. 3(5): p. 528-532.

10. Walraven, J.T.M. and Silvera, I.F., *Rev. Sci. Instrum.*, 1982. 53(8): p. 1167-1181.

11. Koch, N. and Steffens, E., *Rev. Sci. Instrum.*, 1999. 70(3): p. 1631-1639.

12. Greenberg, J.M., *Surf. Sci.*, 2002. 500(1-3): p. 793-822.

13. Bolina, A.S., Wolff, A.J., and Brown, W.A., *J. Chem. Phys*, 2005. 122(4): p. 044713.

14. Pirronello, V., Liu, C., Shen, L.Y., and Vidali, G., *Astrophys. J.*, 1997. 475(1): p. L69-L72.

15. Zecho, T., Guttler, A., and Kuppers, J., *Chem. Phys. Lett.*, 2003. 370(3-4): p. 366-370.

16. Berman, R., Foster, E.L., and Ziman, J.M., 1955. 231(1184): p. 130-144.

17. Wiley, W.C. and McLaren, I.H., *Rev Sci Instr*, 1955. 26(12): p. 1150-1157.

18. Cotter, R.J., *Time-of-flight mass spectrometry*. ACS symposium series. 1994: American Chemical Society.

19. Price, D. and Milnes, G.J., 1990. 99: p. 1-39.

Chapter 3. The Laser System and REMPI Technique

3.1. Laser System

The laser technique of Resonance Enhanced Multi-Photon Ionisation (REMPI) is used to probe the ro-vibrational state of the H_2 and HD molecules that have formed on the HOPG surface, as described in Chapter 2. The principles behind, and the reasons for using, this specific technique will be described in section 3.2. In this section, the laser system used to produce the photons which state-selectively ionise the product molecules will be described.

For the REMPI scheme used in these experiments, photons of wavelength 200 - 230 nm are required, in order to probe the $v = 0$, 1, and 2 levels of H_2, D_2 and HD. The laser system used to produce these photons consists of three parts: a neodymium: yttrium aluminium garnet (Nd:YAG) pump laser, a tuneable dye laser and a frequency tripling unit. Each of these parts will be described individually.

3.1.1. Nd:YAG Laser

The Nd:YAG laser is a solid state laser with a core rod of Yttrium Aluminium Garnet (YAG) $Y_3Al_5O_{12}$. Nd^{3+} ions are present in the YAG lattice as impurities. These ions are randomly distributed on the lattice in sites usually occupied by yttrium ions, and provide the energy levels required for the laser transitions. The YAG rod is not directly involved in the lasing action but plays an important role in how the laser works.

The electrostatic field, known as the 'crystal field', of the YAG rod influences the Nd^{3+} ion impurities in the lattice. In the gas phase, free Nd^{3+} ions have many degenerate energy levels. However, when these ions are placed in the crystal field of the YAG rod, these energy levels are split, partly lifting their degeneracy. In the

Nd:YAG laser, the crystal field also changes the transition probabilities between various energy levels of the Nd^{3+} ion so that some transitions, which are forbidden in the free ion, become allowed in the ion in the lattice. The overall result is that the ground and first excited states of the Nd^{3+} ions are split into groups of levels, as shown in Figure 3.1. These levels are pumped by an intense pulse of light from two xenon flash-lamps. This flash excites the Nd^{3+} ions from the ground $^4I_{9/2}$ level to levels above the $^4F_{3/2}$ state, these higher levels result in a larger number of available pumping transitions which increase the efficiency of the laser. These upper levels then undergo rapid, non-radiative decay to the $^4F_{3/2}$ state, from which the laser transition occurs [1]. The most intense laser transition occurs at 1064 nm and is a superposition of the two transitions shown in Figure 3.1.

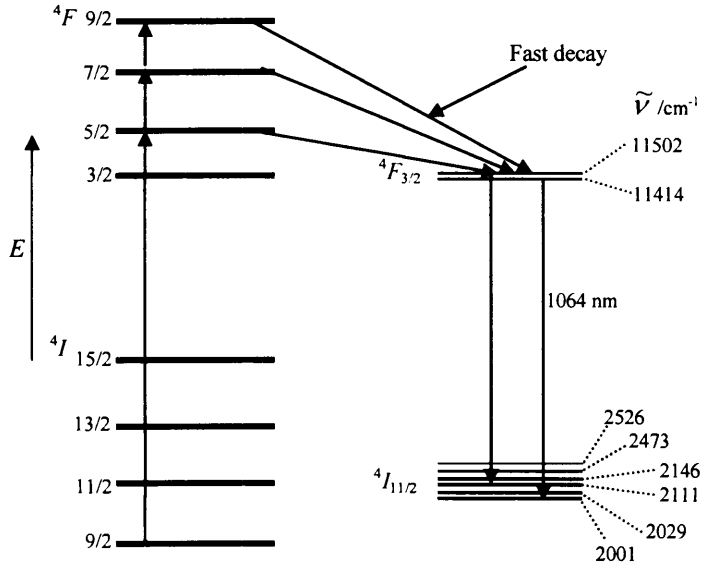

Figure 3.1. Energy level diagram for the transitions in the Nd:YAG laser. $\tilde{\nu}$ refers to the energy of the particular level.

The 1064 nm light is frequency doubled to 532 nm by a potassium di-hydrogen phosphate (KD*P, KD_2PO_4) crystal and the power of the pulse is increased by an electro-optic Q-switch, which is provided by a Pockels cell before the KD*P crystal. Q-switching is a technique for obtaining short, intense pulses of radiation from a laser. This technique involves introducing time-dependent losses into the laser

cavity, that is, lowering the Q-factor of the cavity. With a high loss in the cavity, the gain due to the population inversion can reach large values without laser action occurring, since the poor Q-factor prevents laser action while energy is being pumped into the excited state of the laser medium. When a large population inversion has been achieved, if the cavity loss is suddenly reduced (i.e., the Q-factor is suddenly improved) then laser oscillations can begin, resulting in a large, powerful pulse. For effective Q-switching, the rate of pumping must be faster than the spontaneous decay rate of the upper lasing level, to prevent it depopulating faster than it can be filled and therefore preventing a large population inversion from building up. Also, the Q-switch should switch rapidly compared with the build up of laser oscillations, otherwise the laser oscillations will only build up gradually, resulting in a longer pulse with lower peak power [1, 2]. The Nd:YAG laser pulses at 10 Hz with pulses of duration 4-6 ns. The 532 nm second harmonic has energies of approximately 400 mJ per pulse. This second harmonic is used to pump the dye laser, described in the next section.

3.1.2. Tuneable Dye Laser

The photoionisation of H_2 or HD from a variety of specific ro-vibrational states requires a variable-wavelength light source. This variable wavelength light source is a dye laser, which is pumped by the 532 nm second harmonic of the Nd:YAG laser described above. The advantage of using a dye laser is that it is tuneable over a significant wavelength range, and hence, can be scanned through a range of wavelengths in order to find a signal for the particular ro-vibrational state of interest [1, 2].

The active medium in a dye laser is an organic dye dissolved in a solvent, for example methanol. When the dye is excited it fluoresces, at a longer wavelength than the excitation source, over a broad wavelength range. The laser transitions occur between the singlet electronic states S_1 and S_0, as shown in Figure 3.2. Pumping with the Nd:YAG laser results in excitation from the ground S_0 state to the

first excited electronic state, S_1. Pumping to the S_2 electronic state is also possible, as shown in Figure 3.2. Rapid non-radiative decay by collisional relaxation to the lower ro-vibrational levels in S_1 then occurs, resulting in a population inversion between these levels and the S_0 ro-vibrational levels. The laser transition is then fluorescence, which occurs between these low levels in S_1 and ro-vibrational levels in S_0. Because there are many closely spaced ro-vibrational levels in both singlet states, there is the possibility of many transitions, resulting in an emission spectrum which is very broad [1, 2].

The triplet states shown in Figure 3.2 are not directly involved in the laser action but they can affect it, as there is a small probability of a non-radiative $S_1 \rightarrow T_1$ transition, despite it being formally disfavoured quantum mechanically [3]. This transition can result in a reduction in the gain of the laser as the $T_1 \rightarrow T_2$ transition, which is allowed, is pumped by the same range of frequencies of light required to pump the laser transition. This problem is overcome by operating the laser in short pulses, shorter than the time taken to build up any population in T_1, typically 1 μs. The time between the pulses must be long enough to allow the transition $T_1 \rightarrow S_0$ to occur in order to empty the T_1 levels before they can be pumped to T_2 and reduce the laser gain.

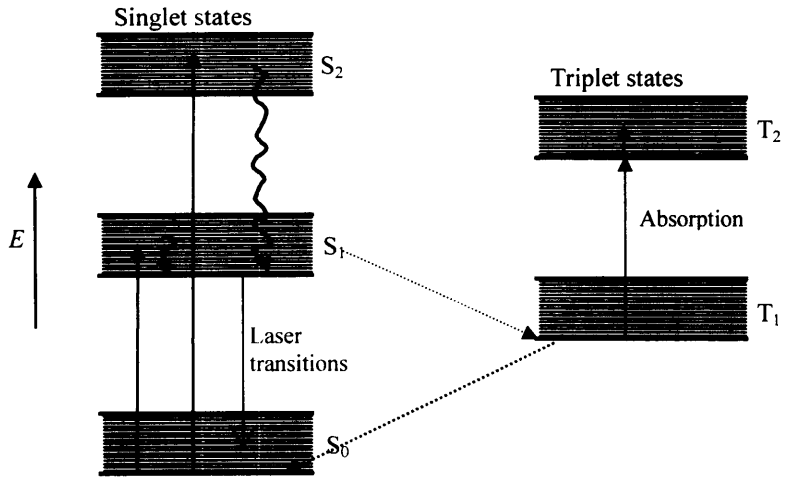

Figure 3.2. Schematic diagram of the energy levels used in a typical dye laser.

The laser dyes used in the cosmic dust experiment are chosen depending on the wavelength required to ionise a H_2 or HD molecule in a specific internal energy state. To ionise H_2 or HD in the $v'' = 0$ vibrational state, a 2:1 ratio of Rhodamine 640: Rhodamine 610 is used, which has a dye wavelength range of 594-629 nm. For H_2 or HD in $v'' = 1,2$ vibrational states, DCM (Rhodamine 101) is used with a wavelength range of 607-663 nm. The dyes are dissolved in methanol.

There are three stages to the dye laser: a tuneable oscillator, a pre-amplifier and an amplifier. The oscillator allows us to choose the wavelength of laser light required. 5% of the incoming 532 nm light is directed into the oscillator cavity using a dichroic mirror and then passes through a quartz cell containing a flow of laser dye. Light emitted from the dye cell is then directed onto a grating with 2400 lines mm^{-1} which acts as the rear mirror of the oscillator. The angle of the grating can be computer-adjusted so that the reflected light (first order) is at a specifically chosen wavelength. As discussed above, the wavelengths available from the oscillator depend on the particular dye used.

Following tuning in the oscillator cavity, the beam of light exiting the cavity is directed onto the pre-amplifier which consists of a dye cell pumped by 10% of the 532 nm beam. The pre-amplifier acts to increase the power of the dye beam but is not a laser cavity itself. This dye beam is then directed into the final amplifier stage. The final amplifier is also a dye cell, pumped by the remaining 85% of the 532 nm beam. With the DCM dye in use, typical output power of the dye laser is on the order of 60-70 mJ/pulse. When using the Rhodamine (640:610) mix dye, the output power of the dye laser is closer to 80 mJ/pulse. The linewidth of the dye laser beam is around 0.1 cm^{-1} and the beam diameter is around 3-6 mm. Figure 3.3 shows a schematic of the dye laser optical layout.

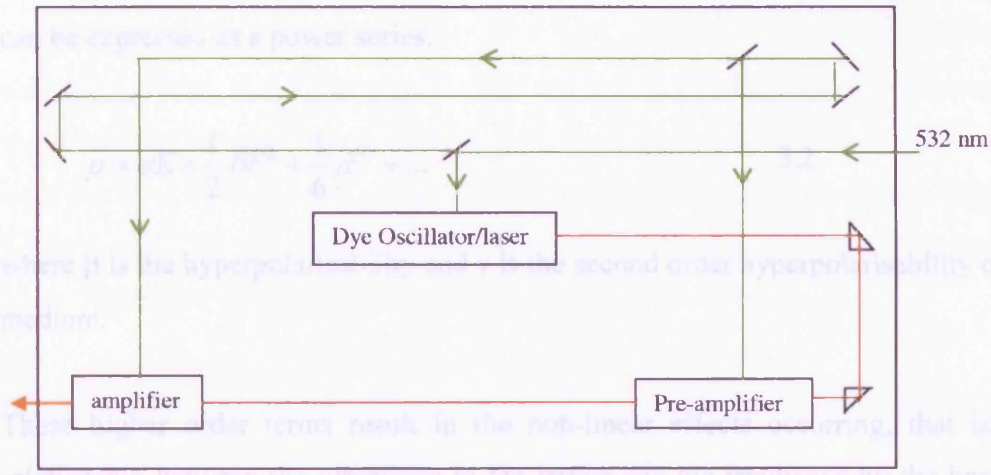

Figure 3.3. Schematic diagram of the optical layout of the dye laser.

3.1.3. Frequency Doubling and Frequency Mixing

The REMPI schemes used for H_2 and HD require the photons from the dye laser, of wavelengths around 600 - 660 nm, to be frequency tripled to give photons of around 200 - 220 nm [4]. To do this, non-linear crystals of KD^*P and Barium Borate (BBO) β-BaB_2O_4 are used to create the second and third harmonics of the dye laser beam. The dye beam is first frequency doubled using the KD^*P crystal and this doubled light is then frequency mixed with the residual dye beam in the BBO crystal to result in a beam of light with a third of the wavelength of the original dye beam.

3.1.3.1. Frequency Doubling

When a beam of light propagates through a solid, electric dipoles are induced in the solid which interact with the oscillating electric field. The induced electric dipole moment, μ, is given by:

$$\mu = \alpha E \qquad 3.1$$

where E is the oscillating electric field and α is the polarisability of the medium.

This equation is only approximate and if the incident electric field is large enough, it can be expressed as a power series:

$$\mu = \alpha E + \frac{1}{2}\beta E^2 + \frac{1}{6}\gamma E^3 + \ldots \qquad 3.2$$

where β is the hyperpolarisability and γ is the second order hyperpolarisability of the medium.

These higher order terms result in the non-linear effects occurring, that is, the relationship between the vibrations in the lattice and the irradiance by the beam of laser light becomes non-linear as the amount of light hitting the crystal increases. The magnitude of the incident electric field, E, is given by:

$$E = E_0 \sin(2\pi\nu t) \qquad 3.3$$

where E_0 is the amplitude of oscillation, ν is the frequency.

Since

$$E^2 = E_0^2(\sin(2\pi\nu t))^2 \qquad 3.4$$

$$= \frac{1}{2}E_0^2(1-\cos(2\pi 2\nu t)) \qquad 3.5$$

this gives us radiation scattered with twice the original frequency of the incident wave, known as second harmonic generation. This can only take place in non-centrosymmetric crystals which have a non-linear response to an applied electric field [1, 2].

In order to maintain the maximum power from the second harmonic light, it is important to use a phase-matching technique. Due to the optical properties of the crystals used to produce second harmonic light, the refractive index of the crystal

(and hence the speed of the light travelling through it) depends on the wavelength [1, 2]. This results in the frequency doubled light travelling through the crystal at a different speed to that of the fundamental beam. The fundamental is continuously generating the frequency-doubled beam on its passage through the crystal and hence, the frequency-doubled beam cannot stay in phase with itself. If the phase difference is big enough, the frequency-doubled beam may get completely out of phase and cause destructive interference, reducing its power considerably.

Phase-matching overcomes this by choosing a path through the crystal so that the velocity of the fundamental beam, which corresponds to the O-ray (ordinary ray) of frequency ν and refractive index n_o^{ν}, is the same as that of the frequency doubled beam, which corresponds to the E-ray (extraordinary ray) of frequency 2ν and refractive index $n_e^{2\nu}(\theta)$, this is shown in Figure 3.4. Hence a path is chosen whereby $n_o^{\nu} = n_e^{2\nu}(\theta)$, both beams remain in phase and there is a build-up in the irradiance of the second harmonic.

To achieve the build up in irradiance of the second harmonic described above can be difficult and a number of factors can influence the success of the phase matching, for example the refractive indices are temperature dependent so it may be necessary to control the temperature of the crystals used. The laser beam divergence must also be minimised since only one direction of propagation through the crystal is perfectly phase-matched. The optics used for second harmonic generation and phase-matching of the beams in this experiment will be described in section 3.1.4.

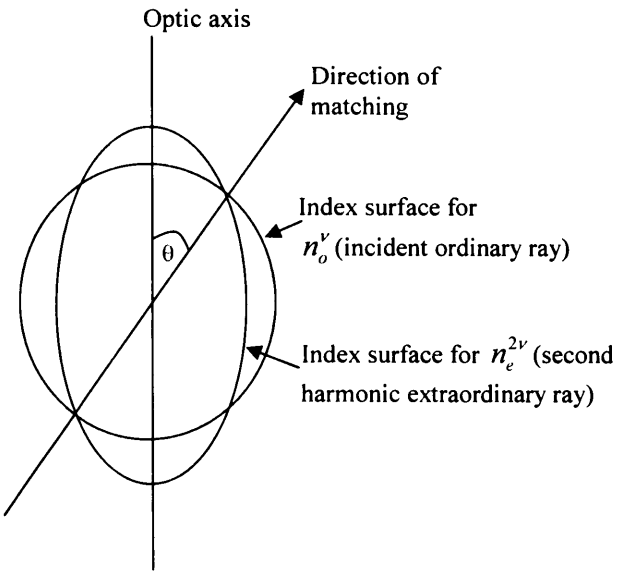

Figure 3.4. Wave ellipsoid for incident and second harmonic rays. The ellipse and circle show how the phases of the electric fields of the O-ray and E-ray change as they go through the crystal.

3.1.3.2. Frequency Mixing

Following the generation of the second harmonic light, the dye beam and the second-harmonic beam are frequency mixed in a BBO crystal to give light of the wavelength required for (2+1) REMPI of H_2 or HD. The frequency of the light produced in the BBO crystal will be the sum or difference of the frequencies of the two beams entering the crystal.

The frequency mixing works as follows [1, 2]. For the two beams of frequencies ν_1 and ν_2 and amplitudes E_1 and E_2, the second order polarisation term from equation 3.2 becomes

$$\beta(E_1 \sin \nu_1 t + E_2 \sin \nu_2 t)^2 \qquad 3.6$$

Expanding this term gives

$$\beta\left(E_1^2 \sin^2 \nu_1 t + E_2^2 \sin^2 \nu_2 t + 2E_1 E_2 \sin \nu_1 t \sin \nu_2 t\right) \qquad 3.7$$

The third term in this equation can be rewritten as

$$E_1 E_2 \beta[\cos(\nu_1 - \nu_2)t - \cos(\nu_1 + \nu_2)t] \qquad 3.8$$

which gives us terms that show that light is emitted from the mixing crystal with frequencies

$$\nu_3 = \nu_1 \pm \nu_2 \qquad 3.9$$

Hence, we obtain photons of light at three times the frequency (or a third of the wavelength) of the incident dye laser beam.

3.1.4. Frequency Doubling and Frequency Mixing Optics

As described in the above theory, the light from the dye laser is frequency-doubled and then this doubled light is mixed back with the original dye laser beam in order to generate the photons of wavelength required for the REMPI process in H_2, D_2 and HD, around 200-220 nm depending on the ro-vibrational state of interest. This is achieved in the final stage of the laser system, which consists of a frequency doubling and tripling unit, shown schematically in Figure 3.5 below.

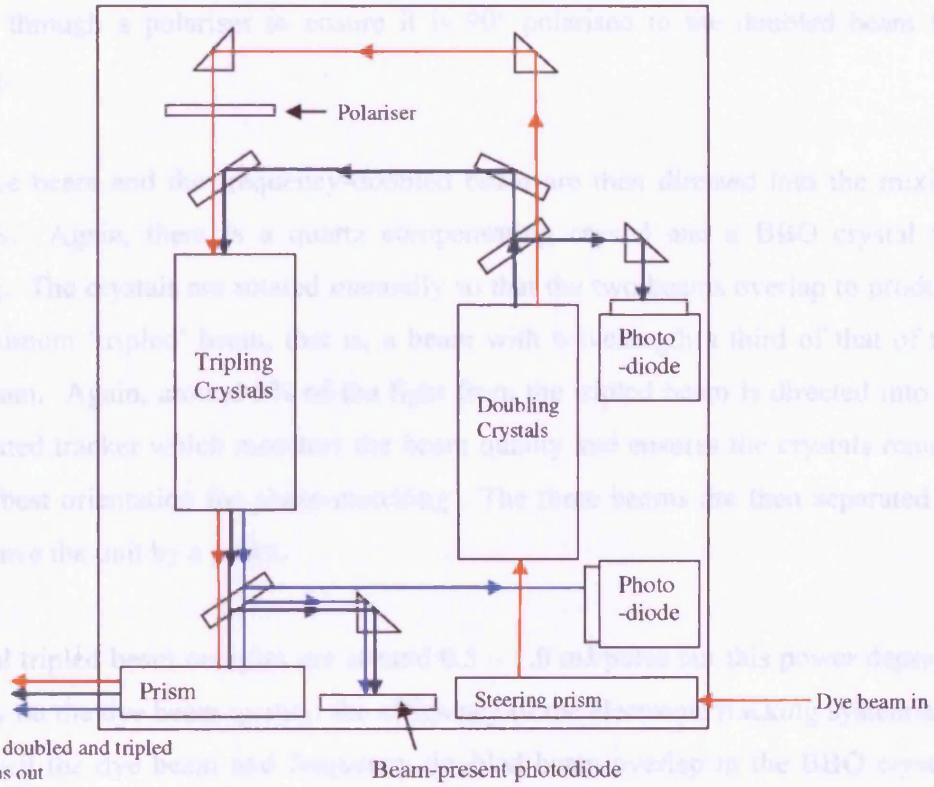

Figure 3.5. Schematic diagram showing the set-up of the doubling and tripling optics of the laser system.

The dye beam is horizontally polarised as it enters the unit and is steered into the doubling crystals. As mentioned earlier, these are a KD*P crystal, which doubles the frequency of the dye beam, and a quartz compensating crystal. The KD*P crystal is rotated for phase-matching and the quartz crystal acts to compensate for any 'beam walk' during this rotation. The crystals can be rotated manually to find the optimum beam and then an automated tracker ensures they remain in the correct orientation for the beam to stay optimised. The frequency doubling is not 100% efficient so both the doubled beam and the dye beam leave the KD*P crystal, vertically polarised, and then pass through a beam splitter that separates them. Around 5% of the doubled light is then directed into a photodiode. It is this photodiode that sends a signal to the automated tracker which then monitors the quality of the frequency-doubled beam and ensures the crystals are rotated into the

correct position for maximum phase-matching during a laser scan. The dye beam passes through a polariser to ensure it is 90° polarised to the doubled beam for mixing.

The dye beam and the frequency-doubled beam are then directed into the mixing crystals. Again, there is a quartz compensating crystal and a BBO crystal for mixing. The crystals are rotated manually so that the two beams overlap to produce the optimum 'tripled' beam, that is, a beam with wavelength a third of that of the dye beam. Again, around 5% of the light from the tripled beam is directed into an automated tracker which monitors the beam quality and ensures the crystals remain in the best orientation for phase-matching. The three beams are then separated as they leave the unit by a prism.

Typical tripled beam energies are around 0.5 – 1.0 mJ/pulse but this power depends heavily on the dye beam quality, the efficiency of the electronic tracking system and how well the dye beam and frequency doubled beam overlap in the BBO crystal. Achieving useable tripled beam energies is the most challenging part of the laser system and requires much time and effort in order to ensure the tracker has enough light to ensure an adequate tripled beam. The final output power must be greater than 0.3 mJ/pulse in order for the light detected by the trackers to be adequate to ensure efficient phase matching. The 'tripled' beam is then directed into the ionisation region of the time-of-flight mass spectrometer and focused down to a spot to give enough light intensity for REMPI.

The beam is directed into the vacuum chamber using two UV light-reflecting steering mirrors, which allow vertical and horizontal adjustment of the beam. The beam passes through a lens of focal length 30 cm before it enters the vacuum chamber, which focuses it down into an intense spot of radius 0.15 mm, area 7.1×10^{-4} cm^2. The resulting power density per pulse is then:

$$\frac{1\times10^{-3}}{7.1\times10^{-4}}\cdot\frac{1}{4\times10^{-9}} = 0.35\ \text{GJ cm}^{-2} \qquad 3.10$$

for an average pulse length of 4 ns at the lens focus. Given that the laser pulses at 10 Hz, this power density must be multiplied by 10 Hz to give a time-averaged power density. This then becomes 3.5 GW cm^{-2}, in good agreement with other groups who have carried out REMPI of H_2 [4, 5].

In order to minimise stray photoelectrons from the chamber walls, a series of light baffles are employed. Stray photons from the laser could release photoelectrons from the steel chamber walls, which could in turn ionise any other gas molecules in the vacuum chamber, swamping the H_2 and HD REMPI signals. A set of conical baffles sits just inside the quartz entry window to the vacuum chamber in order to minimise the stray light entering the chamber. Attached to the end of the baffles is a copper tube, diameter 10 mm which has a roughened inner surface. The roughened surface ensures that any stray light which gets through the baffles is reflected around inside the copper tube and does not get into the interaction region of the time-of-flight mass spectrometer. A second set of light baffles sits before the exit window and has a PTFE tube at the front. The beam then exits the vacuum chamber through a second quartz window and is dumped. This set-up is shown schematically in Figure 3.6 below.

The photoelectron background is minimised by setting the laser output at a wavelength where it will not excite a H_2 rotational line and then letting H_2 into the reaction chamber. The TOF is then set to integrate H_2^+ ions and the ion counts in a set period of time (20 seconds) are monitored. The laser beam alignment through the chamber is then adjusted until it is passing through the chamber with the minimum of background counts.

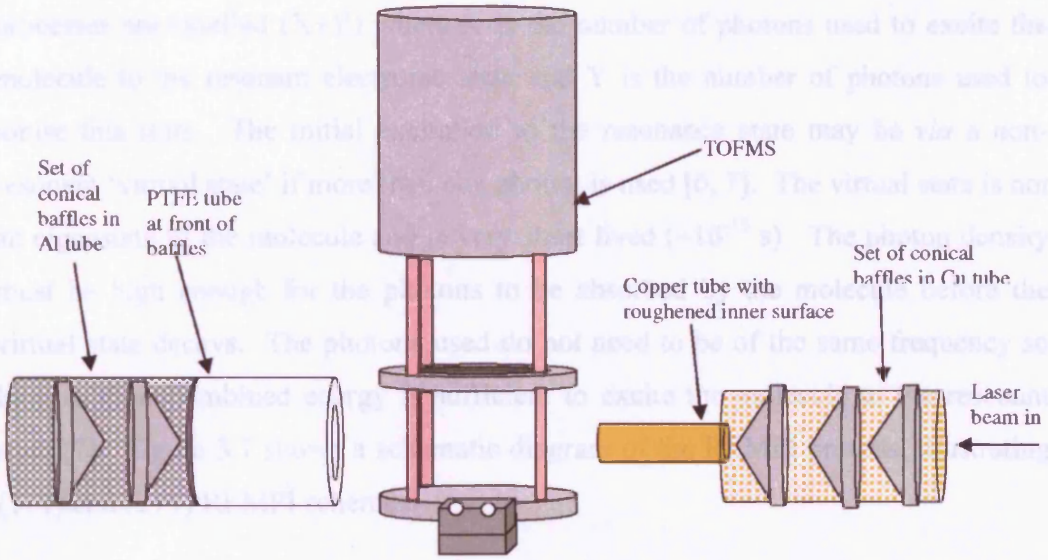

Figure 3.6. Schematic diagram to show the light baffles used in the vacuum chamber to minimise photoelectrons. (Not to scale).

3.2. Resonance Enhanced Multi-Photon Ionisation (REMPI)

Resonance Enhanced Multiphoton Ionisation (REMPI) is a well established laser spectroscopic technique which allows ionisation of molecules in specific ro-vibrational states [4, 6]. REMPI has advantages over techniques such as Laser Induced Fluorescence (LIF) since it detects ions rather than photons. Ion detection is much more efficient than photon detection and so REMPI is a much more sensitive spectroscopic technique [6]. REMPI also has advantages over non-resonant multi-photon ionisation because the ionisation process is *via* a relatively long-lived resonance state. This means that there is a bigger cross section for a resonantly excited molecule absorbing another photon and being ionised than a non-resonantly excited molecule, which will increase the signal strength.

The REMPI process uses one or more photons to excite a molecule to a resonant electronic state. The molecule is then ionised with further photons and the ions are

detected, in this case by a time-of-flight mass spectrometer (TOFMS). REMPI processes are labelled (X+Y) where X is the number of photons used to excite the molecule to the resonant electronic state and Y is the number of photons used to ionise this state. The initial excitation to the resonance state may be *via* a non-resonant 'virtual state' if more than one photon is used [6, 7]. The virtual state is not an eigenstate of the molecule and is very short lived ($\sim 10^{-15}$ s). The photon density must be high enough for the photons to be absorbed by the molecule before the virtual state decays. The photons used do not need to be of the same frequency so long as their combined energy is sufficient to excite the molecule to the resonant state [7]. Figure 3.7 shows a schematic diagram of the REMPI process, illustrating (1+1) and (2+1) REMPI schemes.

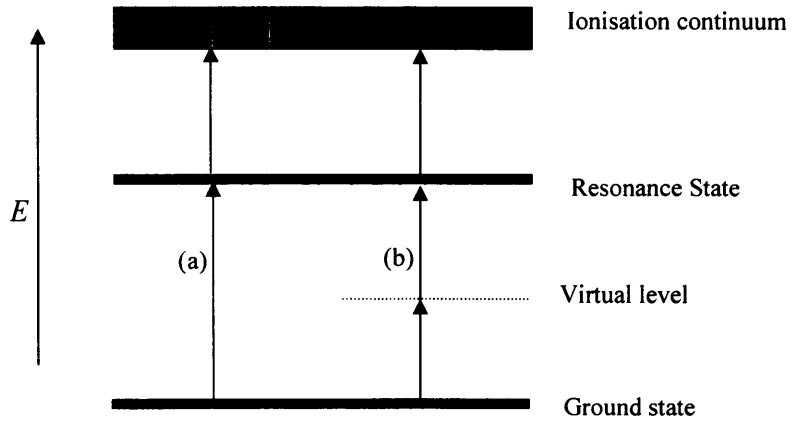

Figure 3.7. Schematic energy level diagram showing (a) (1+1) and (b) (2+1) REMPI schemes.

The state-selective ionisation of H_2 and HD carried out in the cosmic dust experiment uses a well understood excitation scheme, with a (2+1) REMPI process [4, 5, 8-10]. This scheme is shown in Figure 3.8. Two photons are used to excite the molecules from a specific rotational-vibrational level in the ground electronic state, $X\,^1\Sigma_g^+$ (v'', J''), *via* a virtual level to the ground vibrational level of the $E,F\,^1\Sigma_g^+$ resonant electronic state. A further photon of the same frequency as the initial two photons then ionises the molecule.

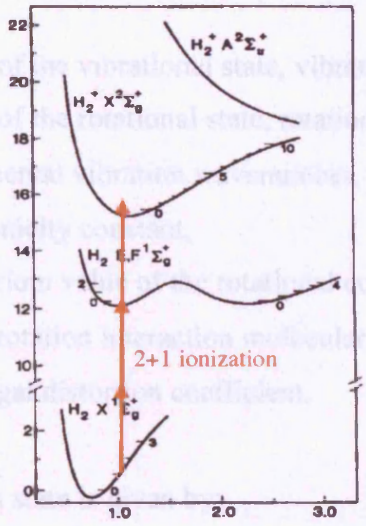

Figure 3.8. (2+1) REMPI scheme for H_2 taken from reference [4].

The state-selective step is a two photon process which means that the change in rotational quantum number J is $\Delta J = 0, \pm 2$ and hence only O, Q and S branches are detected. These branches arise from the rotational fine structure of ro-vibrational transitions. For the (2+1) schemes used here, only Q branch transitions are detected ($\Delta J = 0$): $X\,^1\Sigma_g^+ (v'', J'') \rightarrow E,F\,^1\Sigma_g^+ (v' = 0, J' = J'')$ since these are much stronger than the O or S branch transitions, due to them being vibronically favoured [8, 10, 11].

The wavelengths of photons required for these transitions can be calculated using the standard spectroscopic equations for electronic, rotational and vibrational energies.

$$E_v = \left(v+\tfrac{1}{2}\right)\varpi_e - \left(v+\tfrac{1}{2}\right)^2 \varpi_e x_e \ \text{cm}^{-1} \qquad 3.11$$

and

$$E_J = \left[B_e - \alpha\left(v+\tfrac{1}{2}\right)\right]J(J+1) - DJ^2(J+1)^2 \ \text{cm}^{-1} \qquad 3.12$$

In the above equation, the following definitions apply:

E_v is the energy of the vibrational state, vibrational quantum number v,
E_J is the energy of the rotational state, rotational quantum number J,
ϖ_e is the fundamental vibration wavenumber,
x_e is an anharmonicity constant,
B_e is the equilibrium value of the rotational constant B,
α is a vibration-rotation interaction molecular constant,
D is the centrifugal distortion coefficient.

The total energy of each state is given by:

$$E_{\text{total}} = E_{elec} + E_v + E_J \qquad 3.13$$

where E_{elec} is the electronic state energy.

The wavelength of light required to excite H_2 from a ro-vibrational level in the ground electronic state to the excited resonance state can therefore be calculated with these equations, using the known constants [12]. An example set of calculated photon energies for rotational levels in H_2 $v = 1$ using the constants in reference [12] is given in Table 3.1 below.

Table 3.1. Photon wavelengths required for the transition $X\ ^1\Sigma_g^+ (v'' = 1, J'') \rightarrow E,F\ ^1\Sigma_g^+ (v' = 1, J' = J'')$.

J''	v''	λ / nm
0	1	210.4924
1	1	210.6008
2	1	210.8165
3	1	211.1377
4	1	211.5613
5	1	212.0834
6	1	212.6989
7	1	213.4013
8	1	214.1831
9	1	215.0350
10	1	215.9465

The laser system used for the experiments is tuneable over a range of wavelengths, as discussed previously in section 3.1. The output wavelengths of the laser are adjusted by a stepper motor which moves the grating. This motor does not always repeat its movement to 100 % accuracy since the Q-branch transitions appear to shift in wavelength over time, and are not at the wavelengths predicted from the spectroscopic constants. The separations between the Q-branch transitions are constant however and so the REMPI spectra can be calibrated to determine which peak corresponds to which transition.

3.3. Summary

This chapter has described the laser system and REMPI technique used in these experiments to study the formation of molecular hydrogen on cosmic dust analogues surfaces. The following chapters will describe the results obtained from these experiments.

3.4. References

1. Wilson, J. and Hawkes, J., *Optoelectronics an introduction.* 3 ed. 1998: Prentice Hall Europe.

2. Hawkes, J.W.J., *Lasers principles and applications.* 1 ed. Prentice hall international series in optoelectronics. 1987: Prentice Hall Europe.

3. Banwell, C.N. and McCash, E.M., *Fundamentals of Molecular Spectroscopy.* 4th ed. 1994: McGraw-Hill book company.

4. Rinnen, K.D., Buntine, M.A., Kliner, D.A.V., Zare, R.N., and Huo, W.M., *J. Chem. Phys.*, 1991. 95(1): p. 214-225.

5. Kligler, D.J. and Rhodes, C.K., 1978. 40(5): p. 309-313.

6. Lin, S.H., Fujimura, Y., Neusser, H.J., and Schlag, E.W., *Multiphoton spectroscopy of molecules.* 1 ed. Quantum electronics - principles and applications, ed. P.K. Paul Liao. 1984: Academic press inc.

7. Hollas, J.M., *Modern Spectroscopy.* 4 ed. 2004: John Wiley & Sons Ltd.

8. Kligler, D.J., Bokor, J., and Rhodes, C.K., 1980. 21(2): p. 607-617.

9. Marinero, E.E., Rettner, C.T., and Zare, R.N., *Phys. Rev. Lett.*, 1982. 48(19): p. 1323-1326.

10. Marinero, E.E., Vasudev, R., and Zare, R.N., *J. Chem. Phys.*, 1983. 78(2): p. 692-699.

11. Pozgainer, G., Rendulic, K.D., and Winkler, A., *Surf. Sci.*, 1994. 309: p. 344-349.

12. Huber, K.P. and Herzberg, G., *Molecular spectra and molecular structure IV: Diatomic molecules.* 1979: van Nostrand Reinhold Company.

Chapter 4. Commissioning of the new D-atom Source

As discussed in Chapter 2, it was necessary to design and commission a new D-atom source following the introduction of a new microwave generator for the atomic hydrogen source. This Chapter will describe the various attempts to quench out the excited H_2 in vibrational level $v'' = 1$ that became evident in the H-atom source, following the introduction of the new microwave unit. It will then go on to describe the implementation and commissioning of the D-atom source in order to probe the formation of HD, thus removing the problem of vibrationally excited H_2 from the H-atom source entering the target chamber.

4.1. Commissioning the new D-atom Source

4.1.1. Evidence of Problems with the Single Atom Source

Using the original experimental set-up and microwave generator described in reference [1], there was conclusive evidence that none of the excited H_2 in vibrational levels $v'' \geq 1$ that may have formed in the atom source itself was reaching the interaction region in the target chamber. Furthermore, no vibrationally excited H_2 was detected in the target chamber when the PTFE transport tube was directed away from the line of sight of the laser, which meant that the excited H_2 that had been detected in $v'' = 1$ and $v'' = 2$ must have formed on the cold HOPG surface and not anywhere else in the chamber. Some of these results for H_2 formation will be described in Chapter 5.

Before the installation of the new microwave generator, the diagnostic used to check that no vibrationally excited H_2, formed in the atom source, was reaching the target chamber was an aluminium block attached to the end of a coldhead. This coldhead used the same closed cycle helium compressor as the coldhead which cools the

HOPG target, as described in Chapter 2, and maintained the temperature of the Al block at around 110-120 K.

Aluminium has the useful property that, when it is cooled to around 120 K, it has a low recombination efficiency for H-atoms on its surface. However when Al is warmer, around 300 K, it has a high recombination efficiency for H-atoms [2, 3]. When the Al block was cold, definite signals for H_2 formed ro-vibrationally excited from the HOPG surface were observed, but when the block was allowed to warm up to room temperature, these signals disappeared [1]. This observed effect on the signals indicated that when the Al block was cold, H-atoms from the source were not recombining on its surface but rather being translationally cooled through collisions with its walls and then recombining on the HOPG surface to form ro-vibrationally excited H_2. However, when the Al block was warm, the lack of signal indicated that the H-atoms were recombining on the surface of the aluminium to form H_2, and that these H_2 molecules were thermalising before they reached the target chamber. This observation indicated that no vibrationally excited H_2 was reaching the laser interaction region from anywhere other than the target surface (see Figure 4.1). The absence of any excited H_2 signal when the Al block was cold also indicated that any excited H_2 that may have formed in the source cell had thermalised with the Al block, through collisions with its walls, before reaching the laser interaction region in the target chamber. This suggests that before the installation of the new microwave generator, there could not have been a large amount of vibrationally excited H_2 formed in the H-atom source region.

Following the replacement of the original microwave unit with a new Sairem 300 W microwave generator, the above observations were not repeatable. Molecular hydrogen formed in the $v''= 1$ ro-vibrationally excited state was observed whether or not the aluminium block was at 120 K, as shown in Figure 4.2.

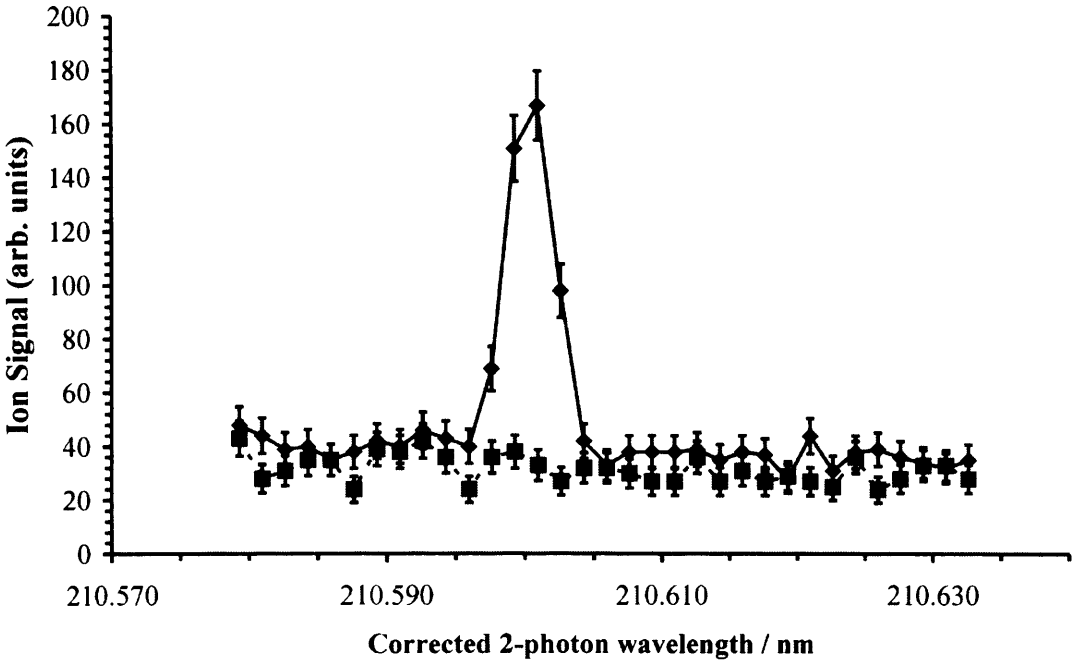

Figure 4.1. Plot to show the REMPI signal for H_2 E,F $^1\Sigma_g^+$ ($v' = 0$, $J' = J''$)-$X^1\Sigma_g^+$ ($v'' = 1$, $J'' = 1$) detected from a room temperature HOPG target. The solid line indicates the signal with the Al block at 113 K and the dashed curve shows the result of the same experiment with the Al block at room temperature [1].

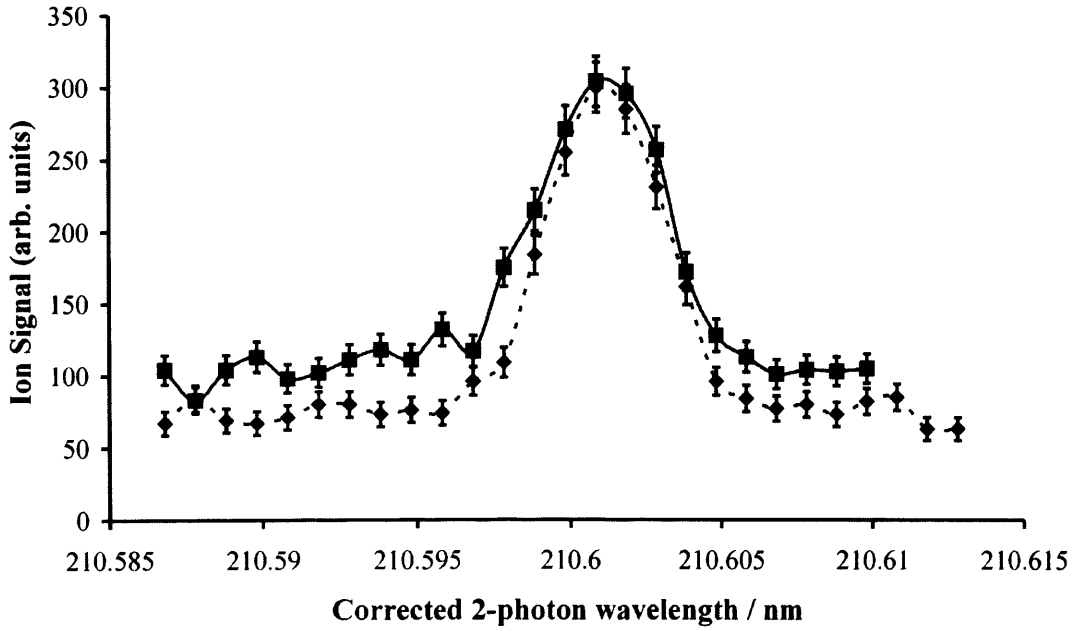

Figure 4.2. Plot to show the REMPI signal for H_2 E,F $^1\Sigma_g^+$ ($v' = 0$, $J' = J''$)-$X^1\Sigma_g^+$ ($v'' = 1$, $J'' = 1$) detected with the HOPG surface and the new microwave generator in place,. The solid line indicates the Al block at room temperature and the dashed line is for the Al block at 120 K. Signals are detected at both Al block temperatures, indicating excited H_2 is entering the target chamber from the H-atom source line.

Following the observation of a clear $v'' = 1, J'' = 1$ REMPI signal for H_2 whether the Al block was at room temperature or at 120 K, the HOPG target was removed and the PTFE tube from the H-atom source cell was directed straight into the laser interaction region between the time-of-flight repeller plate and middle plate. The tube was redirected in this manner so that the laser would only ionise any hydrogen coming into the target chamber directly from the atom source. A REMPI signal was observed for H_2 formed in $v'' = 1, J'' = 1$ coming directly from the H-atom source when the Al block was warm (see Figure 4.3) and this signal disappeared when the microwave generator was turned off. These observations proved that the new microwave generator had changed the conditions in the Pyrex cell, and that vibrationally excited H_2 was entering the target chamber from the H-atom source.

It has so far been made clear that the aim of this experiment is to measure the ro-vibrational distribution of H_2 formed on a cold HOPG surface under conditions similar to those of the ISM. Hence, it is also clear that this excited hydrogen entering the target chamber from the H-atom source would seriously affect the results of the experiment, as it would be indistinguishable from any H_2 that had formed ro-vibrationally excited on the target surface.

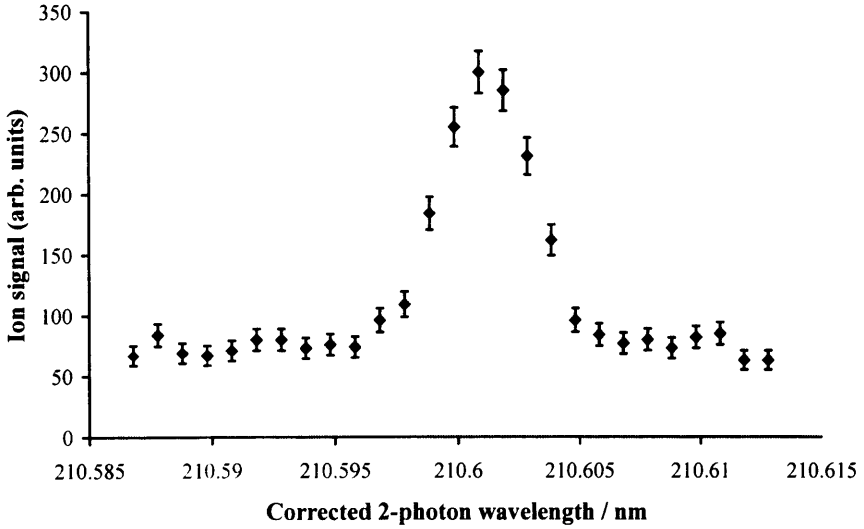

Figure 4.3. REMPI signal detected for H_2 $E,F\ ^1\Sigma_g^+$ ($v' = 0, J' = J''$)-$X^1\Sigma_g^+$ ($v'' = 1, J'' = 1$) with the Al block at room temperature and no HOPG target in the chamber. The PTFE transport tube for the H-atom beam was pointed directly into the laser beam path, between the repeller plate and middle plate of the TOFMS.

4.1.2. Attempts to remove excited H_2 from the atom source

Following the discovery that the excited H_2 in the atom source was entering the target chamber before it had thermalised with the Al block, various attempts were made to adjust the pressure conditions in the transport tubes and Pyrex cell regions in order to quench the excited molecules back to the ground vibrational level before they reached the target region.

The first adjustment was to decrease the inner diameter of the capillary at the base of the Pyrex cell from 1 mm to 0.5 mm, since increasing the pressure in this capillary would induce more collisions and quench out the excited molecules. This was successful in that no vibrationally excited H_2 was observed from the source with this set-up in place. However, a big drawback was that this smaller capillary also reduced the flux of H-atoms significantly, meaning it was impossible to get an acceptable flux of H-atoms to the surface of the target in order to form H_2, as shown below in Figure 4.4 and 4.5.

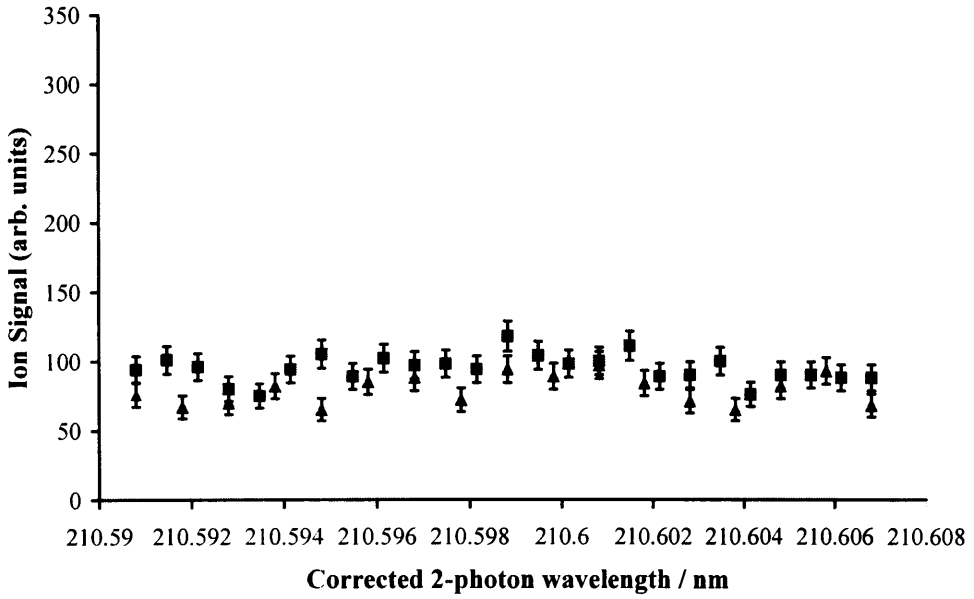

Figure 4.4. Plot to show REMPI signal for H_2 $E,F\,^1\Sigma_g^+$ ($v' = 0, J' = J''$)-$X\,^1\Sigma_g^+$ ($v'' = 1, J'' = 1$) from the HOPG surface with a 0.5 mm capillary on discharge cell. No clear REMPI signal is observed. ■ indicates Al block 120 K, ▲ indicates Al block room temperature. No signal at both temperatures indicates that there is no H-atom flux to the target surface.

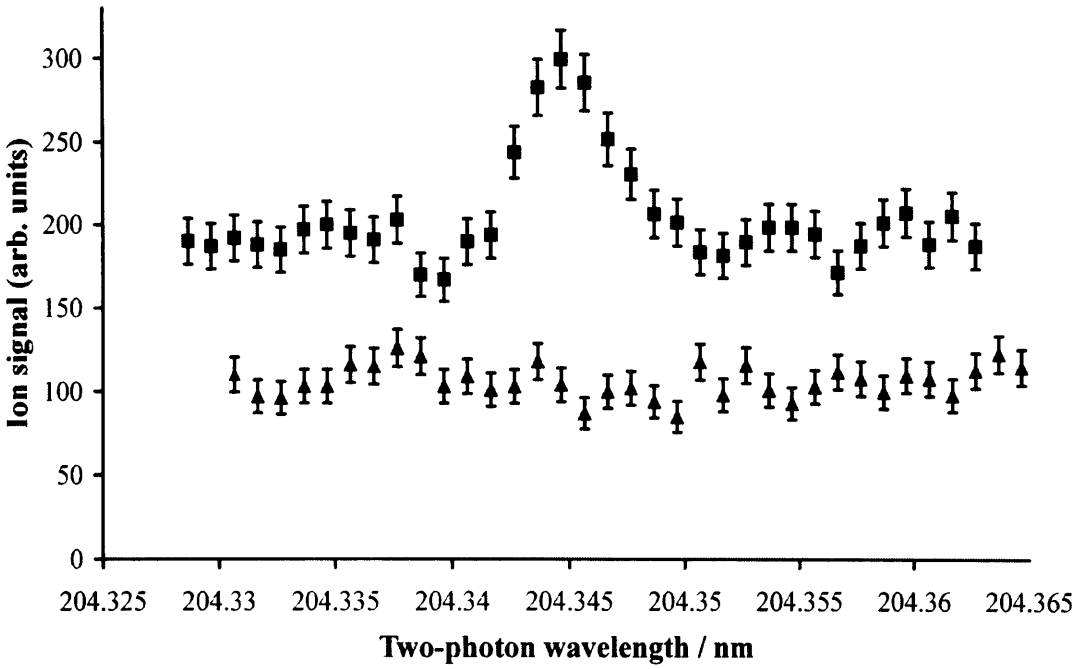

Figure 4.5. Plot of the H-atom REMPI signal when a 0.5 mm capillary was used on the discharge cell (▲). The H-atom REMPI signal when a 1 mm capillary was used on the discharge cell is shown for comparison (■). It is clear that no H-atom REMPI signal is observed with a 0.5 mm capillary. The lines are offset for clarity.

Changing the inner diameter of the capillary on the end of the cell clearly had a detrimental effect on the production of H-atoms, as shown in Figure 4.5, so it was decided to try to quench out the excited H_2 molecules by adjusting the pressure conditions in the transport tube.

The obvious way to change the pressure conditions in the transport tube was to use different sized apertures on the PTFE plugs that were used as junctions between the PTFE transport tube and the aluminium cooling block. The plugs currently in use are described in Chapter 2. The plugs also act to differentially pump the source and target chambers by allowing a proportion of the gas out of the transport tube into the source chamber, hence keeping the pressure in the target chamber as low as possible. The set-up used is shown in Figure 4.6 below. For each adjustment to the set-up, the chamber had to be vented whilst the plugs were changed and then pumped down

again. The H-atom source then had to be allowed to 'condition' for 35 - 48 hours to ensure that the signals observed were maximised (see Chapter 2).

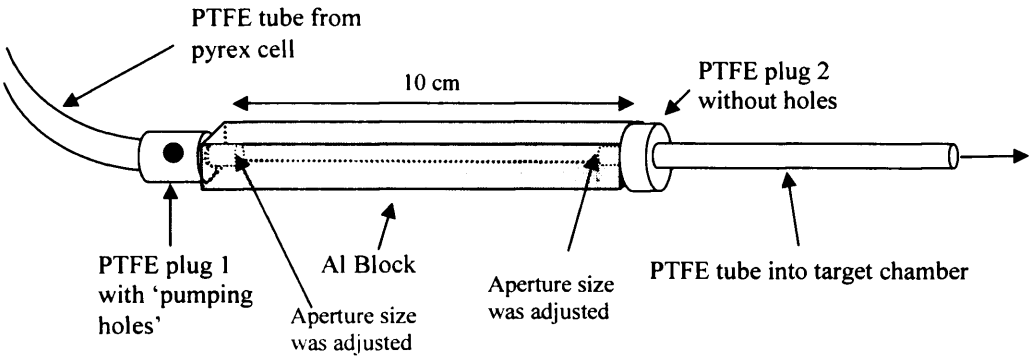

Figure 4.6. Diagram to show the set-up of the PTFE plugs into and out of the Al block. Adjusting the inlet gas aperture size on either of the blocks helped someway to quenching out the excited H_2 signal. However, only by removing the pumping holes completely did the signal disappear.

Removing the pumping holes completely, by putting in a PTFE plug without any pumping holes, made it possible to quench out the excited H_2 signal to below the detection threshold (see Figure 4.7). Unfortunately, this resulted in a pressure in the target chamber of approximately 8×10^{-6} Torr, much too high to be astrophysically relevant. The background counts in these graphs is much higher than in the previous plots due to the higher pressure, coupled with the fact that H_2 is a background gas in the chamber.

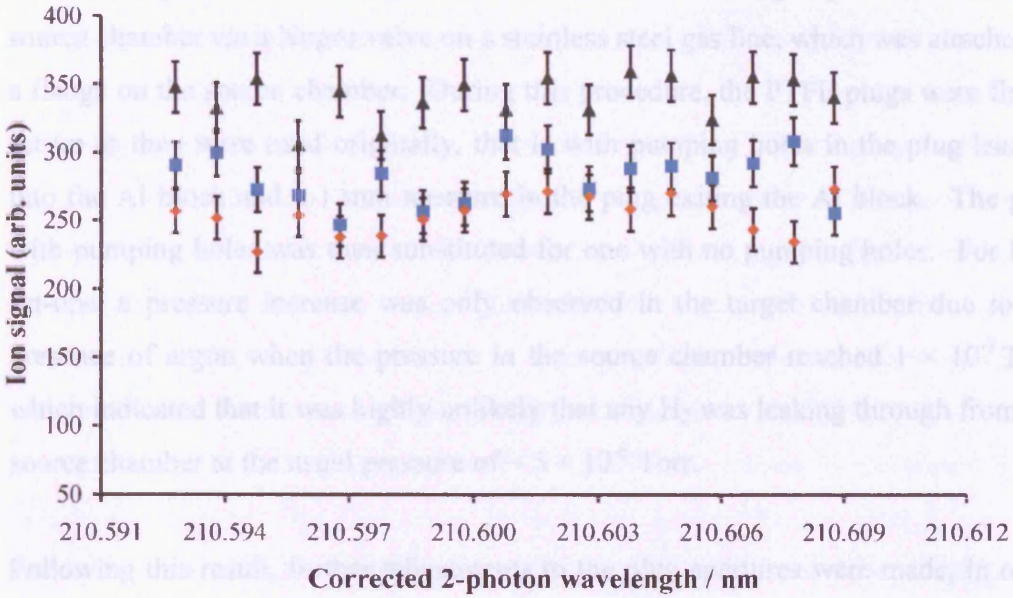

Figure 4.7. Graph to show H_2 $v''=1$, $J''=1$ REMPI signal. Data were taken with no target in the chamber and the PTFE tubing piped up to TOFMS. ▲indicates the spectrum taken at a cell pressure of 1.0 Torr, resulting in a target chamber pressure of 6.2×10^{-6} Torr, ■ indicates cell pressure of 0.9 Torr, resulting in a target chamber pressure of 6.0×10^{-6} Torr, ♦indicates cell pressure of 0.8 Torr, resulting in a target chamber pressure of 5.5×10^{-6} Torr. It is clear that the signal is quenched out at higher target chamber pressures.

The next procedure was to change the position of the pumping holes so that they were in the plug exiting the Al block rather than the plug leading into the Al block, to see if a higher pressure of gas into the Al block resulted in the vibrationally excited H_2 signal being quenched out. For this set-up, the plug leading into the Al block had an aperture of 2 mm. The aperture of the plug exiting the Al block was initially 3 mm and was then changed to 1 mm. Neither set-up had any effect on the H_2 $v''=1$, $J''=1$ signal observed from the H-atom source.

Before proceeding with any other adjustments to the apertures of the plugs at the Al block interface, it was decided to make sure that there was no way that the signal observed in the target chamber could have arisen due to H_2 gas from the source chamber diffusing around the brass seal between the two chambers (see Chapter 2). This was done by allowing some argon gas into the source chamber and observing

whether the pressure in the target chamber increased. The argon gas was let into the source chamber *via* a Nupro valve on a stainless steel gas line, which was attached to a flange on the source chamber. During this procedure, the PTFE plugs were firstly set-up as they were used originally, that is with pumping holes in the plug leading into the Al block and a 1 mm aperture in the plug exiting the Al block. The plug with pumping holes was then substituted for one with no pumping holes. For both set-ups, a pressure increase was only observed in the target chamber due to the presence of argon when the pressure in the source chamber reached 1×10^{-3} Torr, which indicated that it was highly unlikely that any H_2 was leaking through from the source chamber at the usual pressure of $\sim 5 \times 10^{-6}$ Torr.

Following this result, further adjustments to the plug apertures were made, in order to try to quench out the excited H_2 signal. Changing the aperture in the plug exiting the Al block to 0.3 mm (with 2 mm diameter pumping holes in this plug) resulted in a decrease in the H_2 $v'' = 1$, $J' = 1$ signal strength, but the flux of H-atoms became undetectable. The arrangement of the holes in the plug exiting the Al block were then changed so that there was a 1 mm aperture and 2 mm pumping holes, but the pumping holes were situated after the aperture where previously they had been situated before the aperture. This set-up again had no effect on the strength of the H_2 $v'' = 1, J' = 1$ signal. Further attempts with different sized apertures and different arrangements of the pumping holes also had no significant effect on the excited H_2 signal from the atom source.

Following the adjustments described above, it had become clear that it was not possible to remove the excited H_2 from the H-atom beam without either decreasing the flux of H-atoms below a detectable level or making the pressure in the target chamber too high to be astrophysically relevant. This result is perhaps not surprising, since it has been shown both experimentally and through theoretical calculations, that the rate of self-relaxation of vibrationally excited H_2 is small ($\sim 10^{-17}$ cm^3 s^{-1}) at temperatures from 50 – 500 K [4-6]. Because of these two facts,

it was decided to move on to studying the formation of HD on the HOPG surface. In order to do this, a second atom source was required to produce D-atoms.

Following the decision to introduce a second atom source, producing D-atoms, it was decided that the aluminium cooling block was unnecessary. The reason for this was that two atom beams would have required two cooling blocks, which would have meant redesigning the system for attaching the single Al block to the coldhead. The main use of the Al block was as a diagnostic to prove that the H_2 signals observed came from the HOPG surface and not from the source itself. The introduction of the second source, to investigate the formation of HD meant that it was highly unlikely that HD could form in the source chamber and it has been shown that this is the case (See Chapter 5). A second purpose of the Al block was to translationally cool the H-atoms as they travelled into the target chamber. However, the fact that the atom beam was piped up to the target in a second length of PTFE tubing, after it had been through the Al block, meant that the beam would have warmed up to room temperature by the time it reached the target surface. This increase in gas temperature is not very significant for these experiments since the difference in kinetic energy between a 100 K atom beam and a 300 K atom beam is quite small, on the order of 0.017 eV per molecule. Therefore, the Al block was no longer needed. The Al block was replaced with similar sized PTFE blocks which were not cooled but which give the same flow conditions as the previous Al block. The same plug set-up as was originally used with the Al block is used with both the PTFE blocks, as described in Chapter 2.

4.1.3. Deuterium Atom Source

The design of the deuterium atom source was identical to that of the H-atom source already in place. These sources are described in Chapter 2. It was found that it was possible to run both sources from the same microwave generator with no loss of flux, as described in Chapter 2.

It is possible to do REMPI of both H-atoms and D-atoms, as described in reference [7]. This is useful because it allows the beams of H-atoms and D-atoms to be characterised independently, and without the need for the aluminium block diagnostic described in section 4.1.1. The following REMPI scheme is used, where the atoms are ionised through the n = 3 state of the atom, at around 205 nm (Figure 4.8).

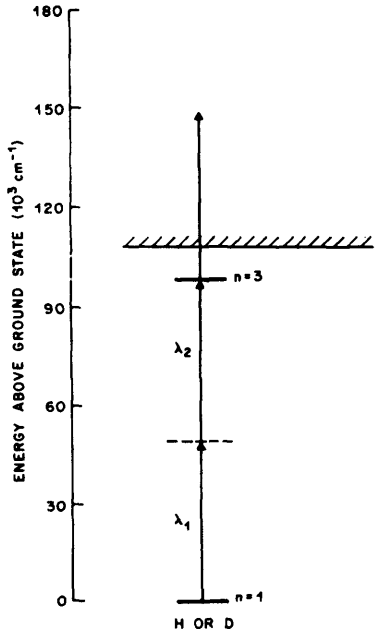

Figure 4.8. Schematic diagram of the REMPI scheme used for H-atom and D-atom REMPI through the n=3 state. Figure taken from reference [7].

The H-atom and D-atom sources were both characterised through using the REMPI technique. Figure 4.9 shows REMPI signals obtained from this experiment for both H and D atoms.

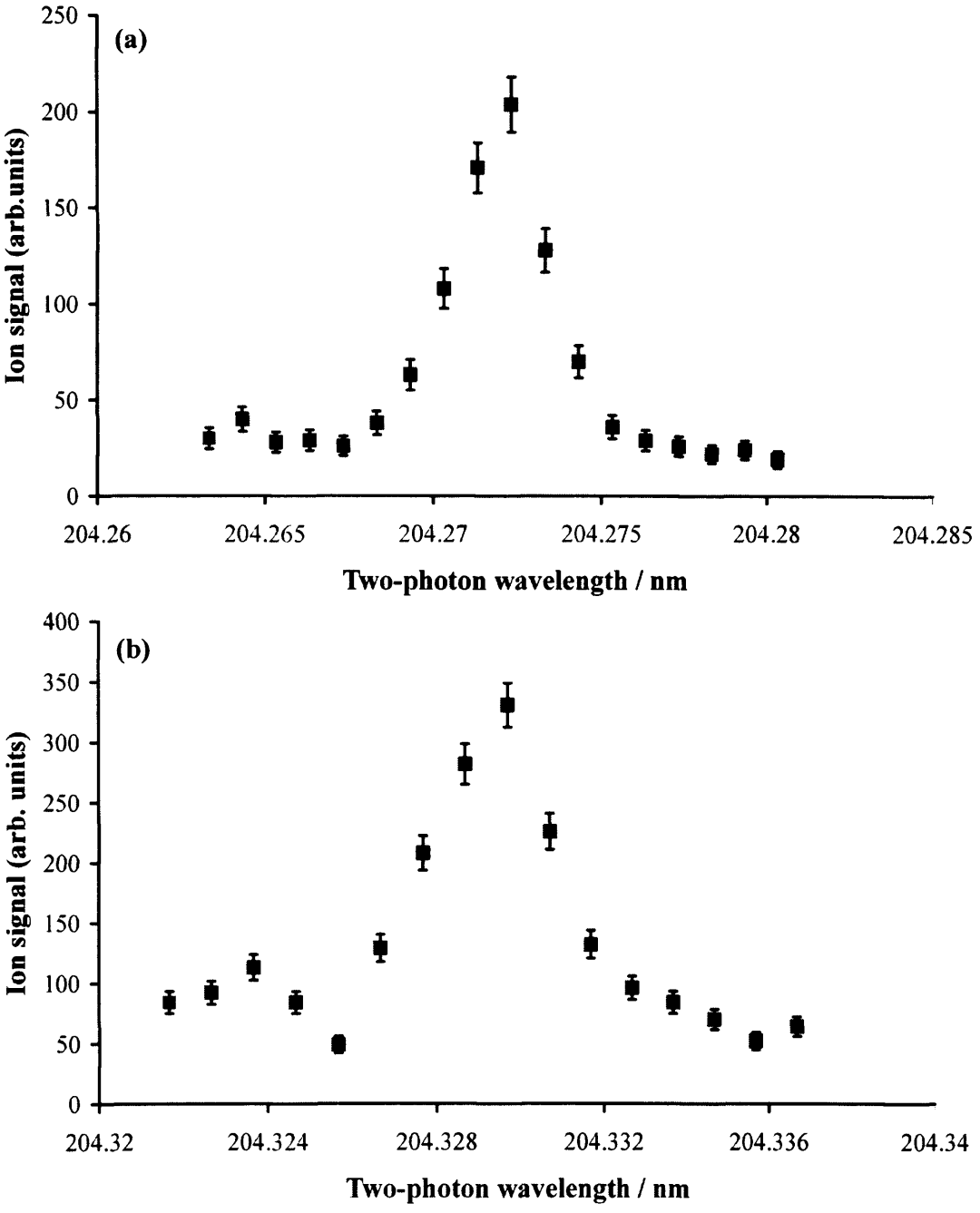

Figure 4.9. Example REMPI spectra of (a) D-atoms and (b) H-atoms through the n=3 states of each atom. For each spectrum, the accumulation time at each point was 100 seconds.

As described in Chapter 2, the sources require conditioning over several hours to achieve maximum atom production. It is also vitally important to ensure there are no leaks on the gas line system, since any trace of air in the cells can affect the

production of atoms, and it has been observed that a drop in H-atom or D-atom signal intensity can be attributed to a leak on either of the gas lines.

From earlier experiments, it was known that the intensity of the H-atom REMPI signal, and hence the amount of H-atom flux, depended on the pressure of the gas in the Pyrex cell. Experiments were carried out to determine the best operating pressure to give maximum H-atom and D-atom production in both the atom source cells. Figure 4.10 below shows a plot of the intensity of the signal versus cell pressure for each atom source. It was found that the maximum signal for the H-atom source was at 0.65 Torr in the Pyrex cell and the maximum signal for the D-atom source was found to be at 0.5 Torr in the Pyrex cell.

It was found, through a similar set of experiments, that varying the microwave power had little effect on the intensity of the ion signals for the H-atoms and D-atoms, although a power of 180 W gave a slightly stronger signal. This result is shown in Figure 4.11 below.

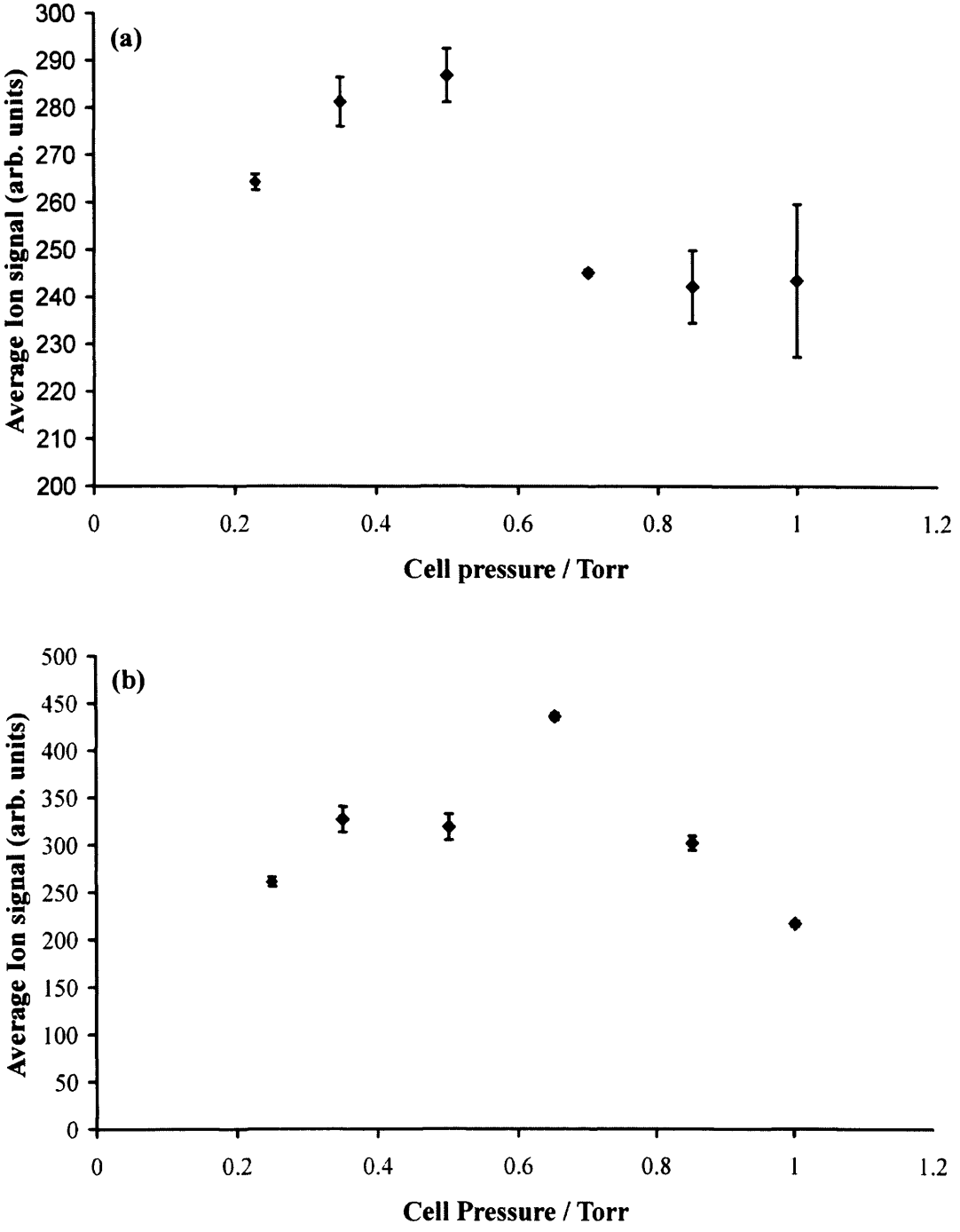

Figure 4.10. Graphs to show ion signal dependence on the pressure in the Pyrex cells. (a) shows the result for the D-atom source, with a peak at 0.5 Torr and (b) shows the result for the H-atom source, with a peak at 0.65 Torr.

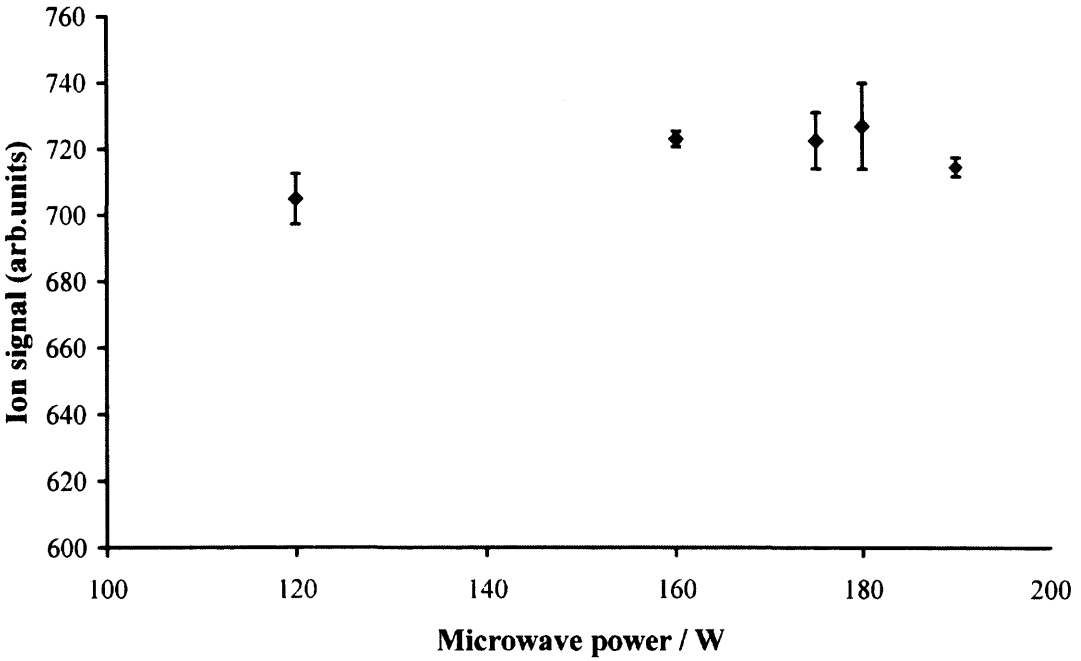

Figure 4.11. Graph to show the effect of changing the microwave power on the H-atom signal strength. It is clear that there is little difference between the points, but 180 W gives a slightly better signal.

From the REMPI peaks, it is possible to estimate the flux of H and D atoms into the source chamber [8, 9]. This is done using the following equation:

$$S = N_i(\sigma_{2ph} I) I_1 l V \tau \frac{\sigma_i I_1}{\sigma_i I_1 + A} C \qquad 4.1$$

where:

S is the ion signal per laser pulse

N_i is the ground state ion population

σ_{2ph} is the two-photon cross section for the transition ~ 1×10^{-28} cm^4 W^{-1}

I is the intensity of the laser ~ 1×10^{8} W cm^{-2}

I_1 is the intensity of the laser 1×10^{26} photons cm^{-2} s^{-1}

σ_I is the photo-ionisation cross section ~ 1×10^{-18} cm^{-2}

l is the length of the ionisation region ~ 0.5 cm

V is the area of the ionisation region = 7×10^{-4} cm^2

τ is the length of one laser pulse = 4 ns

A is 1/lifetime of n = 3 level = $1/17\times10^{-9} = 58.8\times10^{6}$ s^{-1}

C is the instrumental detection efficiency ~ 0.1

The cross section values given above are taken from reference [8].

Using the data from a typical H-atom signal, it was found that there were 1300 counts under the REMPI peak in 6 laser steps (0.003 nm steps). The accumulation time at each laser step was 100 seconds. Therefore, if all the counts in the peak were from H atoms, S can be determined *via*

$$\frac{1300}{100} = 13.00 \text{ counts per second which is } \sim 1.3 \text{ counts per pulse.}$$

Putting the values into 4.1 gives:

$$1.3 = N_i 1\times10^{-7} \qquad 4.2$$

so

$$N_i = \frac{1.3}{1\times10^{-7}} = 1.3\times10^{7}\,\text{cm}^{-3} \qquad 4.3$$

The speed of H at 300 K is ~ 3×10^{5} cm s^{-1} so the flux is $N_i v \sim 4 \times 10^{12}$ cm^{-2} s^{-1}.

The same reasoning can be used for the D-atom flux. Taking a typical D-atom REMPI peak, it was found that there were 740 counts under the peak in 6 steps (0.003 nm steps). The accumulation time at each step was 100 seconds. This gives 7.40 counts per second or 0.74 counts per pulse. Using the above equations, and a velocity for D atoms at 300 K of ~2×10^{5} cm s^{-1}, this results in a D-atom flux of ~2×10^{12} cm^{-2} s^{-1}.

Once both the atom sources had been characterised, it was then necessary to check that no HD was forming either in the source chamber, for example through back diffusion through the holes in the plugs in the PTFE lines, or else in the target chamber without the target in place. The reason for this was to make sure that any ro-vibrationally excited HD that was observed in the experiments had actually formed on the HOPG target surface and had not come from anywhere else in the experimental set-up. Various tests were carried out to ensure that the observed HD was from the target surface and the results of these tests will be described in detail in Chapter 5.

4.2. Summary

This chapter has described the reasons for introducing and the commissioning of a new atom source to allow the study of HD formed on a HOPG surface. Chapter 5 will describe the results obtained from this experimental arrangement.

4.3. References

1. Perry, J.S.A., Gingell, J.M., Newson, K.A., To, J., Watanabe, N., and Price, S.D., *Meas. Sci. Technol.*, 2002. **13**: p. 1414-1424.
2. Koch, N. and Steffens, E., *Rev. Sci. Instrum.*, 1999. **70**(3): p. 1631-1639.
3. Walraven, J.T.M. and Silvera, I.F., *Rev. Sci. Instrum.*, 1982. **53**(8): p. 1167-1181.
4. Audibert, M.M., Joffrin, C., and Ducuing, J., *Chem. Phys. Lett.*, 1974. **25**(2): p. 158-163.
5. Flower, D.R., *J. Phys. B-At. Mol. Opt. Phys.*, 2000. **33**(22): p. 5243-5249.
6. Pogrebnya, S.K., Mandy, M.E., and Clary, D.C., *Int. J. Mass Spectrom.*, 2003. **223**(1-3): p. 335-342.
7. Bokor, J., Freeman, R.R., White, J.C., and Storz, R.H., *IEEE J. Quantum Electron.*, 1981. **17**(12): p. 223-223.
8. Pozgainer, G., Windholz, L., and Winkler, A., *Meas. Sci. Technol.*, 1994. **5**(8): p. 947-953.
9. Demtroder, W., *Laser Spectroscopy*. 2 ed. 1996, Berlin: Springer.

Chapter 5. Results

5.1. Overview

In this Chapter, the results obtained from the UCL cosmic dust experiment for this thesis will be presented. The experimental methods and the data analysis procedures will be described in section 5.2. Sections 5.3-5.7 will detail the results obtained for the formation of H_2 and HD formed on HOPG at various surface temperatures. Section 5.8 will describe a kinetic model that has been used in order to model the coverage of H_2 on the HOPG surface under the current experimental conditions. In section 5.9, the experimental results are used to determine the partitioning of the energy released on the formation of H_2 and HD. All the results are discussed and compared with the literature in section 5.10.

5.2. Experimental Methods

This section details the procedures followed to carry out the experiments and collect the data to determine rotational populations. These experiments result in the determination of an average rotational temperature of the nascent molecules formed on the HOPG surface.

For the H_2 experiments described in this chapter, the pressure in the H-atom source was set to 2.4 Torr, resulting in a target chamber pressure of 5×10^{-8} Torr. This pressure in the H-atom source was found to give the best flux of H-atoms to the target surface, as described in Chapter 2. Following the introduction of the D-atom source, new Pyrex cells for both atom sources were used. As described in Chapter 4, it was found that the optimum cell pressures for maximum atom flux was 0.5 Torr in the D-atom source and 0.65 Torr in the H-atom source. The new optimum pressure for the H-atom source (0.65 Torr instead of 2.4 Torr) is attributed to the different

Pyrex cell used, the slight difference in the size of the capillary at the exit of the Pyrex cell, and possibly the fact that the microwaves are now distributed between two Pyrex cells.

Once it has been decided which ro-vibrational line of a newly formed molecule to search for, the 2-photon wavelength required for the REMPI process to take place is determined from the spectroscopic constants, as described in Chapter 3. Laser calibration experiments using CO, a molecule that has many rotational lines close together in its REMPI spectrum, have shown that the laser described in Chapter 3 has an offset of approximately 0.75 nm in the 2-photon wavelength range. This offset means that the wavelength at which a REMPI peak appears in the spectrum will be ~0.75 nm lower than the wavelength expected from the calculations using the spectroscopic constants. This discrepancy is not because the wavelength at which the line occurs is incorrect, just that the inbuilt calibration of the laser is not perfectly accurate. Hence, if a rotational line of H_2 is calculated at, for example, 202 nm (v'' =0, J'' = 1) then this line will be observed at approximately 201.25 nm using this particular laser, described in Chapter 3. This laser 'offset' has been found to be constant with wavelength; therefore, the separation between the rotational lines in the spectra taken with this laser will be the same as the separation between the calculated lines. Hence, it is possible to ensure that the rotational line observed is correct, from the separation between the rotational lines in the experimental spectrum. As described in Chapter 3, the REMPI signals observed arise from Q-branch transitions, where $\Delta J = 0$ since these transitions are much stronger than the O or S branch transitions which also arise from the (2+1) REMPI process.

In order to record the data from the REMPI process, the data collection PC for the time-of-flight mass spectrometer (TOFMS) uses a program to communicate with the laser. The program sets a wavelength range over which to scan the laser in small, incremental steps. The step-size is typically 0.001 – 0.003 nm. The laser can be set to dwell at each wavelength of the scan for a specific accumulation time. Depending on the strength of the signal, these accumulation times range from 20 seconds (for

H_2 or HD in $v'' = 0, J''$) up to 200 seconds (for H_2 or HD in $v'' = (1, 2), J''$). It can take many hours to scan over several nanometres with small steps (0.002 nm) and long accumulation times (200 s) and so in order to speed up the process, 'rough scans' are performed over a larger wavelength range, using large steps (0.003 - 0.005 nm) and shorter times, in order to determine the position of a rotational line. The laser is then set to scan over the line using longer accumulation times, and smaller steps to ensure the best possible signal to noise ratio. Figure 5.1 shows a typical REMPI scan achieved in the manner described. The area under the peak is proportional to the rotational population and the peak areas are converted into rotational populations, as described in detail below. Prior to each experimental run, the target is heated to 500 K and allowed to cool back down to the base temperature before the laser scan is initiated. This heating and cooling process takes approximately 20 minutes in total. As described in Chapter 2, the atom sources are run constantly, including during the heating and cooling process.

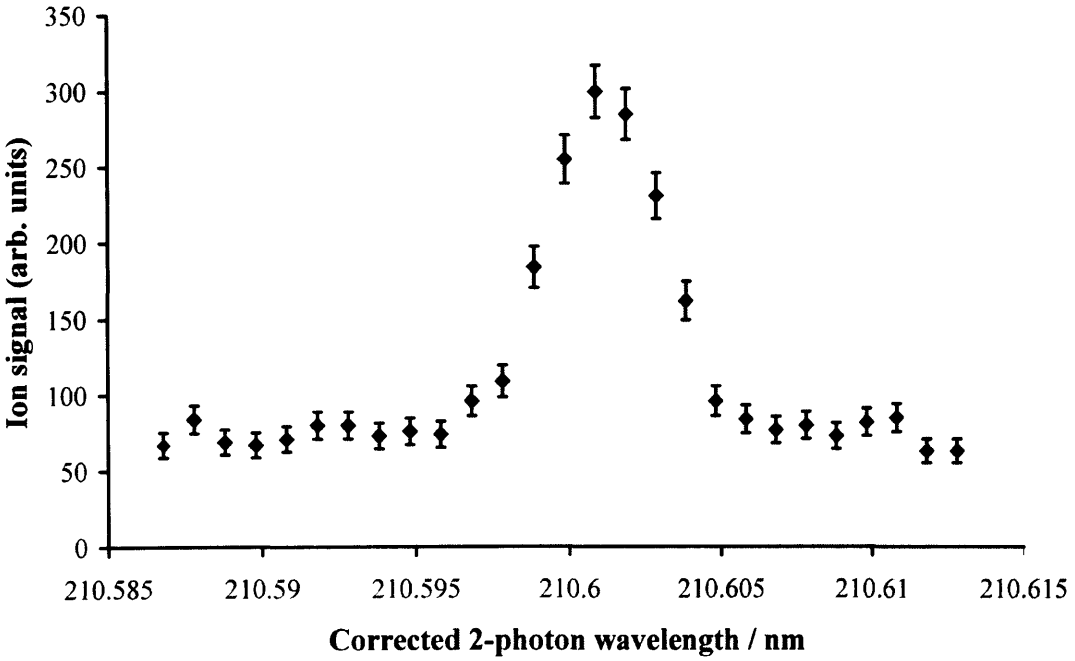

Figure 5.1. Plot showing the result of a typical REMPI scan using the laser system. This peak is for H_2 formed in rovibrational level $v'' = 1$ $J'' = 1$.

In order to correctly determine the rotational populations of the newly formed molecules, the counting electronics of the TOFMS are set to integrate only over flight times which contain the relevant ions. To determine the flight times of the relevant masses, a photoelectron mass spectrum is taken. This is achieved by allowing the 'off resonance' laser beam into the chamber. The laser beam creates photoelectrons through stray photons hitting the stainless steel walls of the chamber and releasing electrons. These photoelectrons then ionise the gas in the chamber from which H_2^+ can be easily identified in the mass spectrum. These photoelectrons are responsible for the higher background counts in a H_2 REMPI spectrum compared with a HD REMPI spectrum, as there is a significant amount of H_2 gas present in the background gas of the chamber. An integration window, encompassing only the H_2^+ peak, can then be chosen for recording the ions during the experiment. An example photoelectron mass spectrum is shown in Figure 5.2 below. Since it is known where the H_2^+ and H^+ peaks appear in the photoelectron mass spectrum, the time of flight of HD^+ and D_2^+ can also be determined from the mass spectrum.

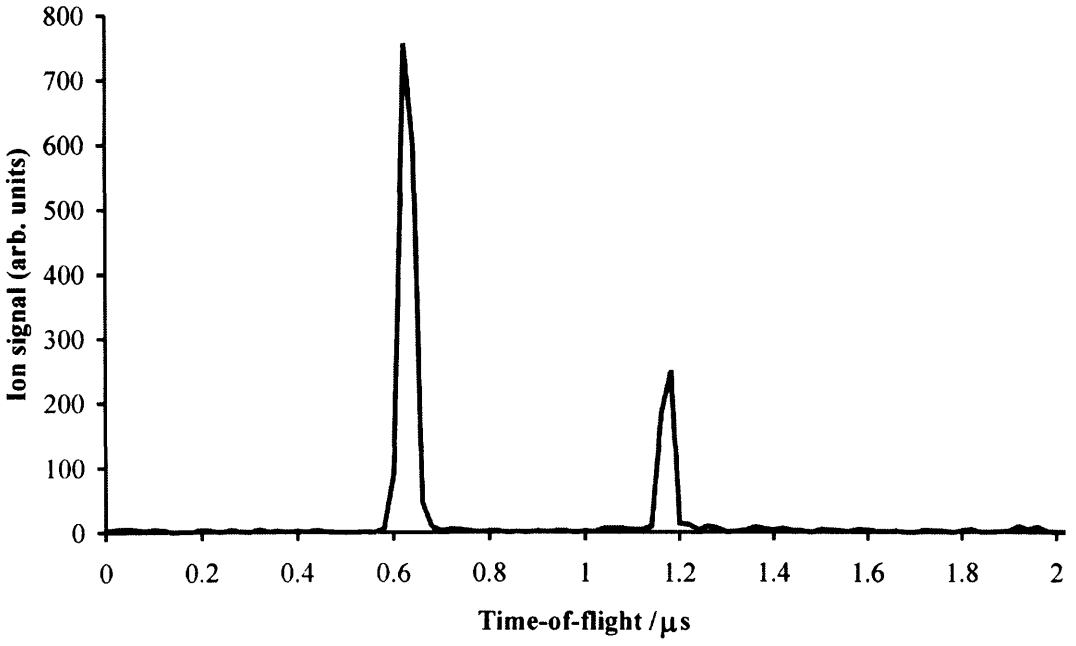

Figure 5.2. Plot showing a photoelectron mass spectrum. The peak at lower flight times is for H^+ and the peak at longer flight times is H_2^+. This spectrum was taken with -1900 V on the MCP.

The electronics of the TOFMS used to count the ions are only fast enough to accurately count one ion of a given mass per laser shot. This is because of the 'dead time' associated with the constant fraction discriminator, which means that any molecules which arrive at the detector within this dead time will not be counted. The laser runs at a repetition rate of 10 Hz so to avoid counting an incorrect number of ions per wavelength step, the laser power must be low enough to fulfil the following relationship:

$$\frac{\textit{Ion of a given mass count per laser step}}{10 \times \textit{(accumulation time)}} \leq 1$$

If necessary, the laser power can be adjusted to ensure that this condition is met.

5.2.1. Calibration of Laser Power

The output power of the laser varies as it scans across a wavelength range, due to the laser dyes used having output powers which are wavelength dependent. Since the laser tracking system described in Chapter 3 is not always perfectly efficient, inadequate phase-matching of the doubling and tripling optics can also occur, which will affect the laser output power. In order to record accurate rotational populations of the internal energy states of the newly formed molecules, the signal area must be corrected for laser power. The intensities of the ion signals detected using the TOFMS vary with the laser output power and this variation follows a power law [1, 2].

$$\textit{Ion signal} \propto \textit{(laser power)}^n$$

In order to determine the value of n in the above equation, ion signals were measured for different laser output powers. Plotting a graph of ln(laser power / mJ) versus ln(ion signal) gives a straight line with a gradient n. This was done for H_2 $v''= 0,1$ and 2 and HD $v'' = 0,1$ and 2. An example plot is shown in Figure 5.3 below. The values for n used for each v'' state of H_2 and HD are given in Table 5.1

below. Within the error limits, the values of n for each v'' state are very similar and these values are in good agreement with the work of other groups [1, 2]. An average value for n is used for each vibrational state, regardless of the rotational level of interest. The populations of the rotational states are corrected for laser power by dividing the areas of the TOFMS peaks by the laser power raised to the relevant value of n.

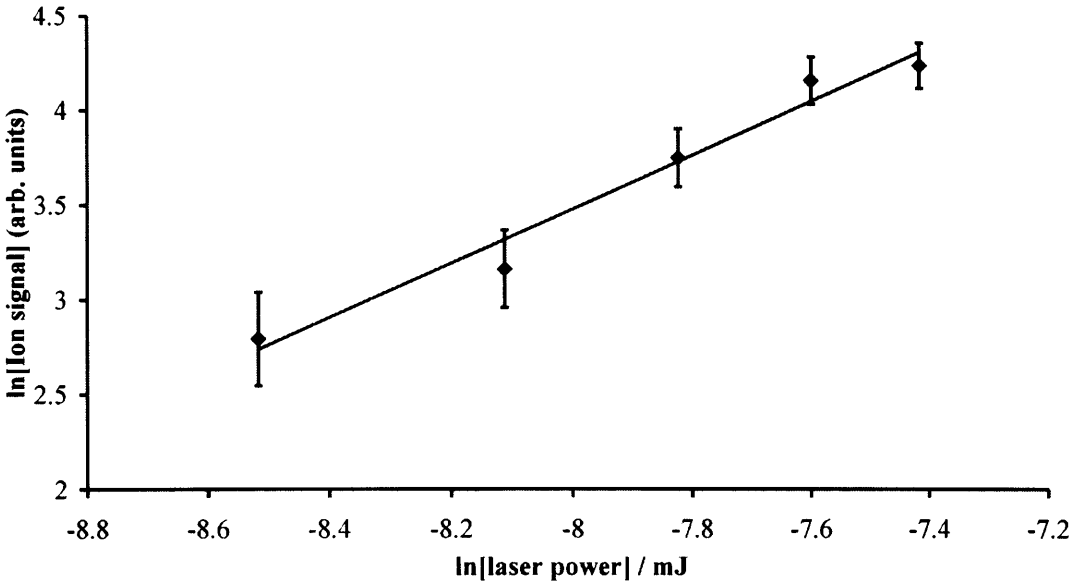

Figure 5.3. Plot of ln(Ion signal) vs ln(laser power) to determine the laser power dependence factor for H_2 formed in $v'' = 2$. The solid line is a weighted least squares fit, the gradient of which gives the value of n as described in the text.

Table 5.1. Table to show laser power dependence factors determined for each vibrational state of H_2 and HD.

Particular	Vibrational level	n
H_2	0	1.47 ± 0.14
	1	1.48 ± 0.16
	2	1.43 ± 0.23
HD	0	1.96 ± 0.21
	1	2.03 ± 0.24
	2	1.55 ± 0.39

Since the ionisation dependence on the laser power follows a power law, a non-saturating 3-photon process (that is, a process which depends on the photon flux density) would be expected to give a value of $n = 3$. If either the ionisation step or 2-photon resonance step of the (2+1) REMPI process were saturating, a value between $n = 2$ and $n = 3$ would be expected [1, 2]. Since the values of n obtained are all less than 2 (within the error limits), this indicates that both the ionisation and 2-photon resonance steps are saturated in this case [1, 2].

5.2.2. Determination of Rotational Temperature

Once the rotational populations have been determined, it is possible to calculate a characteristic rotational temperature for each vibrational level. This temperature determination is achieved by creating a Boltzmann plot. The Boltzmann distribution describes the population of the rotational levels P_J relative to the population of the $J = 0$ level:

$$\frac{P_J}{P_0} = g_J(2J+1)\exp\left(-\left(\frac{E_J}{kT}\right)\right) \qquad 5.1$$

where g_J is the nuclear spin degeneracy (for hydrogen, $g_J = 1$ for para states and $g_J = 3$ for ortho states), k is Boltzmann's constant, J is the rotational quantum number, E_J is the corresponding rotational energy and T is the temperature.

Rearranging equation 5.1 gives:

$$-k\ln\left(\frac{P_J}{g_J(2J+1)}\right) + k\ln(P_0) = \frac{E_J}{T} \qquad 5.2$$

It is then clear that plotting $-k\ln\left(\frac{P_J}{g_J(2J+1)}\right)$ vs. E_J gives a straight line with gradient 1/T and intercept $k\ln(P_0)$.

If the rotational populations determined from the REMPI peaks lie on this straight line, then the distribution is Boltzmann and the gradient of a least squares fit to the data can be used to determine the rotational temperature, T. However, if the points do not lie on a straight line, the rotational distribution is non-Boltzmann but it is still possible to determine an average rotational energy and hence, an average rotational temperature. This can be done using statistical mechanics as described below.

The average rotational energy, E_{rot} is given by:

$$\langle E_{rot} \rangle = \sum_J P_J E_J \qquad 5.3$$

and the average rotational temperature is then given by:

$$\langle T_{rot} \rangle = \frac{\langle E_{rot} \rangle}{k} \qquad 5.4$$

A line of best fit to a Boltzmann plot in which the data points do not necessarily lie on a straight line can also give us the average rotational temperature from the gradient.

The rotational populations themselves are found from the following equation

$$P_J = \frac{I_J}{\sum_J I_J} \qquad 5.5$$

where I_J is the power normalised ion signal detected for the rotational state J.

5.2.3. H_2 Boltzmann Distribution at Room Temperature

For H_2 gas at room temperature, the rotational distribution is expected to be Boltzmann [1]. Hence, if the REMPI/TOF system used in this experiment is detecting rotational populations accurately, a room temperature REMPI experiment on H_2 gas should give the required Boltzmann distribution. Figure 5.4 shows a

comparison between data taken with this laser system and a predicted Boltzmann plot for H_2 at 295 K. It is clear that there is good agreement between the two, showing that this experiment should give accurate ro-vibrational distributions and rotational temperatures for H_2 formed on cosmic dust-like targets at low temperatures.

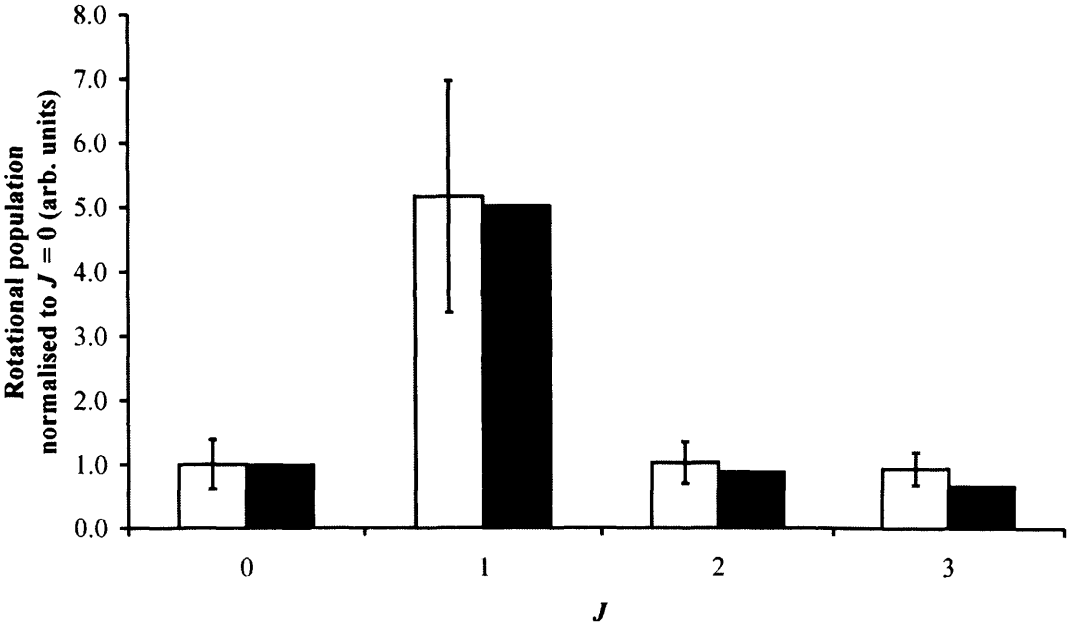

Figure 5.4. Rotational populations for ground state ($v'' = 0$) H_2 gas at 295 K, normalised to $J' = 0$ (white columns), compared with the expected Boltzmann distribution (black columns).

5.3. H_2 Formation on HOPG

In this section, the results obtained for the formation of H_2 from H-atoms recombining on HOPG will be described. For the results shown, only the data for H_2 formed in $v'' = 1$ at 23 K and in $v'' = 2$ at 15 K and 23 K were recorded for this thesis. The other results were taken on the same equipment prior to the author starting experiments and are included in order to enable a complete discussion of the results and their implications.

5.3.1. H_2 formed in $v''= 1, J''= 0$-3

REMPI signals were detected for H_2 formed in $v'' = 1$, $J' = 0$-3 with the target temperature held at 23 K. REMPI signals from higher J'' levels in $v'' = 1$ were searched for but no signals were observed above the detection limit. The background count level in the H_2 experiments is around 20-50 counts in 200 seconds. The background count is much lower for the HD experiments described below, around 5-10 counts in 200 seconds. The REMPI signals observed for H_2 $^1\Sigma_g^+ X$ ($v''= 1, J' = 0$-3) $\rightarrow$ $^1\Sigma_g^+ E,F$ ($v' = 0, J' = J''$) are shown in Figure 5.5. The signals for each J'' state were not all taken at the same time, this is because the line separation between adjacent rotational lines in H_2 is very large and hence the time taken to scan the whole spectrum would run into days, at the necessary accumulation times.

As discussed above, the H_2^+ signals recorded by the mass spectrometer are converted into relative rotational populations which are listed below in Table 5.2.

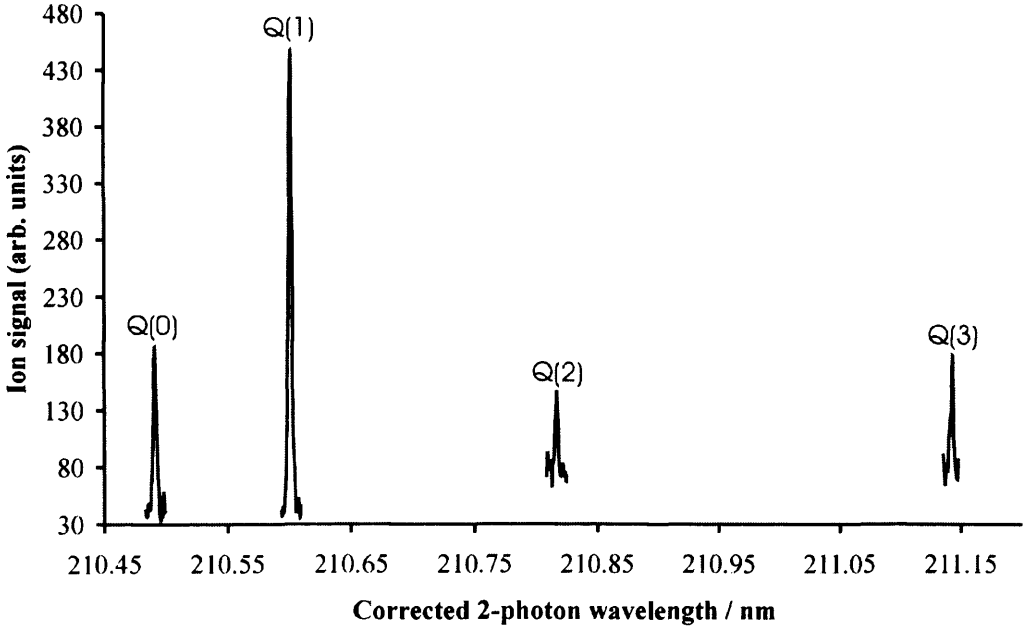

Figure 5.5. REMPI plot showing the transitions $^1\Sigma_g^+ X$ ($v'' = 1, J' = 0$-3) $\rightarrow$ $^1\Sigma_g^+ E,F$ ($v' = 0, J' = J''$) for H_2 formed by recombination of H-atoms on a HOPG surface held at 23 K. The entire spectrum was not taken at the same time due to the large separation between the rotational lines and the long accumulation times necessary to obtain good signal to noise.

Table 5.2. Relative rotational populations for H_2 $v'' = 1$, recorded at a target temperature of 23 K.

J''	Relative population
0	1.00 ± 0.07
1	4.73 ± 0.26
2	0.93 ± 0.09
3	0.68 ± 0.07
4	0.19 ± 0.17

As shown in Table 5.2 the experimental signal from $J'' = 4$ is effectively zero within the experimental error bar. An average rotational temperature for this vibrational level was determined from the Boltzmann plot of these relative populations shown in Figure 5.6 in the way described above in section 5.2.2. Applying a weighted least squares fit to this data yields a rotational temperature of 314 ± 9 K.

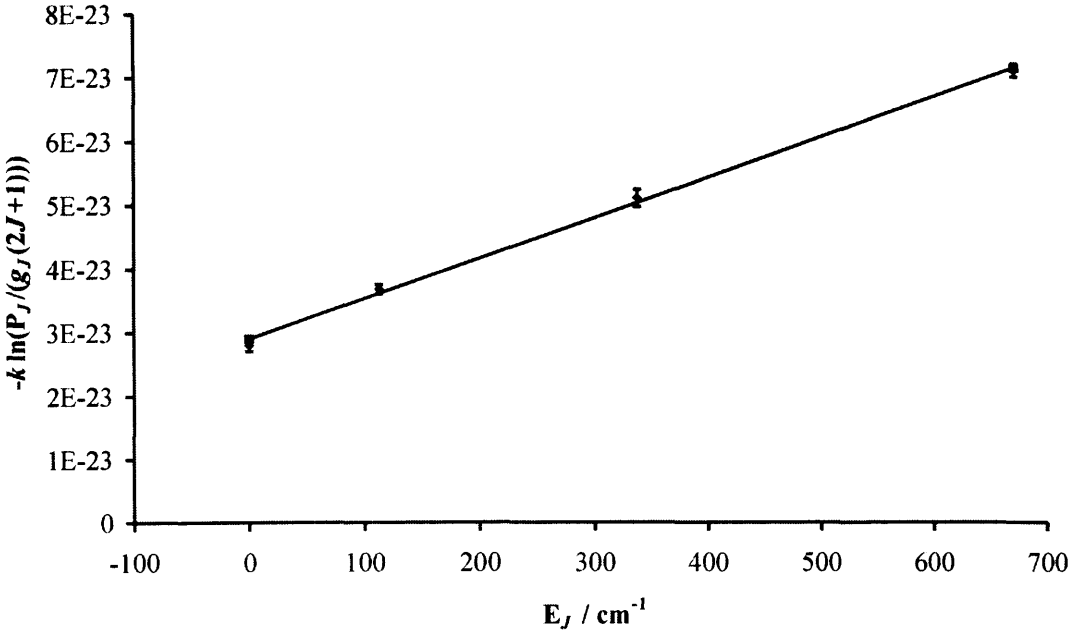

Figure 5.6. Boltzmann plot to determine the rotational temperature of H_2 formed on HOPG at a surface temperature of 23 K. The solid line is a weighted least squares fit to the data, the gradient of which yields the rotational temperature.

This analysis shows that the populations fit a Boltzmann distribution quite well. For all of the rotational temperatures given, the error stated is the standard deviation in

the gradient from a weighted least squares fit. This fitting procedure includes the uncertainties in the values of P_J due to the uncertainty in the laser power measurements and the statistical uncertainty of the experimental ion counts. A full description of the error analysis is given in Appendix B.

Previously published data [3] from this experiment, at target temperatures of 30 K and 50 K, is shown in Table 5.3 along with the above results at 23 K. The average molecular rotational temperatures are clearly much higher than the corresponding surface temperatures. In addition, the average rotational temperatures are all quite similar, perhaps with an upward trend in the rotational temperature at the lower surface temperatures.

Table 5.3. Rotational temperatures of H_2 formed in $v'' = 1, J = (0\text{-}3)$ at different surface temperatures.

Surface Temperature / K	Calculated Rotational Temperature / K
23	314 ± 9
30	214 ± 11
50	224 ± 21

5.3.2. H_2 formed in $v'' = 2, J'' = 0\text{-}3$

REMPI signals were also detected from H_2 formed in ro-vibrationally excited states $v'' = 2, J'' = (0\text{-}2)$ at surface temperatures of 15 and 30 K and in states $v'' = 2, J'' = (0\text{-}3)$ at HOPG surface temperatures of 23 and 50 K. As mentioned above, only the data at 15 and 23 K were taken by this author, the 30 and 50 K data have not been previously published and are included for completeness [4]. The REMPI spectra obtained for each of these temperatures are shown below in Figure 5.7 and Figure 5.8. As for the $v'' = 1$ data, no higher J'' states were observed above our detection limits. It is unclear why the $J'' = 3$ rotational level was not detected at 23 K and 50 K but this is likely to be due to the relatively small signal strengths and fluctuations in laser power.

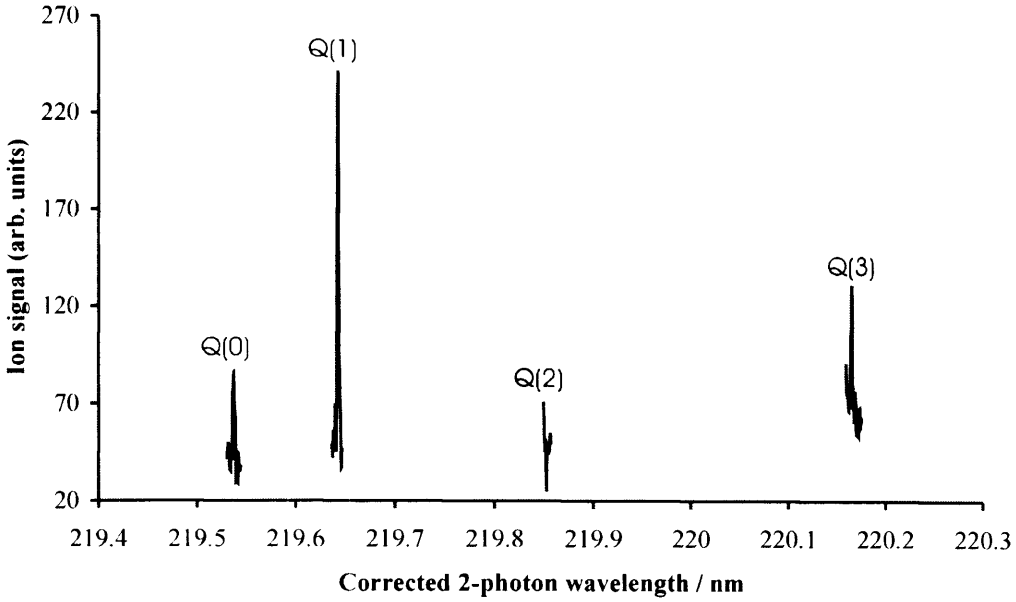

Figure 5.7. REMPI plot showing the transitions $^1\Sigma_g^+$ X ($v'' = 2$, $J'' = 0$-2) $\rightarrow$ $^1\Sigma_g^+$ E,F ($v' = 0$, $J' = J''$) for H_2 formed by recombination of H-atoms on a HOPG surface held at 15 K.

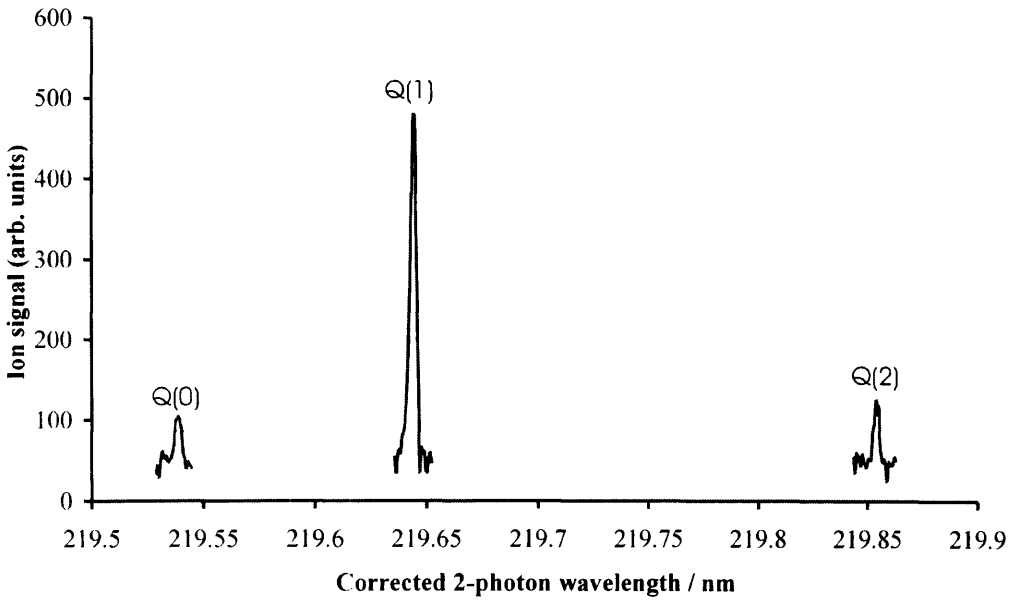

Figure 5.8. REMPI plot showing the transitions $^1\Sigma_g^+$ X ($v'' = 2$, $J'' = 0$-2) $\rightarrow$ $^1\Sigma_g^+$ E,F ($v' = 0$, $J' = J''$) for H_2 formed by recombination of H-atoms on a HOPG surface held at 23 K. Again, the entire spectrum was not taken at the same time. No signal was observed for $J'' = 3$ at this surface temperature.

Boltzmann plots were again constructed from the rotational populations obtained from the REMPI signals and were fitted with a weighted least squares fit, as shown below in Figure 5.9.

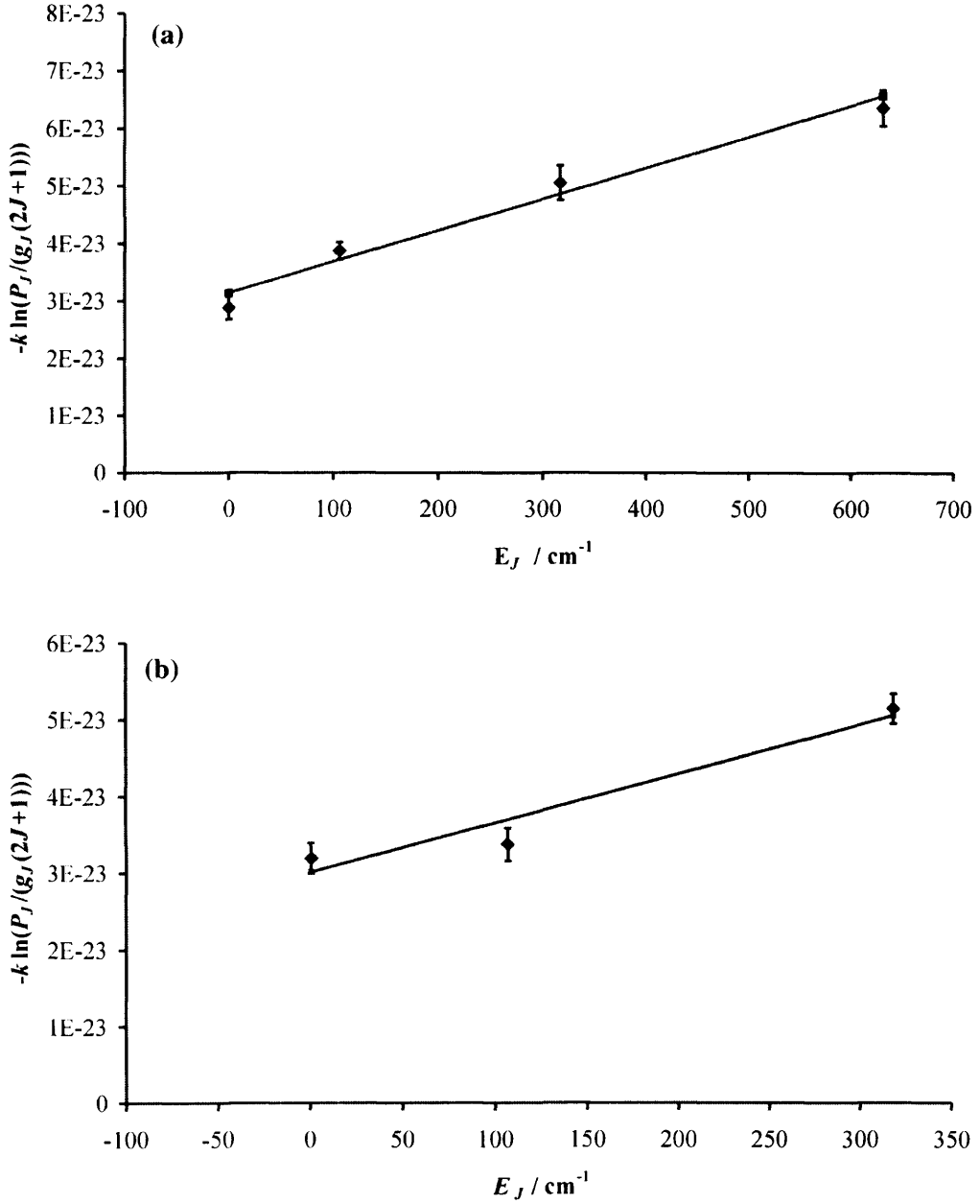

Figure 5.9. Boltzmann plot to determine rotational temperature of H_2 formed in $v'' = 2$ on HOPG at a surface temperature of (a) 15 K and (b) 23 K. The solid lines are weighted least squares fits to the data, the gradient of which yields the rotational temperatures.

These Boltzmann plots were again used to determine an average rotational temperature for the nascent desorbing molecules at each surface temperature. The relative rotational populations for each surface temperature are shown in Table 5.4 below and the rotational temperatures are shown in Table 5.5.

Table 5.4. Relative rotational populations NJ for H2 formed in v″ = 2 at various surface temperatures Tsurf.

J''	$N_J(T_{surf}=15\ K)$	$N_J(T_{surf}=23\ K)$	$N_J(T_{surf}=30\ K)$	$N_J(T_{surf}=50\ K)$
0	1.00 ± 0.14	1.00 ± 0.14	1.00 ± 0.27	1.00 ± 0.33
1	4.39 ± 0.49	7.92 ± 1.23	5.18 ± 1.35	4.91± 1.08
2	1.03 ± 0.22	1.21 ± 0.17	0.70 ± 0.21	1.35 ± 0.66
3	1.67 ± 0.38	0.33 ± 0.34	1.26 ± 0.37	0.15 ± 0.15
4	0.01 ± 0.34	-	0.05 ± 0.08	-

Table 5.5. Rotational temperatures of H_2 formed in v'' = 2, J' = (0-2,3) at different surface temperatures.

T_{surf} / K	Rotational Temperature / K
15	364 ± 37
23	309 ± 41
30	316 ± 41
50	345 ± 153

As was observed for the v'' = 1 results, the calculated rotational temperatures are much higher than the surface temperature and are also broadly similar to each other within the error limits. The rotational temperatures for the v'' = 2 data are all higher than those for v'' = 1 at the same surface temperatures, as shown in Figure 5.10.

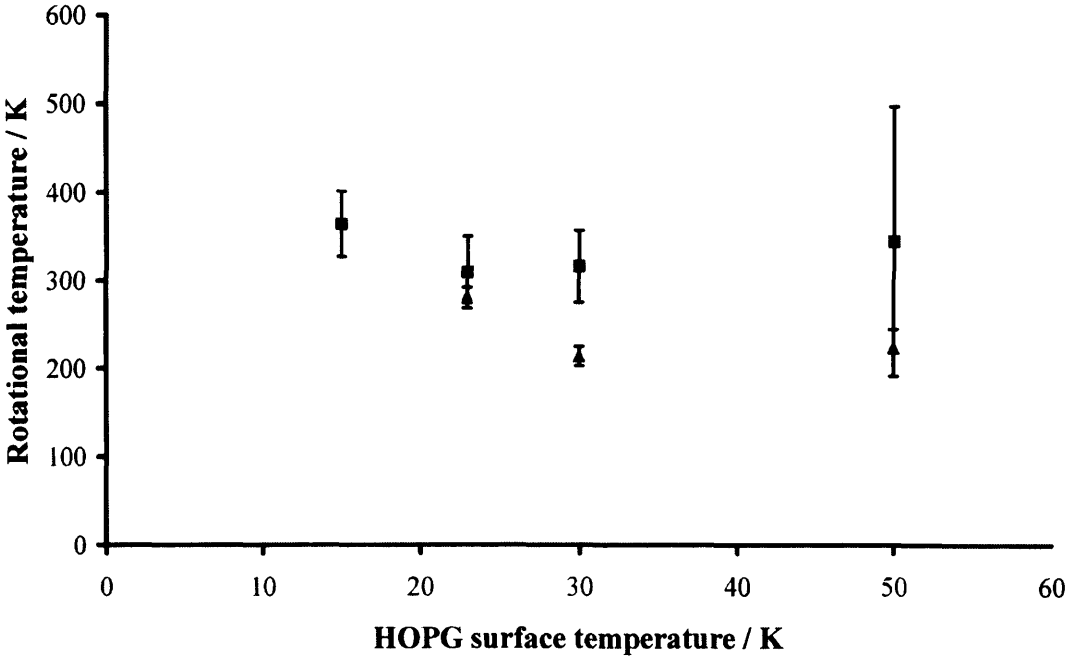

Figure 5.10. A plot of the average H_2 rotational temperature against surface temperature for the recombination of H atoms on HOPG. The ▲ symbol is for H_2 formed in $v'' = 1$ whilst ■ indicates H_2 formed in $v'' = 2$.

5.4. HD Formation on HOPG at Surface Temperatures 15 - 50 K

In this section, the results obtained for the formation of HD by recombination of H and D atoms on HOPG at surface temperatures of 15, 27, 40 and 50 K will be described. All the data presented in the following sections were recorded by the author. The origin of the REMPI signals for HD formation on a HOPG surface will be discussed in detail in section 5.10.1.2.

5.4.1. HD formed in $v'' = 1$, $J'' = 0$-4

Rotational populations for HD formation were recorded at target temperatures of 15, 27, 40 and 50 K for both the $v'' = 1$ and $v'' = 2$ vibrational levels, in order to enable a good comparison with the data for H_2 formation. As shown in Table 5.6 and Table 5.8, the signals for $J'' = 4$, in both vibrational states, are weak but for $v'' = 2$ are certainly above our detection limit at 15 K. These $J'' = 4$ signals are stronger at the

higher surface temperatures for both vibrational levels. Despite several searches, no signals were observed from $J' > 4$ rotational states. HD formed in $v'' = 1$, $J'' = 5$ would be expected to be observed at a wavelength of 210.2206 nm. As shown in Figure 5.11 below, no $J'' = 5$ signal is observable.

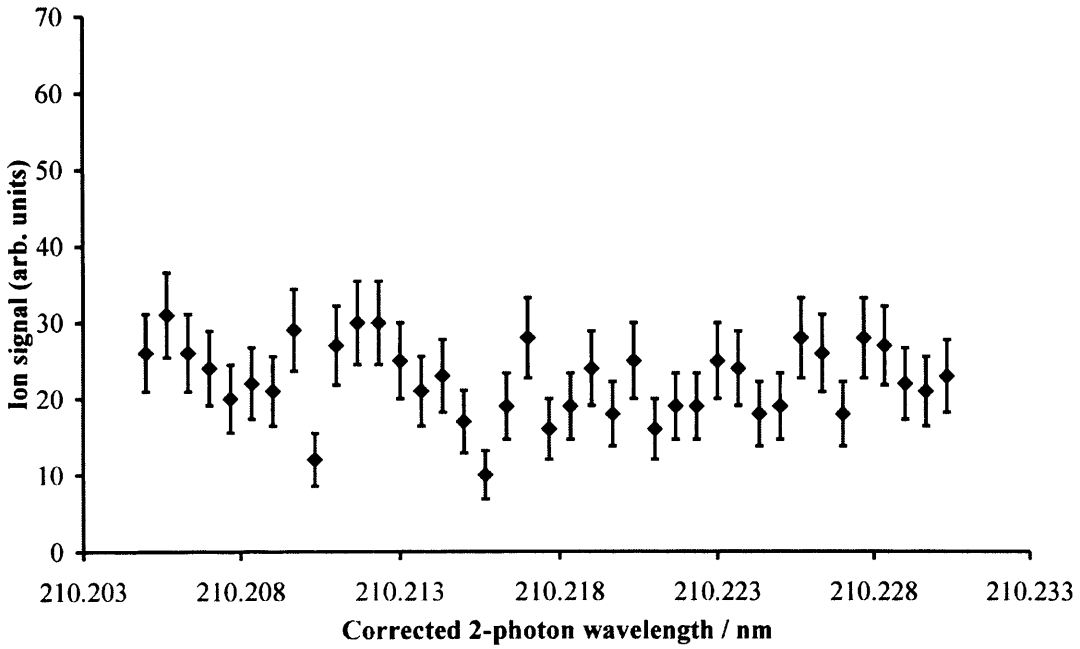

Figure 5.11. Plot showing attempts at finding a REMPI signal for HD formed in $v'' = 1$, $J'' = 5$ via the transition $E,F\,^1\Sigma_g^+$ ($v' = 1$, $J' = 1$) - $X\,^1\Sigma_g^+$ ($v'' = 0$, $J' = 1$). It is clear that there is no signal above the background.

As before, the surface was heated to 500 K prior to each experiment to desorb any impurities. The same HOPG sample as used for the H_2 experiments was employed for these experiments to study HD formation. REMPI spectra for the ionization of HD in $v'' = 1$ with $J'' = 0$-4 at the surface temperatures described are shown in Figure 5.12-5.15 along with the corresponding Boltzmann plots. The gradient of a weighted least squares fit to each data set was used to determine the average rotational temperature of the nascent HD molecules formed at each surface temperature.

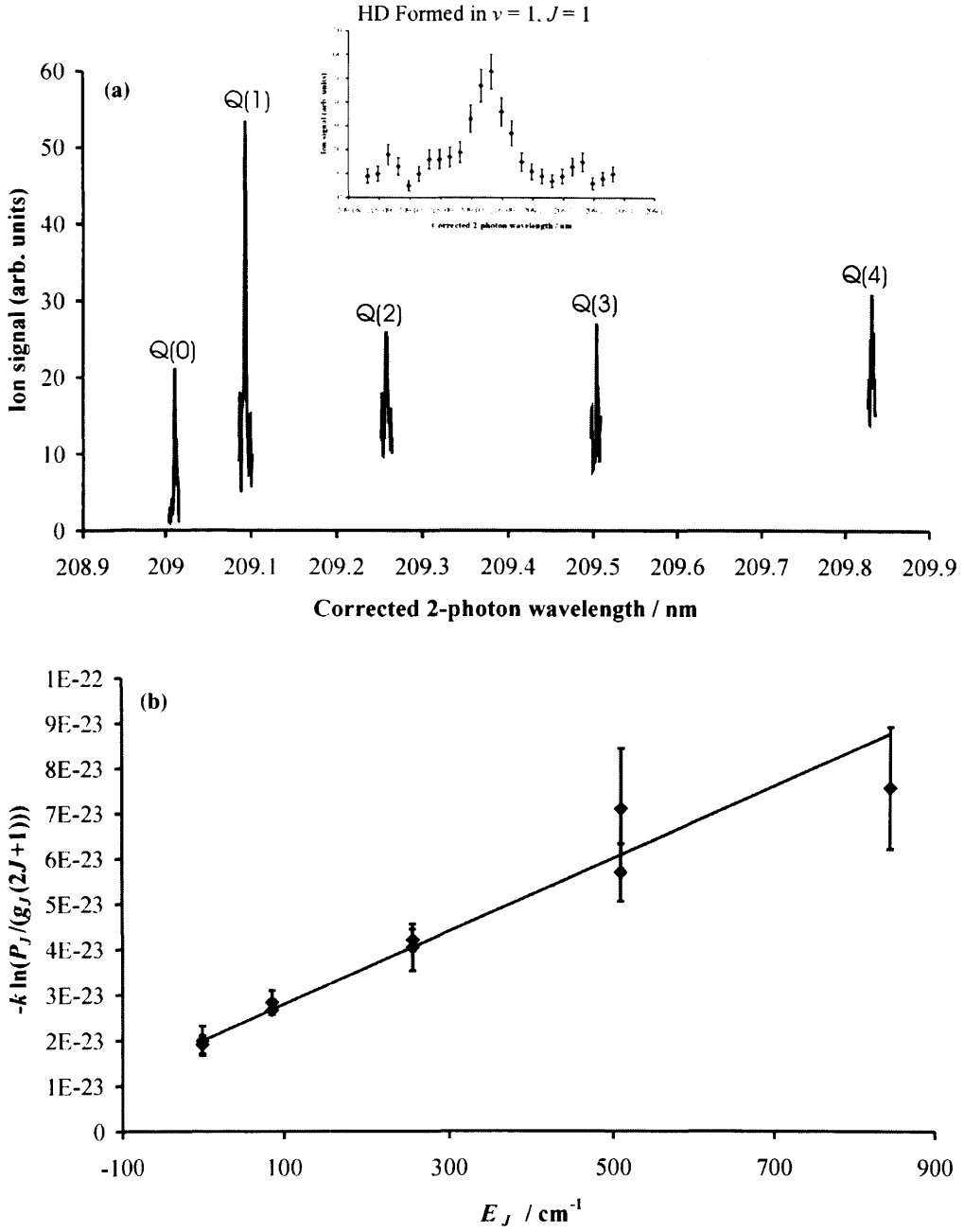

Figure 5.12. (a) shows the REMPI spectrum for the transitions $^1\Sigma_g^+$ X ($v'' = 1$, $J'' = 0$-4) $\rightarrow$ $^1\Sigma_g^+$ E,F ($v' = 0$, $J' = J''$) for HD formed on a HOPG surface held at 15 K. The inset picture shows the $v'' = 1$, $J'' = 1$ signal in close up, since the background on each signal is not clear when they are all plotted on the same graph. (b) shows the corresponding Boltzmann plot used to calculate the average rotational temperature of the molecules formed on the surface held at 15 K.

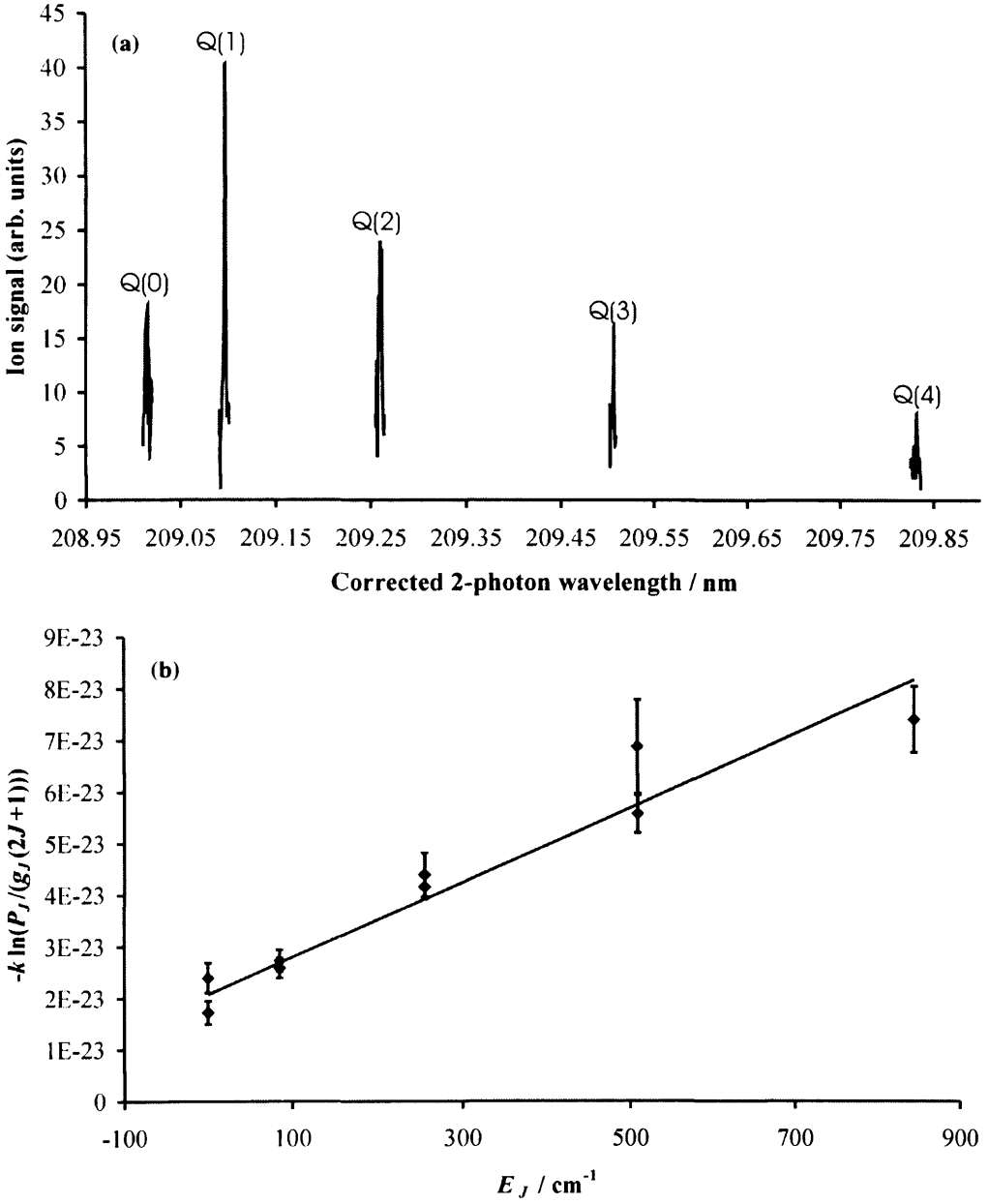

Figure 5.13. (a) shows the REMPI spectrum for the transitions $^1\Sigma_g^+$ X (v'' = 1, J'' = 0-4) → $^1\Sigma_g^+$ E,F (v' = 0, $J' = J''$) for HD formed on a HOPG surface held at 27 K. (b) shows the corresponding Boltzmann plot used to calculate the average rotational temperature of the molecules formed on the surface held at 27 K.

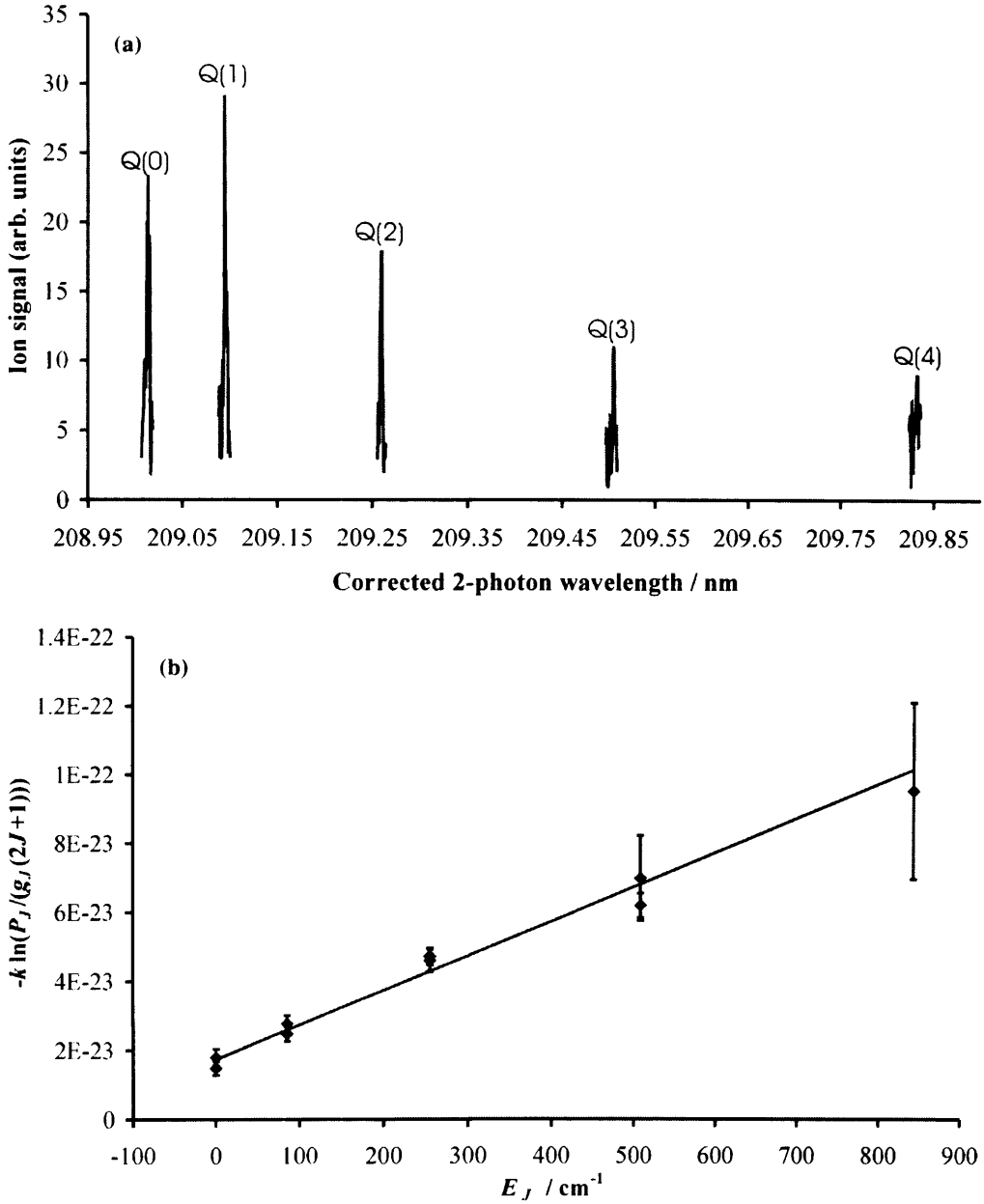

Figure 5.14. (a) shows the REMPI spectrum for the transitions $^1\Sigma_g^+$ X (v'' = 1, J'' = 0-4) → $^1\Sigma_g^+$ E,F (v' = 0, J' = J'') for HD formed on a HOPG surface held at 40 K. (b) shows the corresponding Boltzmann plot used to calculate the average rotational temperature of the molecules formed on the surface held at 40 K.

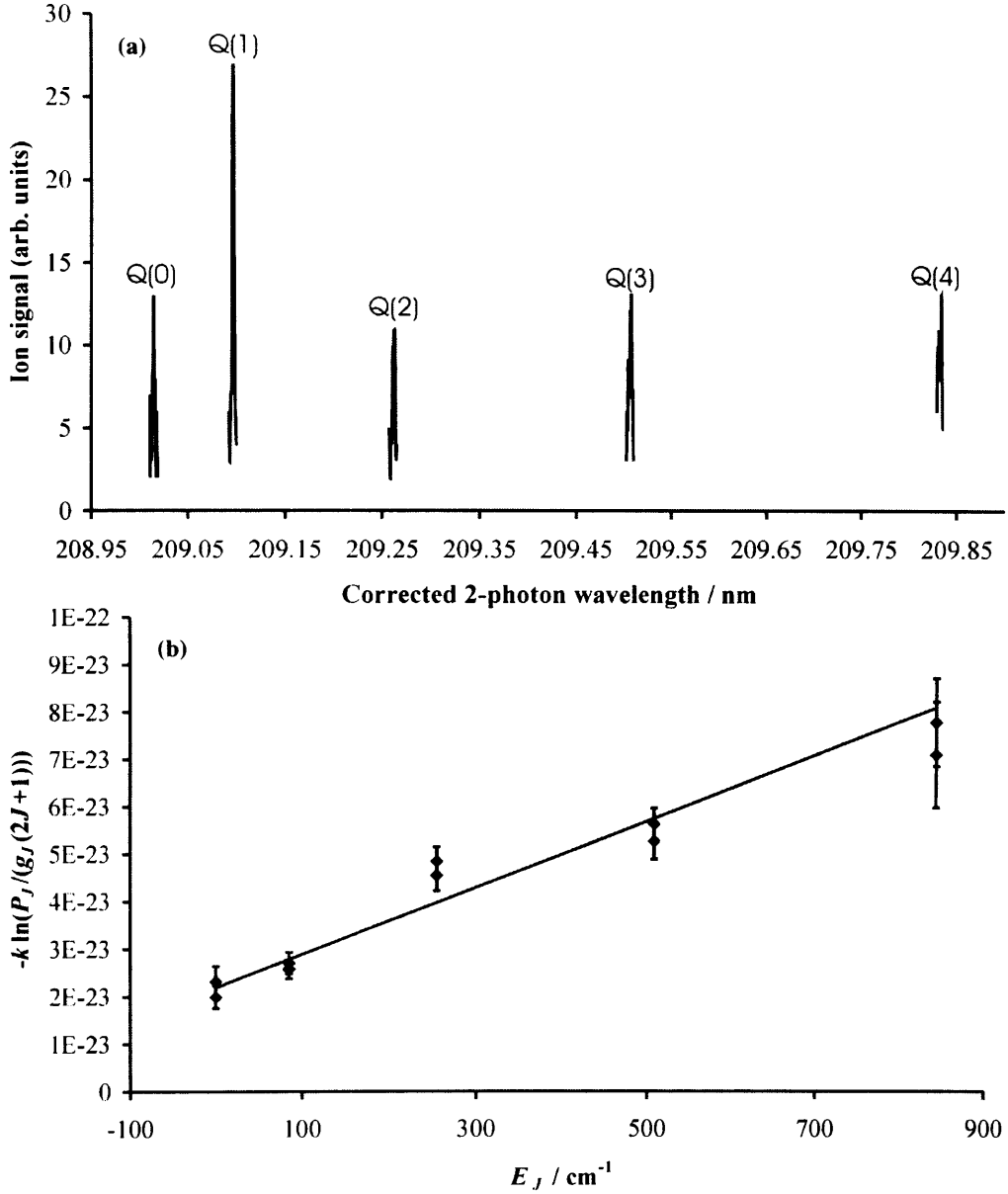

Figure 5.15. (a) shows the REMPI spectrum for the transitions $^1\Sigma_g^+$ X (v'' = 1, J'' = 0-4) → $^1\Sigma_g^+$ E,F (v' = 0, J' = J'') for HD formed on a HOPG surface held at 50 K. (b) shows the corresponding Boltzmann plot used to calculate the average rotational temperature of the molecules formed on the surface held at 50K.

The relative rotational populations for HD formed in $v'' = 1$, $J'' = 0$-4 at the surface temperatures indicated are given in Table 5.6 below.

Table 5.6. Relative rotational populations N_J for HD formed in v'' = 1 at various surface temperatures Tsurf. Two data sets are shown for each J'' state, the average value of the population is used to obtain the rotational temperature in the Boltzmann plot.

J''	$N_J(T_{surf}=15$ K)	$N_J(T_{surf}=27$ K)	$N_J(T_{surf}=40$ K)	$N_J(T_{surf}=50$ K)
0	1.00 ± 0.14	1.00 ± 0.16	1.00 ± 0.15	1.00 ± 0.17
	1.00 ± 0.18	1.00 ± 0.21	1.00 ± 0.18	1.00 ± 0.23
1	1.74 ± 0.12	1.66 ± 0.22	1.20 ± 0.20	1.97 ± 0.28
	1.88 ± 0.27	2.35 ± 0.36	1.84 ± 0.28	2.26 ± 0.37
2	0.95 ± 0.16	0.72 ± 0.22	0.48 ± 0.10	0.63 ± 0.14
	0.93 ± 0.18	1.38 ± 0.24	0.66 ± 0.15	0.99 ± 0.24
3	0.16 ± 0.16	0.17 ± 0.11	0.23 ± 0.06	0.50 ± 0.12
	0.69 ± 0.14	0.69 ± 0.19	0.16 ± 0.14	0.82 ± 0.23
4	0.15 ± 0.14	0.24 ± 0.11	0.02 ± 0.04	0.13 ± 0.09
	0.07 ± 0.10	-	-	0.28 ± 0.22

The average rotational temperatures obtained for HD formed in $v'' = 1$, $J'' = 0$-4 at the surface temperatures indicated are given in Table 5.7 below.

Table 5.7. Rotational temperatures of HD formed in $v'' = 1$, $J'' = (0\text{-}4)$ at different surface temperatures

T_{surf} / K	Rotational Temperature / K
15	265 ± 15
27	274 ± 20
40	198 ± 13
50	283 ± 20

It is clear that the average rotational temperature of the newly formed molecules is much higher than the temperature of the surface on which they were formed, a result similar to that for H_2 formation. Again, the rotational temperatures for each surface temperature are all reasonably similar to each other.

5.4.2. HD formed in $v'' = 2$, $J'' = 0$-4

The REMPI plots obtained for HD formed on HOPG in states $v'' = 2$, $J'' = 0$-4 at the surface temperatures indicated are shown in Figure 5.16-5.19, along with the corresponding Boltzmann plots. Again, no signals for $J'' > 4$ were observed.

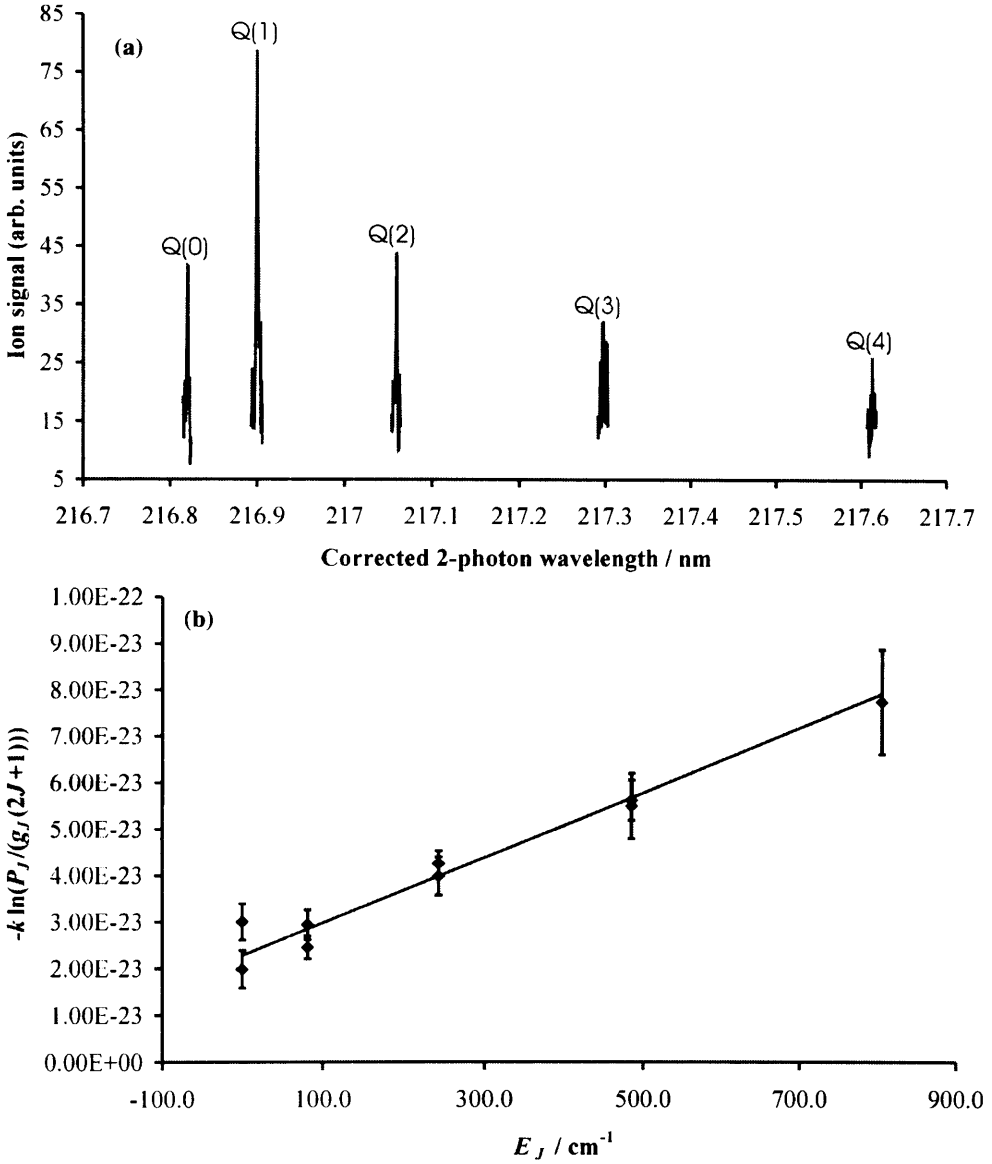

Figure 5.16. (a) shows the REMPI spectrum for the transitions $^1\Sigma_g^+$ X (v'' = 2, J'' = 0-4) → $^1\Sigma_g^+$ E,F (v' = 0, $J' = J''$) for HD formed on a HOPG surface held at 15 K. (b) shows the corresponding Boltzmann plot used to calculate the average rotational temperature of the molecules formed on the surface held at 15 K.

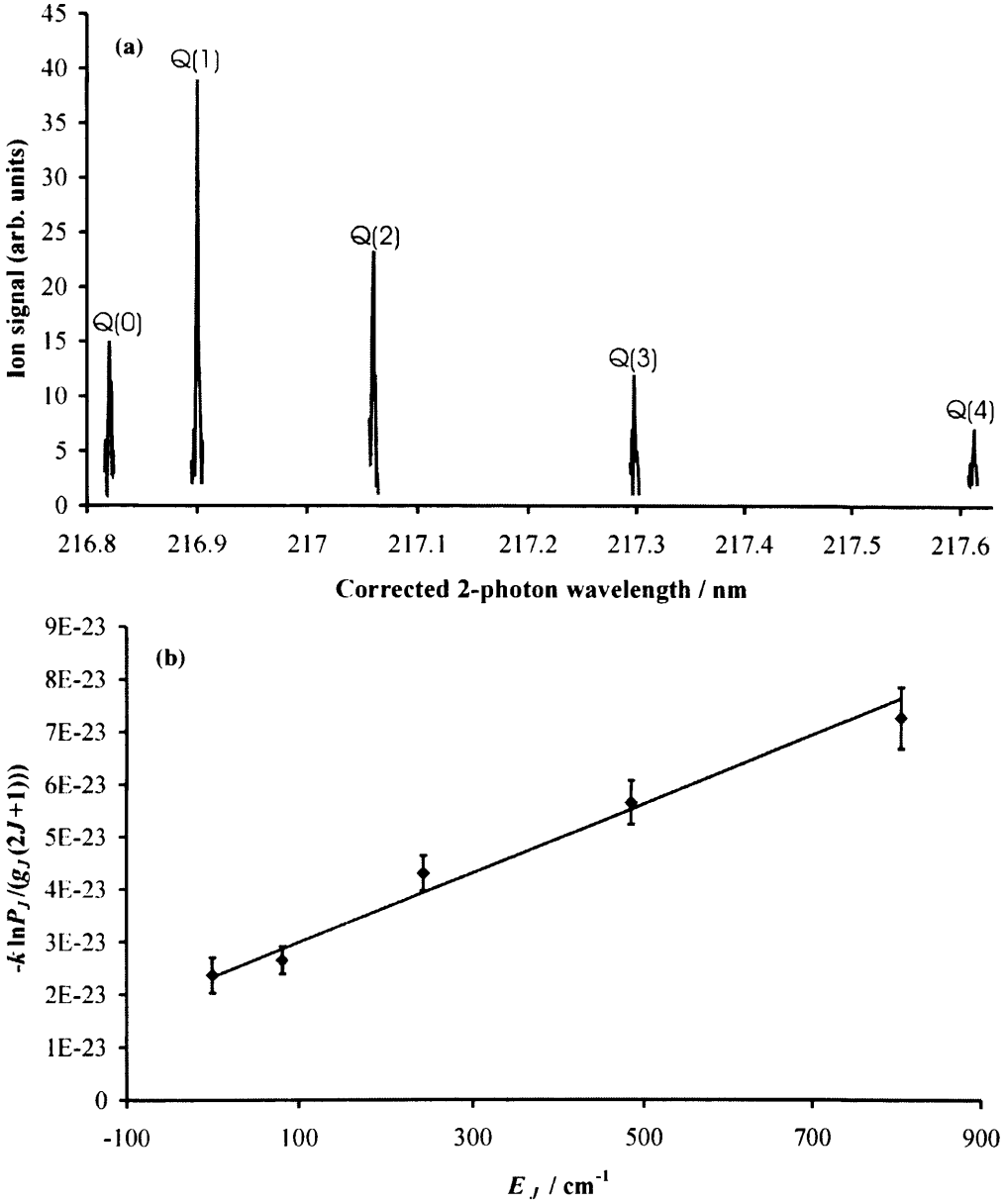

Figure 5.17. (a) shows the REMPI spectrum for the transitions $^1\Sigma_g^+$ X (v'' = 2, J'' = 0-4) → $^1\Sigma_g^+$ E,F (v' = 0, $J' = J''$) for HD formed on a HOPG surface held at 27K. (b) shows the corresponding Boltzmann plot used to calculate the average rotational temperature of the molecules formed on the surface held at 27K.

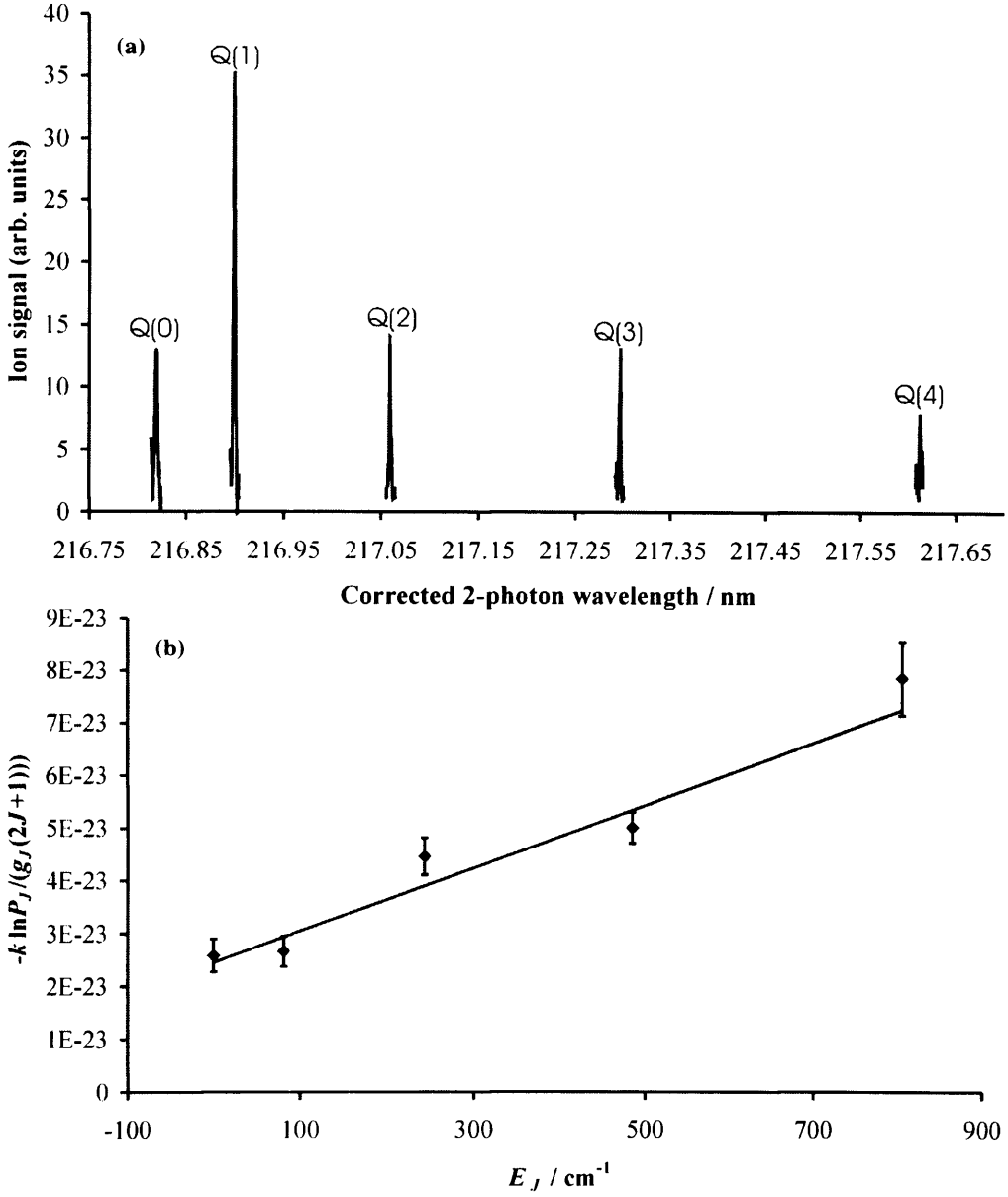

Figure 5.18. (a) shows the REMPI spectrum for the transitions $^1\Sigma_g^+$ X (v'' = 2, J'' = 0-4) → $^1\Sigma_g^+$ E,F (v' = 0, $J' = J''$) for HD formed on a HOPG surface held at 40 K. (b) shows the corresponding Boltzmann plot used to calculate the average rotational temperature of the molecules formed on the surface held at 40 K.

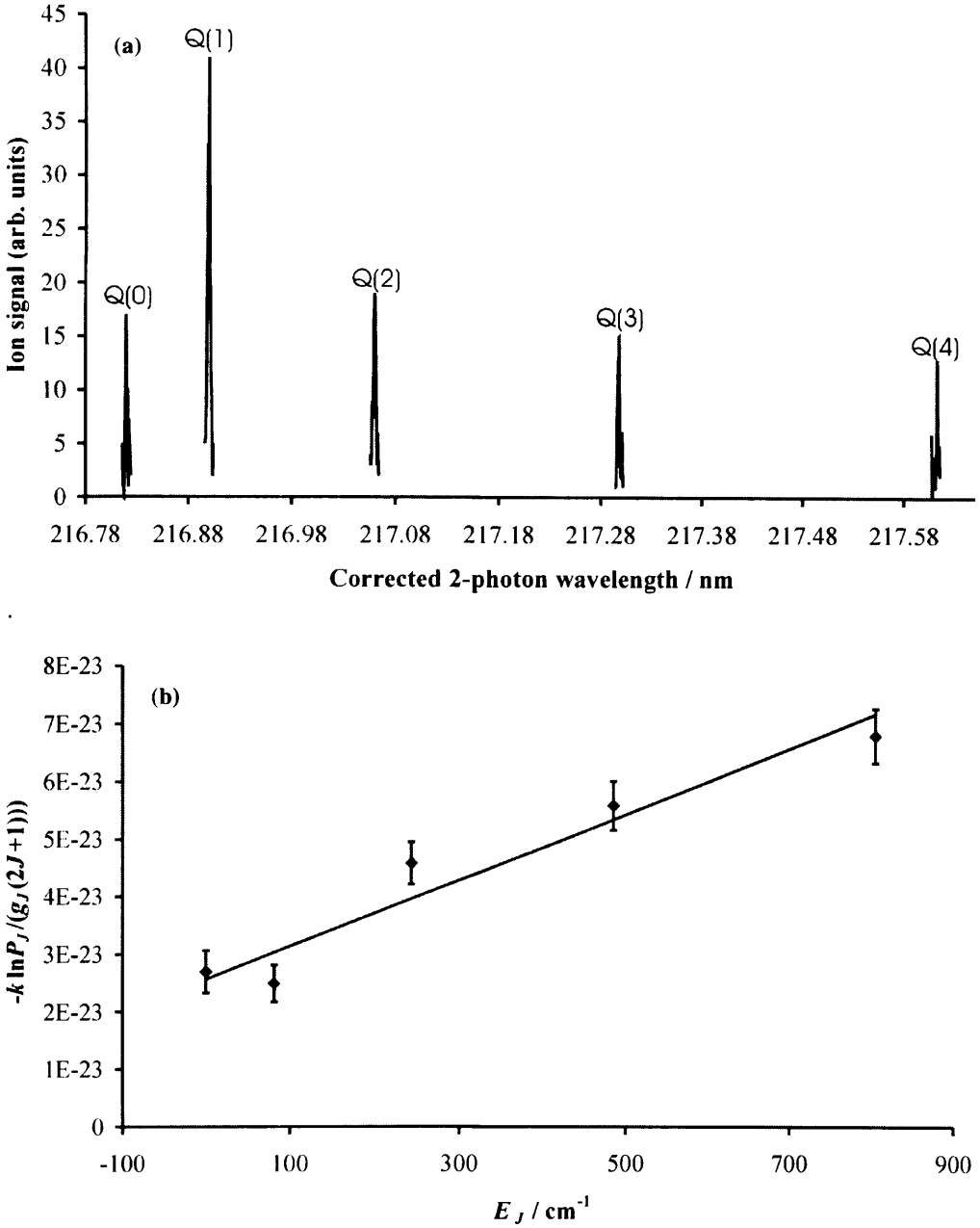

Figure 5.19. (a) shows the REMPI spectrum for the transitions $^1\Sigma_g^+ X$ ($v'' = 2$, $J'' = 0$-4) $\rightarrow$ $^1\Sigma_g^+ E,F$ ($v' = 0$, $J' = J''$) for HD formed on a HOPG surface held at 50 K. (b) shows the corresponding Boltzmann plot used to calculate the average rotational temperature of the molecules formed on the surface held at 50 K.

The rotational populations for HD formed in $v'' = 2$, normalised to $J'' = 0$, are given in Table 5.8 below.

Table 5.8. Relative rotational populations N_J for HD formed in $v'' = 2$ at various surface temperatures Tsurf.

J''	$N_J(T_{surf}=15$ K)	$N_J(T_{surf}=27$ K)	$N_J(T_{surf}=40$ K)	$N_J(T_{surf}=50$ K)
0	1.00 ± 0.29	1.00 ± 0.24	1.00 ± 0.23	1.00 ± 0.27
1	4.47 ± 0.80	2.43 ± 0.46	2.83 ± 0.59	3.48 ± 0.81
2	2.01 ± 0.40	1.22 ± 0.30	1.28 ± 0.33	1.27 ± 0.34
3	1.04 ± 0.33	0.64 ± 0.19	1.20 ± 0.26	0.86 ± 0.26
4	0.29 ± 0.23	0.25 ± 0.11	0.20 ± 0.10	0.47 ± 0.16

The rotational temperatures determined at each surface temperature are shown in Table 5.9 below.

Table 5.9. Rotational temperatures of HD formed in $v'' = 2$, $J'' = (0\text{-}4)$ at different surface temperatures

T_{surf} / K	Rotational Temperature / K
15	286 ± 37
27	299 ± 31
40	331 ± 37
50	345 ± 39

The average rotational temperatures for HD formed in $v'' = 2$ are much higher than the temperature of the surface they were formed on, and are also higher than the rotational temperatures determined for HD formed in $v'' = 1$. This result is also in good agreement with the results obtained for H_2 formation on HOPG at different surface temperatures.

The comparison between the rotational temperatures obtained for $v'' = 1$ and $v'' = 2$ are shown in Figure 5.20 below.

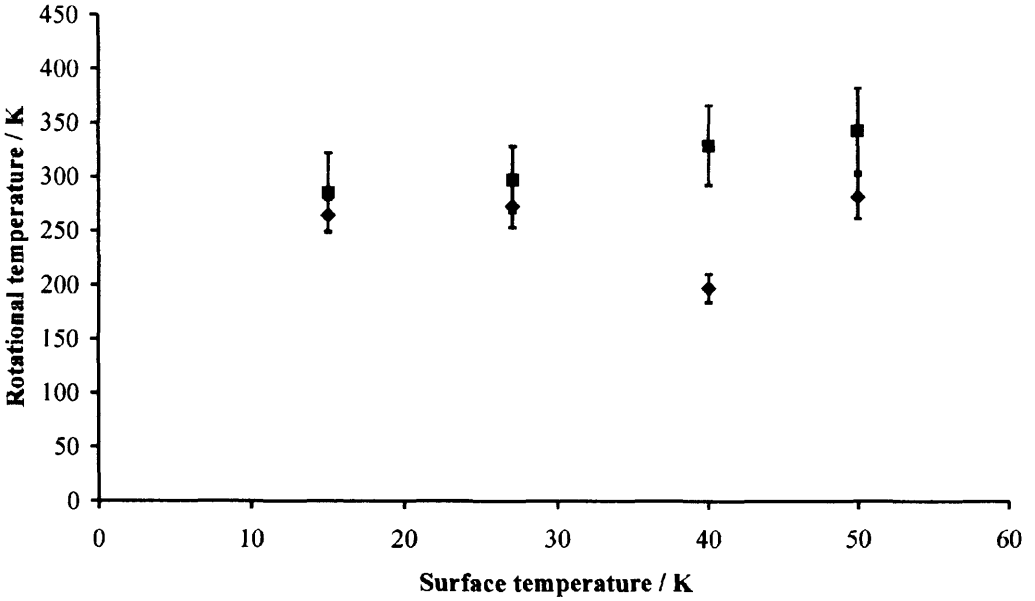

Figure 5.20. A plot of the average HD rotational temperature against surface temperature for the recombination of H with D atoms on HOPG. The ♦ symbol is for HD formed in v'' = 1 whilst ■ indicates HD formed in v'' = 2.

From the REMPI data it is possible to determine an approximate ratio of the densities of HD in v''=1 and v''=2. This ratio of v'' = 2:v'' = 1 is approximately 1.3 ± 0.2. This ratio is determined by comparing the intensities of the appropriately scaled REMPI signals recorded in different experimental runs. The signals are scaled by using the vibrational correction factors, C_v, determined in reference [1]. These correction factors were determined by sequentially measuring the ion signals of rotational levels in two adjacent vibrational bands, v_1 and v_2, under identical experimental conditions. When these rotational distributions were plotted on the same Boltzmann plot, they resulted in the vibrational bands being displaced from each other. The correction factors C_v were then determined by the relation between the intercepts, $I(v_1)$ and $I(v_2)$ such that $\frac{C_{v_1}}{C_{v_2}} = \exp\left[\frac{I(v_1)-I(v_2)}{k}\right]$. The ion signals must be divided by the correction factors in order to be able to compare the relative populations of the states. This scaling is necessary to account for the difference in the 2-photon transition probabilities for the vibrational levels and allow the relative

populations in each state to be compared correctly. The correction factors used are detailed in Table 5.10.

Table 5.10. Table detailing the correction factors, Cv, for the (2+1) REMPI detection of HD *via* the transition $^1\Sigma_g^+ X(v'', J'') \rightarrow {}^1\Sigma_g^+ E,F(v' = 0, J' = J'')$ [1].

v'' state	C_v
1	3.2 ± 0.2
2	4.1 ± 0.2

Every effort was made to keep all the experimental variables, such as the incident H and D atom fluxes, constant between these runs. However, the above ratio should be viewed as an approximate measurement of the relative product *densities*. This ratio expresses the relative densities of HD molecules in the two vibrational states, as the TOFMS measures the density of the target species, not the flux. These relative densities need to be scaled by the relative velocities of the molecules in $v'' = 1$ and $v'' = 2$ to give the ratio of the fluxes. The velocities of the product molecules are not measured directly in our experiments. However, as described below in section 5.9.1, from the width of the HD^+ signals in the TOF mass spectrum, it can be concluded that their translational energies are below 1 eV. Given this observation, the above ratio can be interpreted as showing that the fluxes of HD in $v'' = 1$ and $v'' = 2$ from the surface are approximately equal.

5.5. Search for HD formed in $v'' = 3$

With the laser system described in Chapter 3, it is not possible to search for H_2 or HD formed in vibrational levels higher than $v'' = 2$ *via* the $E,F^1\Sigma_g^+ (v' = 0, J' = J'')$ state, since the wavelengths required (~ 225 nm) are out of the range of the crystals used for the doubling and tripling of the dye laser beam. However, the wavelengths required to search for $v'' = 3$ *via* the $E,F^1\Sigma_g^+ (v' = 2, J' = J'')$ and $E,F^1\Sigma_g^+ (v' = 3, J' = J'')$ states of HD (~ 212 nm and ~215 nm respectively) are well within the range of the crystals described in Chapter 3. Considering the Franck-Condon factors for

each state [5], it was decided to try and search for HD formed in $v'' = 3$ *via* the $E,F^1\Sigma_g^+$ ($v' = 3$, $J' = J''$) state. This was decided because of the much better Franck-Condon factor for the $E,F^1\Sigma_g^+$ ($v' = 3, J' = J''$) - $X^1\Sigma_g^+$ ($v'' = 3$, J'') transition (0.182) compared with the Franck-Condon factor for the $E,F^1\Sigma_g^+$ ($v' = 2, J' = J''$) - $X^1\Sigma_g^+$ ($v'' = 3$, J'') transition (4.5×10^{-8}). The result of the REMPI scan is shown below in Figure 5.21.

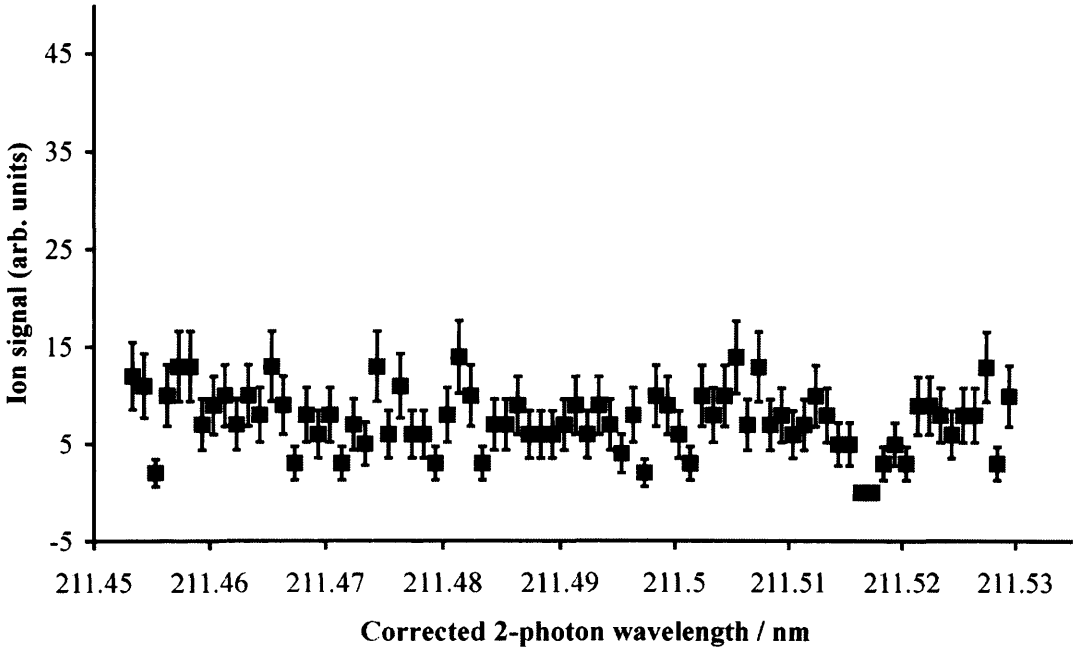

Figure 5.21. Plot showing attempts at finding a REMPI signal for HD formed in $v'' = 3$ via the transition $X^1\Sigma_g^+$ ($v'' = 3, J'' = 1$) - $E,F^1\Sigma_g^+$ ($v' = 3, J' = 1$). It is clear that there is no signal above the background.

It is clear from the spectra that no signal for HD formed in $v'' = 3$ was found by searching *via* the $E,F^1\Sigma_g^+$ ($v' = 3$, $J' = J''$) state, despite lengthy and numerous scans. This does not, however, give conclusive evidence that HD is not formed in $v'' = 3$ on HOPG. As will be described below, a new laser has recently been installed for the experiment which will allow HD formed in $v'' = 3$ and higher vibrational levels to be searched for *via* the $E,F^1\Sigma_g^+$ ($v' = 0$, $J' = J''$) state. The Franck-Condon factor for the relevant transition *via* the $E,F^1\Sigma_g^+$ ($v' = 0$, $J' = J''$) state is 0.176. All the Franck-Condon factors stated are taken from [5].

5.6. New Laser System

Following the completion of the data acquisition for $v = 1$ and $v = 2$, a new Sirah dye laser was installed in the laboratory, to replace the ND 6000 dye laser described in Chapter 3. This new laser is pumped by the same Nd:YAG laser described in Chapter 3. The new dye laser works in much the same way as the ND 6000 laser, in that a dye cell is pumped by the Nd:YAG laser and the dye laser beam is then amplified by pumping a capillary cell. The key difference comes at the stage where the dye beam is first frequency doubled and then the doubled beam mixed back with the dye beam to form UV photons in the wavelength range required. Instead of the automated tracking systems employed in the ND 6000 laser, the Sirah laser uses 'look up tables' to ensure optimum phase matching of the KDP and BBO crystals in which the 'doubling' and 'tripling' of the light occurs. These 'look up tables' are created by optimising the laser power of the doubled and tripled light at a certain wavelength, then moving the laser to another wavelength and repeating the optimisation. A line is then fitted to the data points, incorporating parameters to account for the angle cut and temperature of the crystal. These crystal positions are then stored in the PC which controls all the dye laser motor movements. This means that as the laser scans over a particular wavelength range, the crystals are automatically moved to the position where the phase-matching is maximised. This laser also gives much higher power than the ND 6000 model, around 2.5 - 3 mJ / pulse in the UV tripled light.

The new laser set-up has been installed principally to allow the search for highly excited vibrational levels in HD. For the purposes of this thesis, it has been commissioned and used to search for HD formed in $v'' = 0$ to give a representative result. Higher vibrational levels of HD will be looked for as a continuation of this research programme.

5.7. HD formed in $v'' = 0$

To attempt to determine if HD is formed on the graphite surface in $v'' = 0$ the ro-vibrational distribution for HD in $v'' = 0$ with the HOPG target at 15 K has been recorded. In these experiments, the H and D atom beams are incident upon the target. However, a potential problem with measurements of the rotational distributions of HD in $v'' = 0$ is the contribution of "thermalised" background HD molecules to the signals observed. To quantify the contribution of the background gas HD $v'' = 0$ signals have also been searched for under the following conditions: microwaves to the H-atom source on but to the D-atom source off, microwaves to the H-atom source off but to the D-atom source on and microwaves to both atom sources off. In all cases, the molecular gases were left flowing through the gas transport lines. As shown below, this measurement of the "background" HD signal in $v'' = 0$ is vital if in order to determine whether there are HD $v'' = 0$ REMPI signals from nascent HD molecules formed on the surface.

With the microwaves to both atom sources on, signals were observed for HD present in $v'' = 0$, $J'' = 0$-6. The rotational population recorded gives a good fit to a Boltzmann distribution at 299 K as described below. However, smaller, but appreciable, signals for HD formed in $v'' = 0$, $J'' = 0$-4 were still observed when the microwaves to either of the sources were turned off. Small REMPI signals from HD in $v'' = 0$, $J'' = 0$-4 were also observed when the microwaves to both of the sources were turned off, and just the molecular gases left flowing. The intensity of the REMPI signals decreased significantly when the microwaves to either or both of the sources were turned off, as shown in Table 5.11 below. Table 5.11 details the relative rotational populations and the areas of the REMPI peaks, corrected for laser power, for HD present in $v'' = 0$ for the situations described above.

Table 5.11. Table to show the relative rotational populations and REMPI peak areas for HD formed in $v'' = 0$ with the specified combinations of atom sources on and off. The HOPG target temperature was 15 K.

Atom Source Status	J	N_J(normalised J = 0)	REMPI peak area (corrected for laser power)
H-atom ON, D-atom ON	0	1.00 ± 0.08	982 ± 77
Rotational T: 299 ± 6 K	1	1.81 ± 0.14	1780 ± 133
	2	1.38 ± 0.10	1356 ± 101
	3	0.79 ± 0.06	778 ± 61
	4	0.10 ± 0.01	96 ± 10
	5	0.191 ± 0.003	19 ± 3
	6	0.002 ± 0.001	2.0 ± 0.7
H-atom OFF, D-atom ON	0	1.00 ± 0.10	274 ± 27
Rotational T: 290 ± 8 K	1	2.85 ± 0.23	783 ± 64
	2	0.99 ± 0.10	270 ± 28
	3	0.77 ± 0.09	212 ± 25
	4	0.16 ± 0.02	44 ± 6
	5	0.013 ± 0.003	3.5 ± 0.8
	6	0.001 ± 0.001	0.33 ± 0.37
H-atom ON, D-atom OFF	0	1.00 ± 0.10	235 ± 23
Rotational T: 283 ± 9 K	1	1.17 ± 0.10	275 ± 24
	2	0.95 ± 0.12	224 ± 27
	3	0.55 ± 0.05	130 ± 11
	4	0.04 ± 0.01	10 ± 2
	5	0.007 ± 0.004	2 ± 1
	6	-	-
H-atom OFF, D-atom OFF	0	1.00 ± 0.13	30 ± 4
Rotational T: 304 ± 15 K	1	2.37 ± 0.25	72 ± 7
	2	0.96 ± 0.14	29 ± 4
	3	0.66 ± 0.11	20 ± 3
	4	0.16 ± 0.04	5 ± 1
	5	0.001 ± 0.012	0.27 ± 0.36
	6	0.002 ± 0.006	0.06 ± 0.19

As described above, and shown in Table 5.11, with both sources on and the target at 15 K, the rotational temperature measured for HD in $v'' = 0$ was 299 ± 6 K. Through comparison with the predicted Boltzmann plot, it is clear that the measured rotational distribution is Boltzmann, within the error limits, as shown below in Figure 5.22.

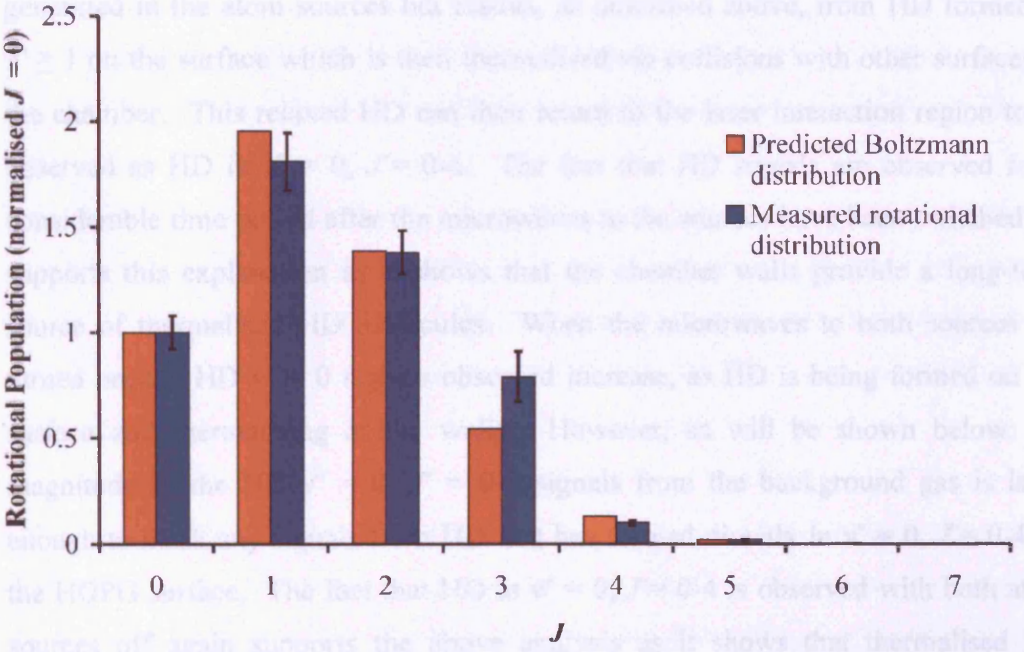

Figure 5.22. Plot of the predicted Boltzmann distribution for HD formed in $v'' = 0$ at 300 K compared to the measure rotational distribution for HD formed in $v'' = 0$ with the HOPG target at a temperature of 15 K.

The obvious question from this observation is are the observed signals due to nascent HD molecules formed in $v'' = 0$, $J'' = 0$-6, or are the signals dominated by HD molecules that have formed on the surface in higher vibrational states and have been "relaxed" into the ground vibrational state by collisions with the walls? Given the excellent agreement of the rotational temperature with the temperature of the chamber walls, and the large signals observed, it seems most likely that the signals are due to vibrationally relaxed HD.

The above deduction is confirmed by the fact that signals are still observed for HD formed in $v'' = 0$, $J' = 0$-4 when the microwaves to either one or both of the atom sources are turned off. This observation shows that HD molecules remain present in the target vacuum chamber for an appreciable time period. The marked reduction in the HD $v'' = 0$ signals (by approximately a factor of three) when either of the atom sources is turned off, strongly indicates that the observed HD in $v'' = 0$ is not generated in the atom sources but results, as described above, from HD formed in $v'' \geq 1$ on the surface which is then thermalised *via* collisions with other surfaces in the chamber. This relaxed HD can then return to the laser interaction region to be observed as HD in $v'' = 0$, $J'= 0$-6. The fact that HD signals are observed for a considerable time period after the microwaves to the sources have been switched off supports this explanation as it shows that the chamber walls provide a long-term source of thermalised HD molecules. When the microwaves to both sources are turned on, the HD $v'' = 0$ signals observed increase, as HD is being formed on the surface and thermalising at the walls. However, as will be shown below, the magnitude of the HD $v'' = 0$, $J' = 0$-4 signals from the background gas is large enough to mask any signals from HD that has formed directly in $v'' = 0$, $J'= 0$-4 on the HOPG surface. The fact that HD in $v'' = 0$, $J'= 0$-4 is observed with both atom sources off again supports the above analysis as it shows that thermalised HD molecules on the chamber walls can return slowly to the gas phase providing a long term source of HD molecules at 300 K.

Despite the above problems with the signals from background HD molecules, some conclusions can be drawn regarding the formation of HD in $v'' = 0$ on the HOPG surface. By considering the observed signal intensities for HD formed in $v'' = 1$ on the HOPG surface, it is possible to predict whether it would be possible to distinguish any HD that has formed in $v'' = 0$ on the HOPG surface from the background signal for HD in $v'' = 0$. The strongest signal in $v'' = 1$ occurs for the $J' = 1$ rotational line and a typical value for the area under the peak for this $v'' = 1$, $J' = 1$ line, corrected for laser power, is approximately 165 ± 11 counts in 200 seconds. The accumulation time per point for the rotational signals for HD in $v'' = 0$

was 20 seconds, hence it is necessary to divide the $v'' = 1$, $J'' = 1$ area by 10 to compare the signals. A value of 16.5 counts is then obtained for the signal that would "typically" be expected for HD formed directly from the heterogeneous reaction. As shown in Table 5.11, the signals from HD in $v'' = 0$, $J'' = 0$-4 with both sources on are much larger than 16.5 counts. This both supports the conclusion that these signals are dominated by background gas and shows that it would not possible to distinguish any signal from HD formed in $v'' = 0$, $J'' = 0$-4 on the HOPG surface from the background signal. That is, the addition of a signal of 16.5 counts to any of the rotational intensities in Figure 5.22 would not make a statistically significant difference to the Boltzmann analysis. However, for the higher J'' states, $J'' > 5$, the signals from the background gas are much smaller. Therefore, since a statistically significant non-Boltzmann intensity has not been observed for these higher rotational states ($J'' > 5$) it is possible to state confidently that the heterogeneous reaction does not produce HD molecules in $v'' = 0$, $J'' > 5$ with anything like a comparable intensity to which HD $v'' = 1$, $J'' = 1$ is formed.

REMPI signals for HD in $v'' = 0$, $J'' = 7,8$ have been searched for but no signal has been observed from these states. If any HD in $v'' = 0$, $J'' = 7,8$ were to be observed, it would be possible to assign these states to nascent HD molecules, given the above analysis. Hence, it would appear that the heterogeneous reaction to form HD, does not populate $v'' = 0$, $J'' = 7,8$ at a level above the detection limits.

To conclude, these investigations of the formation of HD in $v'' = 0$ are hampered by the signals from thermalised HD molecules which return to the gas phase by desorption from the chamber walls. However, despite these background signals it is possible to determine that the heterogeneous reaction of H and D atoms on HOPG does not form HD in $v'' = 0$, $J'' = 6$-8 with intensities comparable to those found in $v'' = 1, 2$.

5.8. Modelling the H_2 Coverage

Experiments were performed by Govers and co-workers in the 1980s, using bolometry, to determine the sticking probability of H-atoms on a cold surface (4 K) as a function of the H_2 coverage on the surface [6, 7]. From their data, the group were able to determine the rate of H-atom recombination, as a function of the coverage of H_2 molecules already on the surface [6, 7]. This group also found that, when reacting H atoms on a 4 K surface pre-dosed with D_2, desorption of D_2 was observed. These D_2 molecules were desorbed either because of localised heating of the surface *via* the recombination of the incident H atoms, or through a collision with a desorbing, newly formed, H_2 molecule. Either way, energy transfer to these secondary D_2 molecules will reduce the internal energy content of the nascent H_2. From the data of Govers *et al* [7]it is found that, on average, at least one D_2 molecule is desorbed per H-atom recombination event, although it is assumed that this number will be a function of the coverage. This observation raises the possibility that the signals seen in the experiments described in this thesis, from H_2(HD) in $v'' = 1,2$, arise from these "secondary" desorption events and are not the primary products of recombination; the primary products being formed in much higher vibrational levels. In order to address this possibility, a simple kinetic model to determine the steady-state H_2 coverage on our surface has been constructed, using the data from Govers *et al* [6, 7]. This model includes the rates of adsorption and desorption of H_2 and the probability of the reaction of H atoms on the surface, as a function of the coverage of H_2. As discussed above, the fact that every H_2 molecule formed by recombination may eject other H_2 molecules from the surface is also included in our model.

As a function of the H_2 coverage on the surface, Govers and co-workers determined the sticking probability of H_2 on the bolometer surface, the binding energy of H_2 to the surface, the sticking probability of H-atoms on the H_2 covered surface, the reaction probability of H-atoms recombining to form H_2 and the binding energy of

H-atoms on the H_2 covered surface. All of these parameters have been included in the kinetic model of the H_2 coverage on the surface, as described below.

Using the various parameters determined by Govers *et al*, it is possible to write down rate equations to find the coverage of H_2 on the surface, as shown below. These equations are then numerically integrated until a steady-state coverage of H_2 on the surface is obtained. The visual basic program, which performs this integration, is set to run for a certain time period, over a number of time steps, *dt*. During this time period, typically 60 seconds, it determines the coverage at each time step, until a steady-state is achieved. The initial conditions, from which the integration starts, can be changed depending on the user's requirements. For the results described below, the pressure in the chamber was set to 5×10^{-8} Torr, the initial coverage of H_2 on the surface was set to zero, the gas temperature was set to 300 K, the number of H_2 molecules desorbed per H-H recombination reaction was set to 1 and the time step, *dt*, was set to 5×10^{-6} s. The flux of H-atoms that exit the gas line into the target chamber has been determined, *via* previous experiments, to be approximately 20% of the total amount of hydrogen in the beam [8]. This flux of H-atoms is approximately 4×10^{12} cm^{-2} (see Chapter 4), hence, the flux of H_2 in the beam has been determined to be $\sim 2 \times 10^{13}$ cm^{-2}. This value for the flux of H_2 in the beam is used in the kinetic model.

In order to construct the kinetic model, the following rate equations have been used. The rate of change of the number, N_{H_2}, of H_2 molecules on the surface, if is is assumed that no H_2 formed by H-atom recombination sticks on the surface, is given by:

$$\frac{dN_{H_2}}{dt} = Rate H_{2\,ads} - Rate H_{2\,des} - Rate H_{2\,eject} \qquad 5.6$$

where $Rate H_{2ads}$ is the rate of adsorption and $Rate H_{2des}$ is the rate of desorption from the surface, $Rate H_{2eject}$ is the rate of desorption of H_2 molecules already on the

surface that are ejected from the surface due to the recombination of H-atoms to form H_2.

Then:

$$Rate\mathrm{H}_{2\,\mathrm{ads}} = \left(Z_{\mathrm{H}_2} + \mathrm{H}_{2_{flux}}\right) N_{H_2} S_{\mathrm{H}_2} \qquad 5.7$$

$$Rate\mathrm{H}_{2\,\mathrm{des}} = \frac{1}{\tau} N_{\mathrm{H}_2} \qquad 5.8$$

$$Rate\mathrm{H}_{2\,\mathrm{eject}} = N_{eject}\left(Rate\mathrm{H}_{\mathrm{recomb}}\right) \qquad 5.9$$

where Z_{H_2} is the collision frequency of H_2 gas from the chamber with the surface, $\mathrm{H}_{2_{flux}}$ is the flux of H_2 in the source gas line, S_{H_2} is the sticking probability for H_2, τ is the residence time of the molecule on the surface, N_{eject} is the number of H_2 molecules ejected due to H-atom recombination, $Rate\mathrm{H}_{\mathrm{recomb}}$ is the rate of recombination of H-atoms to form H_2.

The collision frequency, Z_{H_2}, of H_2 from the background gas in the chamber with the surface is determined from the following equation:

$$Z_{\mathrm{H}_2} = \frac{p}{(2\pi mkT)^{\frac{1}{2}}} \qquad 5.10$$

where p is the ambient pressure, in N cm^{-2}, m is the molecular mass, in kg $molecule^{-1}$, T is the temperature of the gas, in Kelvin and k is the Boltzmann constant, in J K^{-1}. This equation gives the value of Z_{H_2} in units of cm^{-1} s^{-1}.

The residence time, τ, of the molecule (or atom) on the surface is given by [7]:

$$\tau = \tau_0 \exp\left(\frac{\varepsilon}{kT_s}\right) \qquad 5.11$$

where T_s is the surface temperature and ε is the binding energy of the molecule (ε_{H_2}) (or atom, ε_H) to the surface. The value used for τ_0 is 10^{-13} s, a value typically found in the literature.

For the H-atoms, the following parameters are defined:

$$Rate\mathrm{H}_{ads} = S_{\mathrm{H}}\mathrm{H}_{flux} \qquad 5.12$$

$$Rate\mathrm{H}_{des} = \frac{1}{\tau}N_{\mathrm{H}} \qquad 5.13$$

$$Rate\mathrm{H}_{recomb} = Rate\mathrm{H}_{ads}\beta \qquad 5.14$$

where $Rate\mathrm{H}_{ads}$ is the rate of adsorption of H-atoms on the surface, $Rate\mathrm{H}_{des}$ is the rate of desorption from the surface, $Rate\mathrm{H}_{recomb}$ is the rate of recombination of H-atoms to form H_2, S_H is the sticking probability of H-atoms as a function of H_2 coverage, H_{flux} is the flux of H-atoms into the chamber from the source gas line and β is the probability of a thermalised atom recombining with another atom before desorbing.

It is assumed that there is no contribution to the flux of H-atoms to the surface from any background H-atoms in the chamber. It is further assumed that the rate of H-atom desorption from the surface reaches a steady-state almost immediately and therefore, it is not necessary to include equation 5.13 in the integration in the kinetic model.

The above rate equations assume that the Langmuir-Hinshelwood mechanism is the route by which H-atoms recombine to form H_2. Govers *et al* have shown that this pathway is favourable even at surface temperatures as low as 3 K [6, 7].

The parameters S, β and ε_{H_2}, ε_H, defined above and measured by Govers *et al*, are all functions of the H_2 coverage on the surface. Functional forms are therefore required for these parameters in order to include them in the kinetic model, since it is

necessary to know the values for these parameters at each stage of the calculation as the coverage evolves towards its steady-state value. Gaussian and exponential functions have been fitted to these parameters from the data given by Govers *et al* in references [6, 7]. For H_2, S_{H_2} and ε_{H_2} have been fitted as a function of the coverage of H_2 on the surface. For the H-atoms, S_H, β and ε_H have been fitted as a function of H_2 coverage on the surface. The best fits were determined by the least squares method. Figure 5.23 and Figure 5.24 below are taken from reference [7] and show the data used for the fits obtained.

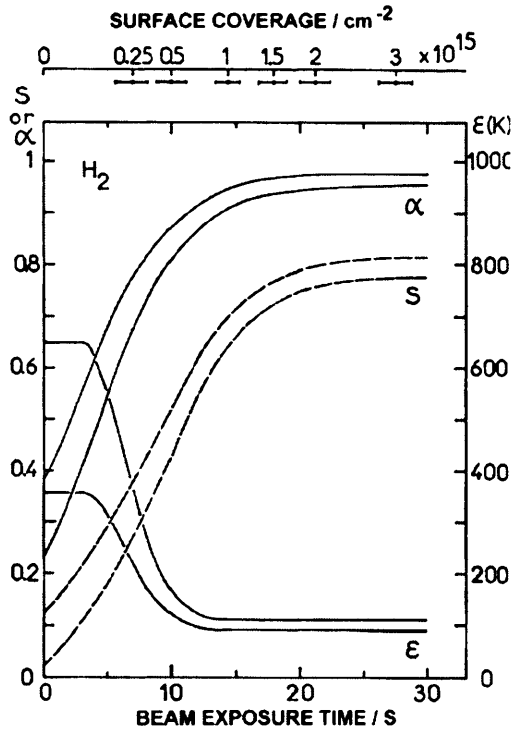

Figure 5.23. Taken from reference [7]. This plot shows the sticking coefficient, S, and the binding energy, ε, for H_2 as a function of surface coverage of H_2.

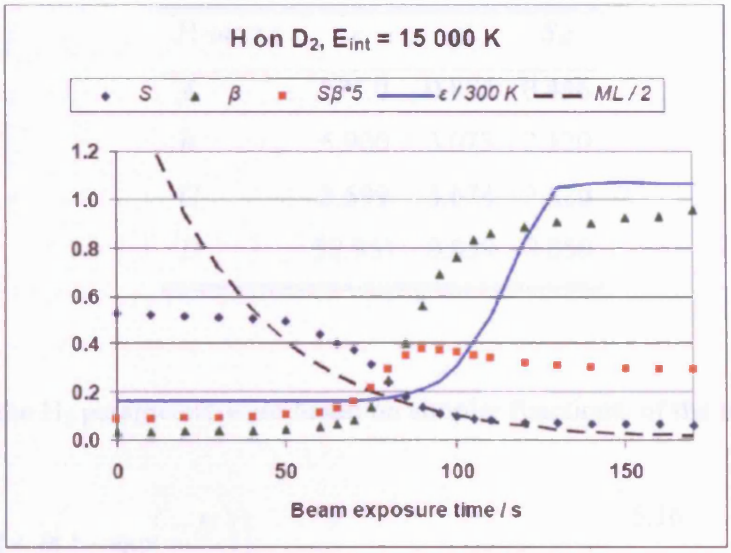

Figure 5.24. Taken from reference [7]. This plot shows the parameters for the H-atoms as a function of beam exposure time. These have been converted to a function of the surface coverage of $H_2(D_2)$ for use in the kinetic model.

The form of the Gaussians used for fitting the H-atom functions is given by:

$$A\exp\left(\left(\frac{-N}{10^{15}}\right)B\right)^{C}+D \qquad 5.15$$

where C is a power greater than 2, N is the number of atoms or molecules involved in the parameter, A,B and D are constants to give the correct shape of the curve.

Table 5.12 below gives the values of A, B, C and D used to fit each parameter.

Table 5.12. Table detailing the values used to fit the parameters to determine the rate equations for the H-atoms.

H-atoms	ε	β	S_H
A	275.0	0.888	0.456
B	5.900	3.073	2.170
C	3.599	3.674	2.820
D	52.951	0.039	0.059

The fits to the H_2 parameters were based on simpler functions, of the form:

$$A + B\left(1 - \exp\left(\frac{-N}{C}\right)\right) \qquad 5.16$$

for the sticking probability S_{H_2}, and of the form:

$$A + B\exp\left(\frac{N}{C}\right) \qquad 5.17$$

for the binding energy ε.

Table 5.13 below details the values of A, B and C used in these fits.

Table 5.13. Table detailing the values used to fit the parameters to determine the rate equations for the H-atoms.

H_2 molecules	ε	S_H
A	93.730	0.107
B	411.904	0.693
C	3.06×10^{14}	6.42×10^{14}

When the kinetic model is set to run, using the initial conditions described above, it indicates that at a surface temperature of 15 K the steady state coverage of H_2 is approximately one hundredth of a monolayer. The steady-state is reached after

approximately 30 seconds exposure. At this surface temperature, and given the incident atom fluxes, this limiting H_2 coverage is almost independent of the number of spectator H_2 molecules that are assumed to be desorbed per recombination event. The model also indicates that this steady state coverage is a strong function of the surface temperature, since the coverage rises to 6% of a monolayer at 10 K. This temperature dependence is clearly shown in Figure 5.25 and Table 5.14 below. Increasing the surface temperature above 15 K quickly leads to almost zero coverage of H_2 on the surface, as shown below in Table 5.14.

Table 5.14. Table to show the temperature dependence of the H_2 surface coverage.

T_{surf} / K	Steady State H_2 coverage / ML
10	6.148×10^{-2}
15	1.106×10^{-2}
20	1.596×10^{-10}

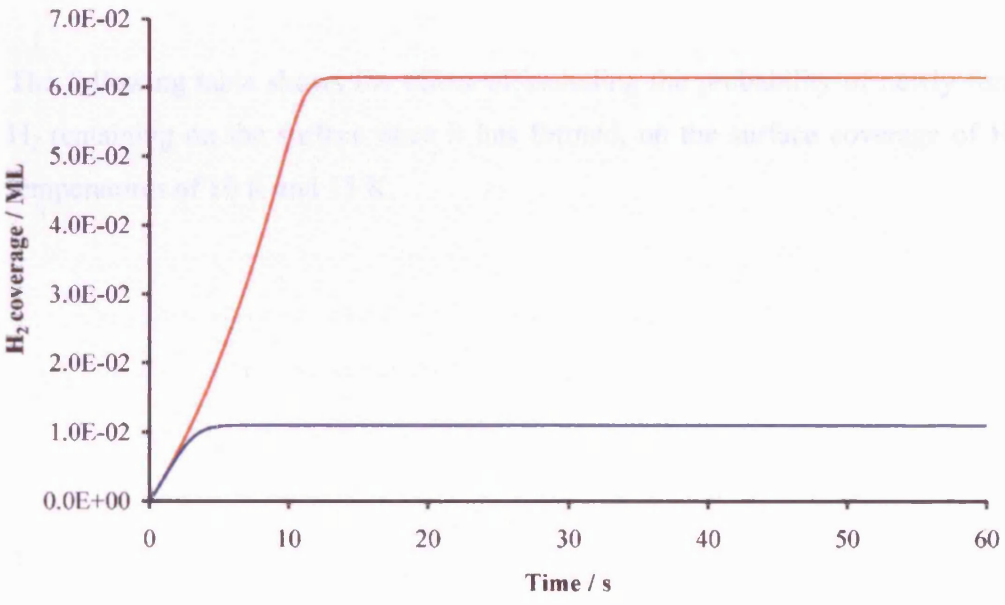

Figure 5.25. Plot to show the effect of surface temperature on H_2 coverage in the modeling of the results of Govers *et al* [6, 7]. The red line indicates H_2 coverage at a surface temperature of 10 K while the blue line indicates H_2 coverage at a surface temperature of 15 K.

In the model used to obtain the results detailed above, for the coverage of H_2 achieved at surface temperatures of 10, 15 and 20 K, the probability of the newly formed H_2 molecule remaining on the surface is zero, and it is assumed that any H_2 that forms on the surface is immediately desorbed. To include the effect on the surface coverage of H_2 of the nascent H_2 molecules sticking to the surface, the kinetic model has been adapted with the rate of nascent H_2 residing on the surface modelled by the following equation:

$$Rate\mathrm{H}_{2\mathrm{residing}} = \gamma_{\mathrm{H}_2} Rate\mathrm{H}_{\mathrm{recomb}} \qquad 5.18$$

where γ_{H_2} is the probability of the newly formed H_2 molecule remaining on the surface once it has formed.

The rate of change of H_2 coverage on the surface then becomes:

$$\frac{dN_{\mathrm{H}_2}}{dt} = Rate\mathrm{H}_{2\mathrm{ads}} + Rate\mathrm{H}_{2\mathrm{residing}} - Rate\mathrm{H}_{2\mathrm{des}} - Rate\mathrm{H}_{2\mathrm{eject}} \qquad 5.19$$

The following table shows the effect of including the probability of newly formed H_2 remaining on the surface once it has formed, on the surface coverage of H_2 at temperatures of 10 K and 15 K.

Table 5.15. Table detailing the steady state coverage of H_2 on the surface when the probability of the molecule remaining on the surface once it has formed is included in the kinetic model.

Surface T / K	γ_{H_2}	$N_{H_2\ eject}$	Steady State Coverage of H_2 / monolayer
10	0	0	6.153×10^{-2}
		1	6.147×10^{-2}
	0.5	0	6.155×10^{-2}
		1	6.150×10^{-2}
	1	0	6.158×10^{-2}
		1	6.153×10^{-2}
15	0	0	1.111×10^{-2}
		1	1.106×10^{-2}
	0.5	0	1.114×10^{-2}
		1	1.109×10^{-2}
	1	0	1.117×10^{-2}
		1	1.111×10^{-2}

It is clear from the above data that including the probability of a newly formed H_2 molecule remaining on the surface once it has formed, has very little effect on the steady-state coverage of H_2. Hence, the key conclusion from this model is that the steady-state coverage of H_2 under these experimental conditions is low, and that it is dominated by background H_2 gas in the chamber, not by H_2 formed from the reaction of H-atoms on the surface. Under these low coverage conditions, it therefore seems highly unlikely that the vibrationally excited H_2 molecules observed are the secondary species desorbed as a result of H atom recombination events and it is therefore clear that our observations of H_2 and HD in $v'' = (1,2)$, J' are due to the formation of H_2 and HD on the surface.

5.9. Energy Partitioning

As has been described in detail in the previous Chapters, the aim of the experiments detailed in this thesis is to determine the ro-vibrational energy distribution of molecular hydrogen formed on analogues of interstellar dust. In order to use the

data described in this Chapter to determine the partitioning of the 4.5 eV of binding energy released on the formation of H_2(HD) on HOPG, it is necessary to make a determination of the translational energy of the nascent molecules. Section 5.9.1 below details the information it is possible to ascertain concerning the translational energy of the nascent H_2 and HD molecules from the experiment, giving an upper limit for their translational energy. Section 5.9.2 discusses the partitioning of the remaining binding energy into the internal energy states of H_2 and HD and into the surface, once this upper limit to the translational energy has been considered.

5.9.1. Translational Energy

It is not possible to directly measure the translational energy of the detected ions using our experimental set-up. However, in principle, the temporal widths of the H_2^+ and HD^+ signals in the TOF mass spectrum can provide some information on the translational energy of these ions along the axis of the TOFMS. In fact, it is possible to use information gained from the temporal widths of the peaks in the TOF mass spectrum, to determine an upper limit for the translational energy of the nascent molecules perpendicular to the surface normal, that is, in the direction of the MCP detector.

The temporal widths of the peaks in a TOF mass spectrum depend on a number of factors. The width of a peak resulting from ions with zero initial kinetic energy, the instrument function, arises from various experimental parameters including jitter in the timing electronics and non-uniformity of the electric fields. If the initial kinetic energy of the ions sampled is non-zero, the distribution of velocities resulting from this non-zero translational energy will, in principle, contribute to the width of the peak in the TOF mass spectrum. The effect of the initial velocities of the ions on the temporal widths of the TOF peaks can be shown if one considers two ions with the same initial kinetic energy, formed at the same point, but travelling in opposite directions; ion 1 in the direction of the detector and ion 2 in the opposite direction. Ion 2 will be decelerated by the source field, E_s, until it stops and will then be

accelerated again in the direction of the detector, returning to the point of ionisation with its initial speed. Ion 2's motion is then identical to that of ion 1 but it will lag behind ion 1 by the 'turn around time', which is twice the deceleration time (see Figure 5.26).

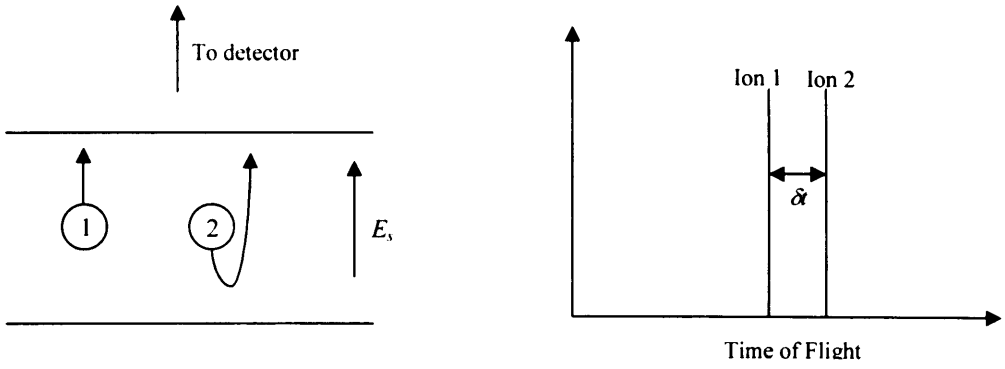

Figure 5.26. Schematic diagram to show the paths of two ions with opposite initial velocities, and their position in the TOFMS.

This turn around time corresponds to the time spread, δt, of the ions hitting the detector [9]:

$$\delta t = \frac{2(2mU_0)^{\frac{1}{2}}}{qE_s} \qquad 5.20$$

where U_0 is the initial kinetic energy of the ions, m is the mass of the ion, q is the charge on the ion and E_s is the electric field in the source region of the TOFMS.

The 'thermal' flight time of an ion, t_0, that is, the flight time of an ion with zero initial kinetic energy is then given by [10]:

$$t_0 = t_{expt} + \frac{(2mU_0)^{\frac{1}{2}}}{qE_s} \qquad 5.21$$

where t_{expt} is the measured time-of-flight of the ion with initial kinetic energy U_0 in the direction of the detector.

Since $U_0 = \frac{1}{2}mv_0^2$, equation 5.21 can then be rearranged to give:

$$v_z = -\left[t_{expt} - t_0\right]\frac{qE_s}{m} \qquad 5.22$$

where v_z is the velocity of the ion in the z direction (that is, in the direction of the detector in the TOFMS).

If the peak widths of the HD^+ ions were dominated by the kinetic energy of the ions, we could use the velocity calculated using equation 5.22 to determine this kinetic energy, *via* the standard equation $E = \frac{1}{2}mv^2$. As detailed below, it is certain that the width of the HD^+ peaks is dominated by the kinetic energy of the ions, indicating that they have a low velocity. However, by assuming that the entire temporal width of the HD^+ peak in the mass spectrum is due to the ion's kinetic energy, it is possible to obtain an upper limit for the translational energy of the nascent molecules, from the velocity of the ions determined with equation 5.22.

For example, an average peak width for HD^+ in the mass spectrum is 40 ns. This value corresponds to ions travelling both towards and away from the detector and so it is necessary to divide this by 2 to give the correct value for $\left|t_{expt} - t_0\right|$, 20 ns. The charge, q, on the ion is 1.602×10^{-19} C, the source field, E_s, is $\frac{400}{0.03} = 1.33 \times 10^4$ V m^{-2}, and the mass of HD is 4.98×10^{-27} kg. The value for E_s is determined from the voltage applied to the middle plate of the TOFMS (400 V) divided by the distance between the middle plate and the repeller plate, 0.03 m. Substituting these values into equation 5.22 gives a value for the velocity, v_z, of 8.57×10^3 ms^{-1}. A value of the kinetic energy of ~1.1 eV is then obtained, if the whole of the peak width of the HD^+ signal was due to the ion's kinetic energy, which of course it is not. Therefore, if the vibrationally excited H_2^+ and HD^+ ions were to have a translational energy component along the axis of the TOFMS in excess of 1 eV, they would be expected to produce an observable change in the widths and/or

positions of the TOF REMPI peaks but this has so far not been the case. Hence, if it is assumed that the nascent HD and H_2 molecules desorb over the full range of angles relative to the surface normal, it is then possible to put an approximate upper limit on their translational energy of 1 eV.

As described above, when performing this calculation it is assumed that the entire width of the HD^+ peaks in the TOF mass spectrum is due to the energy spread of the ions. However, again as mentioned above, the instrument function also contributes to the width of the peak in the mass spectrum. Similar peak widths from H_2^+ ions in the mass spectrum to those seen for the HD^+ ions have been observed. These H_2^+ ions arise from the background gas in the chamber that has been ionised by the REMPI process. These background ions are thermal ions with an average kinetic energy of 0.025 eV, and their peak widths will be dominated by the instrument function. Hence, the fact that these thermal ions have similar peak widths to the HD^+ ions suggests that the kinetic energy of the HD^+ ions is likely to be much less than the 1 eV upper limit that has been determined here. Further evidence to suggest that the translational energy of the nascent molecules may be less than 1 eV is found in a previous study by Roser *et al* [11]. This group found that the kinetic energy of hydrogen molecules desorbing from an amorphous water ice surface was very low, in the region of 3 meV [11]. Hence, it would appear that the upper limit determined in this section for the kinetic energy of the desorbing nascent molecules is a considerable overestimate, but the most robust upper limit it is possible to determine, using the current TOFMS.

As discussed later in Chapter 6, a future adaptation of the experimental set-up will allow the translational energy of the nascent desorbing molecules to be measured much more accurately.

5.9.2. Internal Energy and Energy into the surface

Having determined an upper limit to the translational energy of ~1 eV, there remains a minimum value of ~3.5 eV to distribute between the rotational and vibrational degrees of freedom of the molecules, and the HOPG surface. Using the standard spectroscopic equations for rotational and vibrational energies, it is possible to determine how much energy has gone into vibrational and rotational modes as a function of v'' and J'. These equations are shown below:

$$E_v = \omega_e\left(v+\frac{1}{2}\right) - \omega_e x_e\left(v+\frac{1}{2}\right)^2 \text{ cm}^{-1} \qquad 5.23$$

$$E_J = \left(\left(B_e - \alpha\left(v+\frac{1}{2}\right)\right)J(J+1)\right) - DJ^2(J+1)^2 \text{ cm}^{-1} \qquad 5.24$$

where:

E_v is the energy of the vibrational state, vibrational quantum number v

E_J is the energy of the rotational state, rotational quantum number J

ω_e is the angular frequency

x_e is an anharmonicity constant

B_e is the equilibrium value of the rotational constant B

α is a molecular constant

D is the centrifugal distortion coefficient

From the experimental data, it has been determined that the nascent molecules are formed in v'' = 1, J' = 0-4 and v'' = 2, J' = 0-4. It is also assumed that there is a contribution to the energy for H_2 formed in v'' = 0, J' = 0-5 and HD formed in v'' = 0, J' = 0-6. Table 5.16 and Table 5.17 below detail how this remaining energy is then split between these various modes for both H_2 and HD.

Table 5.16. Table detailing how the 4.5 eV of binding energy released on the formation of H_2 is distributed through the various possible internal energy modes, and into the surface. As detailed in the text, the value for the translational energy is an upper limit and hence, the value for the energy deposited into the surface is a lower limit.

H_2 State		Energy Distribution %			
v	J	Translation	vibration	rotation	surface
0	5	20	6	5	69
1	3	20	17	2	51
2	3	20	28	2	61

Table 5.17. Table detailing how the 4.5 eV of binding energy released on the formation of HD is distributed through the various possible internal energy modes, and into the surface. As detailed in the text, the value for the translational energy is an upper limit and hence, the value for the energy deposited into the surface is a lower limit.

HD State		Energy Distribution %			
v	J	Translation	vibration	rotation	surface
0	6	22	5	5	68
1	4	22	15	2	60
2	4	22	25	2	51

It is clear from the tables above that a maximum value of around 40% of the available energy goes into internal excitation and translational energy of the nascent molecules, with the rest deposited into the surface. These values are based on the current experimental results and are correct for the v'' and J' states that are observed to be populated. Since the value for the kinetic energy is an upper limit, and therefore possibly much lower than 1 eV, the values given for the energy deposited into the surface are therefore lower limits. If the translational energy is much lower than 1 eV, more energy may then be deposited into the surface than has been suggested here. It is also possible that higher v'' and J' states of the molecules, as well as those observed here may be populated. If it is the case that higher internal energy states are also populated, this would result in less energy being deposited into the surface when these states are formed, compared with the states observed here.

Obviously, a search for higher v'' and J' states of the molecules is required, which will be possible with the new laser system, as described in Chapter 6. All the results described in this Chapter will be discussed in detail in section 5.10.

5.10. Discussion

5.10.1. Origin of the REMPI signals

As we are trying to quantify the internal energy of newly formed molecules on the HOPG surface, it is of vital importance to be able to show, without doubt, that the ions detected in the TOFMS are due to the REMPI of molecules formed on the surface and not from anywhere else in the vacuum chamber. A number of tests have been carried out to ensure that this is the case.

5.10.1.1. Origin of the H_2 REMPI signals

In Chapters 2 and 4, the commissioning tests to ensure that the H_2 molecules were formed on the surface and not elsewhere in the chamber have been described. These tests were carried out on the experimental set-up when just the H-atom source was in place. These tests showed that no vibrationally excited H_2 was entering the chamber from the H-atom source, and that no ro-vibrationally excited H_2 could be detected when the PTFE transport tube for the H-atom beam was pointed out of the line of sight of the laser interaction region, clearly indicating that the molecules had formed on the HOPG surface. As discussed in Chapter 2, investigating the formation of H_2 in the $v = 0$ vibrational level was not possible with just the single H-atom source, since it would be indistinguishable from the background gas. Hence, no diagnostic experiments were performed to establish the origin of the H_2 $v'' = 0$ signal, unlike the experiments on HD described in section 5.7.

The rotational temperatures determined for the nascent H_2 molecules (see section 5.3), at first glance, appear very close to room temperature, and could perhaps imply

that the H_2 molecules had rotationally cooled or thermalised before being detected. It has been shown that this is not the case by repeating the experiments at half the pressure in the atom cell, and hence the target chamber, and finding no difference in the observed rotational temperatures [3]. This result indicates that rotational cooling does not affect the experimental results and again shows that the ions detected are due to the newly formed molecules from the surface.

5.10.1.2. Origin of the HD REMPI signals

Upon the introduction of the D-atom source, it was necessary to ensure that the HD molecules observed were due to HD that had formed on the HOPG surface and not elsewhere in the chamber. REMPI signals from HD ($v'' = 1$, $J'' = 1$) were searched for with the microwaves to the H-atom source on and the microwaves to the D-atom source off, and *vice versa*. In these experiments it was just the microwaves to the relevant source which were turned off; both molecular gases were still flowing through the system. Throughout these experiments, when the microwaves to either of the sources were turned off, the HD^+ signal decreased by at least 95 %, indicating that the signals detected with both sources on were indeed from HD formed on the target surface and not from cross-contamination between the sources. This result also supports the conclusion that the REMPI signals are from recombination on the surface. If recombination on the various metal surfaces in the chamber was the source of the vibrationally excited HD it might be expected that, when piping just D-atoms into the chamber, HD signals from the reservoir of H_2, and perhaps chemisorbed H-atoms on the metal surfaces of the target chamber, would be seen but no such signals are observed. The influence of turning off the microwaves to either source is clearly shown in Figure 5.27 below.

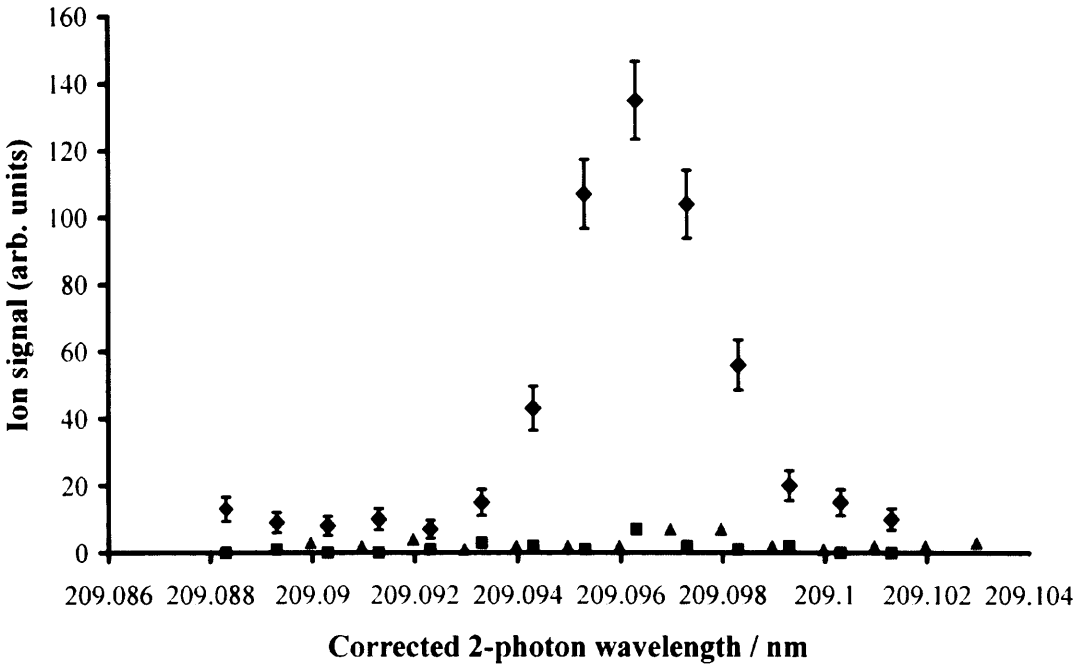

Figure 5.27. REMPI signal for the HD transition $E,F\,^1\Sigma_g^+$ ($v' = 0, J' = 1$) - $X\,^1\Sigma_g^+$ ($v'' = 1, J' = 1$). The ♦ symbol indicates the signal when both atom sources on, ■ shows the signal when the H atom source is on but the D atom source is off and ▲ indicates signal when D atom source is on but H atom source is off. The data was recorded for the recombination of H and D atoms from a HOPG surface at 298 K.

In principle, the use of two isotopic atom beams should allow the investigation of the $v'' = 0$ level of HD and so experiments were carried out to determine whether the signal for HD observed in the $v'' = 0$ vibrational level was due to HD formed in $v'' = 0$ on the HOPG surface or elsewhere in the chamber. These experiments have been described in detail in section 5.7. The observation of HD formed in $v'' = 0$, $J' = 0$-4 when the microwave supply to either or both of the atom sources is turned off suggests that either that some of the HD generated in the target chamber accumulates on the experimental surfaces, and the residual desorption of these thermalised HD molecules gives us a background signal from HD $v'' = 0$. This observation also shows that any ro-vibrationally excited HD which has formed on the HOPG surface, may thermalise with the chamber walls and eventually return to the laser interaction region.

5.10.2. The Energy Budget

5.10.2.1. Comparison of Results with other Experiments

The detection of ro-vibrationally excited H_2 and HD molecules from the cold HOPG surface indicates that some of the binding energy released upon the formation of the H-H(D) bond is converted into internal excitation of the molecule. For both H_2 and HD, the population of the rotational levels in each vibrational state detected, at each surface temperature, fit a Boltzmann distribution reasonably well. As has been discussed in the literature [12], there is no definitive reason for the rotational states populated in dissociative recombination reactions of H(D) atoms to follow a Boltzmann distribution. However, it is often, but not always [13], observed that such rotational distributions are approximately Boltzmann, sometimes with a rotational temperature that is higher than the temperature of the surface [12, 14-16]. For example, an investigation into the interaction of atomic hydrogen with metal surfaces by Winkler found that D atom recombination on Ni(110) at 180 K results in approximately Boltzmann rotational distributions, with a rotational temperature that decreases with vibrational quantum number [12]. The rotational temperatures determined in this study were also much higher than the surface temperature of 180 K. Similarly, Boltzmann rotational distributions are observed for the formation of D_2 on Ag(111) [14]. This study, by Murphy and Hodgson, again looked at the recombinative desorption of D_2 using (2+1) REMPI, and they found that the rotational temperatures of the molecules were much higher than the surface temperature: 550 K from a surface at 210 K. In contrast, the study by Schröter *et al* [15] into the recombinative desorption of H_2 from Pd(100), found that although the rotational populations did follow a Boltzmann distribution, the average rotational temperature of the molecules was much lower than that of the surface: 281 K from a surface at 570 K.

The rotational temperatures observed here for HD formed on a HOPG surface in both $v'' = 1$ and $v'' = 2$ are very similar to those observed for H_2 at all the surface temperatures investigated. This indicates that the formation of HD on the HOPG

surface is a good model for H_2 formation. As discussed below, these results do not show any clear evidence of the isotope effects predicted for these processes in some theoretical studies [17]. However, as previously discussed, the restriction in the laser photons available when this data was taken meant that it is only possible to observe the formation of H_2 and HD in v''=1 and v''=2. Because of this restriction, these measurements give no information on the occupation of higher vibrational levels which may be better candidates for detecting differences in relative vibrational populations, as a monitor of isotopic differences in the formation of H_2 and HD. In fact, reference [17] indicates that vibrational levels v = 5 and v = 6 would be more useful as a probe of the isotopic differences. This problem will be overcome by the use of the new laser system briefly described in section 5.6 which will enable much higher vibrational levels to be investigated.

As discussed in section 5.9.1, the temporal widths of the H_2^+ and HD^+ signals from the TOFMS can provide some information on the translational energy of these ions along the axis of the TOFMS, perpendicular to the surface normal. No shifting, or additional broadening in the vibrationally excited HD^+ and H_2^+ signals compared with thermal HD^+ and H_2^+ signals has been observed. As discussed above, it is estimated that, if the HD^+ and H_2^+ ions were to have a translational energy component along the axis of the TOFMS in excess of 1 eV, they would produce an observable change in the widths and/or positions of our mass spectral peaks. Hence, if it is assumed that the nascent HD and H_2 molecules desorb over the full range of angles relative to the surface normal, it is possible to put an approximate upper limit on their translational energy of 1eV. This upper limit is in agreement with the recent measurements of Roser *et al.* who have monitored the translational temperature of D_2 desorbed in TPD experiments from an amorphous ice surface previously dosed with D atoms [11]. These experiments show that the D_2 molecules are desorbed with a low translational energy. Combining the upper limit on the translational energy determined here (1 eV) with the (v'', J'') levels observed to be populated, suggests that an upper limit of approximately 40% of the binding energy released

upon the formation of H_2 (and HD) goes into internal or translational excitation of the molecules detected in $v'' = 1$ and $v'' = 2$.

This conclusion of significant energy deposition into the surface is in qualitative agreement with the results of the thermal desorption experiments, from an amorphous carbon surface, of Katz *et al* [18]. Katz *et al.* concluded from modelling their TPD experiments that a significant proportion (about 40%) of the HD molecules formed remain on the surface for a significant time period before desorbing, implying significant energy flow into the surface.

Comparing our results with the experiments of Hornekaer *et al.* [19], who studied HD formation on amorphous water films, shows that the results obtained here clearly agree with their conclusion that surface morphology affects the energy distribution in the nascent HD. Hornekaer *et al.* [19] concluded that HD that had formed on porous amorphous solid water (ASW) films had fully thermalised with the surface before desorbing and that HD formed on non-porous ASW films promptly desorbed from the surface. Molecules desorbing promptly from the surface are expected to show some internal excitation, as they have not fully thermalised with the surface. Our observation of vibrationally and rotationally excited H_2 and HD molecules from a non-porous HOPG surface is in accord with these results, indicating that the HD has not fully thermalised with the surface.

From the data of Govers and co-workers [6, 7], it has been shown with the kinetic model (see section 5.8) that the steady state coverage of H_2 under our experimental conditions is low. Under these low coverage conditions it seems very unlikely that the vibrationally excited H_2 molecules observed here are the "secondary" species desorbed as a result of H atom recombination events. Furthermore, the results of Govers *et al* show a contrast to the results of Pironello *et al* [20-23]. Govers and co-workers have shown that there is significant mobility of H-atoms on a surface even at temperatures as low as 3-4 K, which suggests that recombination of H-atoms to form H_2 can occur even at this low temperature. The TPD experiments of

Pirronello and co-workers are said to be 'efficient' at 8 K and yet they do not observe any prompt formation of HD. Pirronello and co-workers have also suggested that the recombination of H-atoms to form H_2 is thermally activated.

Due to the ~0.2 eV barrier to chemisorption predicted by theory [24, 25] and established by experiments [26], as discussed in Chapter 1, it would not be expected that the incident 300 K atoms used in these experiments are chemisorbed on the HOPG surface. Therefore, the obvious conclusion is that we are observing the recombination of physisorbed atoms. Since it is not possible to characterise our surface with any of the usual surface science techniques, due to the difficulties associated with graphite surfaces and the limitations of the experimental apparatus, it is of course possible that defect sites on our surface allow easier access to chemisorbed states. However, the recent experiments of Zecho *et al.*, on etched carbon surfaces irradiated with 2000 K atoms, indicate that there is little change in the observed TPD spectra with the density of steps present on the carbon surface [27]. Zecho *et al* concluded from this work that, for atoms incident with a temperature of 2000 K, recombination on HOPG was dominated by reaction at the conventional sites on the (0001) terraces. However, the experiments described in this thesis, using 300 K atom beams and a 15 K surface, are in a different energy regime to the experiments of Zecho *et al*, and so it is possible that defects may influence the reactivity more dramatically at low temperatures.

It is clear from the above discussion that the results from these experiments fit in well with the data already available in the literature on H_2(HD) formation under conditions similar to those of the ISM. We have observed energy transfer to the surface, in agreement with the results of reference [18] and also significant internal excitation of the molecules, in agreement with the results of the experiments conducted by Hornekaer *et al* [19]. The following section will compare our experimental results with the theoretical studies performed on H_2 formation on interstellar grain analogue surfaces.

5.10.2.2. Comparison Results with Theory Calculations

As described in Chapter 1, the majority of theoretical investigations into the formation of molecular hydrogen in the ISM have probed the Eley-Rideal mechanism for the recombination of H atoms on graphite. These studies all predict the formation of vibrationally excited H_2 which has now been observed here experimentally.

Most of these theoretical investigations predict the maximum product flux for vibrational states with $v'' > 2$. As emphasized above these states have not yet been searched for, although the new laser system will allow us to search for these higher vibrational levels. However, the approximately equal abundance of H_2 in $v'' = 1$ and $v'' = 2$ observed experimentally is in reasonable agreement with the predictions of several [25, 28-34], but not all [35-37], of the theoretical studies of the ER reaction mechanism on carbon surfaces, all of which have been reviewed in Chapter 1. The study by Rutigliano *et al* [25] found a ratio of ~1:1 for the $v'' = 1$ and $v'' = 2$ states, at a variety of kinetic energies of the impinging H-atom. Farebrother *et al* [28] predict that most of the internal energy of the product molecules is in $v'' = 2$, with a ratio of approximately 2:1 $v'' = 2$: $v'' = 1$; however this study does not include any rotational excitation. A further study by Meijer *et al* [30], which looked at the effect of other H-atoms on the surface on the internal energy of the product molecules, again found that the $v'' = 2$ level was more populated than the $v'' = 1$ level, in agreement with our results, although again the ratio was approximately 2:1. Parneix and Bréchignac [31] found that the $v'' = 1$ state of H_2 was slightly more populated than the $v'' = 2$ state, with a ratio of approximately 1.2:1. Ree and co-workers [32] found that the ratio $v'' = 2$: $v'' = 1$ was approximately 1.2:1, with most of the vibrational energy peaking in $v'' = 3$. In contrast, the investigations by Morisset and co-workers [35-37], have predicted almost zero population in the $v'' = 0$-2 states. It is also found that the relatively low rotational excitation observed here experimentally is in accord with the general trends observed in several of these theoretical investigations [25, 29, 34].

As discussed above, the potential energy surface for the approach of an H atom to a graphite surface indicates, if the chemistry at defects is not important, that at the atomic translational energy in this experiment, it would be expected that our atoms react *via* a physisorbed precursor state. Only recently have computational groups started to turn their attention to the LH mechanism one might expect to dominate under these conditions [38, 39]. Again, these theoretical investigations predict considerable vibrational excitation in the product H_2 molecules but predict little formation of H_2 in v''=1 and v''=2, although as has been emphasized before the formation of H_2(HD) in higher lying vibrational states has not yet been searched for experimentally.

Calculations by Meijer *et al* [17] have suggested that, under the ER mechanism, there should be observable differences in the internal state populations of H_2, D_2 and HD formed on a graphite surface. Isotope effects in the formation of HD arise depending on which atom (H or D) is initially chemisorbed, and cannot be investigated here. In addition, at certain incident H(D) atom energies the calculations indicate there may be an observable difference in the formation efficiency of the v''=1 and v''=2 vibrational states between H_2 and HD. However, with an incident beam of D or H atoms at 300 K, the calculated reaction cross sections indicate that the v''=1 and v''=2 ratio is not a sensitive probe of these isotope effects and they would not expected to be observed here. As discussed above, the higher vibrational levels v'' = 5 and v'' = 6 may be better probes of any isotope effects in the formation of molecular hydrogen.

5.10.3. Astrophysical Implications

As was discussed in Chapter 1, the aim of these experiments is to determine the ro-vibrational distribution of H_2 and HD formed on interstellar grain analogues under conditions similar to those of the ISM. The experimental results in this Chapter have clearly shown that molecular hydrogen forms ro-vibrationally excited on a cold HOPG surface. HOPG is of course a very simple model for an interstellar

grain surface but it allows a direct comparison of our results with theoretical calculations, as has been discussed in the previous sections, and is a good first approximation. As yet, the results obtained in these experiments have not been included in any astrophysical models of the ISM. However, as described below, two models have used the results from theoretical calculations of the recombination of H-atoms on graphite, to determine the effect that ro-vibrationally excited H_2 may have on the chemistry occurring in the ISM.

The results of some of the theoretical calculations carried out on H_2 formation [28, 29] have been used in a model of the chemistry and excitation of H_2 in the ISM [40]. Previous discussions of the observed rotationally excited H_2 in the ISM had not included formation on grains as a source of excited H_2 but had instead just concentrated on collisional and radiative pumping methods, due to the lack of reliable information about the energy budget of the formation process. This model assumes that all the H_2 that forms on dust grains in the ISM is made *via* the ER reaction mechanism (see Chapter 1).

The following section refers to the model used in reference [40]. The modellers in this study predicted that the inclusion of 'formation pumping' would be noticeable in the IR emission spectrum of H_2. For the diffuse ISM, the modellers found that UV pumping dominated the emission, in particular the lines v = 1-0 and v = 2-1, with decreasing flux for the higher vibrational levels. The effect of formation pumping was clearly seen by comparison of the spectrum where formation pumping was included with the spectrum where it was not included in the model. In the spectrum where formation pumping was included, there was a signature emission line outside the wavelength range 2-3.5 μm. In the dense ISM model, it was found that formation pumping in fact dominated the emission spectra, as opposed to UV pumping. The study predicted a rich line spectrum due to formation pumping at wavelengths less than 2 μm and greater than 3.5 μm.

The modellers then made a search for the predicted lines in two objects, L1498 and L1512. These starless, pre-protostellar cores are well shielded from ambient interstellar UV radiation and have no internal sources of UV radiation, hence they should be representative of the physical conditions which the model assumes to give rise to the emission spectrum due to formation pumping. No observations of the H_2 lines of interest were made in these objects. The modellers accounted for this in a number of ways, including the fact that their model was based on the formation of H_2 on graphite, under the ER mechanism, which is thought to be less likely than the LH mechanism. Other suggested reasons as to why there was no observation of the H_2 lines of interest included the fact that the model did not allow the H-H system to take up energy from the graphite surface, which may reduce the expected high internal excitation. The workers concluded that more information from theoretical and experimental studies on H_2 formation was required.

The chemical effects of H_2 formation excitation in the ISM have also been investigated by modelling in another study [41]. This study assumes that all H_2 formed on interstellar grains has enough excitation to overcome the energy barriers in the formation reactions that form OH and CH^+, important ISM radicals.

$$H_2^* + O \rightarrow OH + H$$
$$H_2^* + C^+ \rightarrow CH^+ + H$$

The above reactions may initiate a rich chemistry in the ISM and, since a correlation has been observed between the column density of CH^+ and H_2 in highly rotationally excited states, these reactions are particularly pertinent to the inclusion of H_2^*. The modellers concluded from this study that excited hydrogen formed on dust grains has little effect on the chemistry occurring in the ISM. They found that the inclusion of ro-vibrationally excited H_2 in models of the chemistry only resulted in marginally enhanced abundances of the radicals in question. However, in the case of a diffuse region that was subject to a dissociative isothermal shock (an extreme case),

significant enhancements of OH and CH^+ were found, although these were found to be short lived enhancements.

The above studies highlight the need for more complete experimental data on the internal energy and translational energy of molecular hydrogen that has formed on the surfaces of interstellar grains. It has been shown from our results so far that over half the energy released on formation of molecular hydrogen is deposited into the grain surface, with a maximum value of 40% being distributed between the internal modes of the molecule and its translational energy. It should again be emphasised that this does not take into account any energy that may go into vibrational modes higher than $v'' = 2$ since these energy levels have not been investigated here. Until these higher v'', J'' states have been investigated, it is not easy to say how the binding energy released on the formation of H_2 may affect the chemistry occurring in interstellar clouds, and there is still a large amount of work to be done to answer the questions posed in Chapter 1.

5.11. Summary

The formation of H_2 and HD on a HOPG surface at surface temperatures between 15 K and 50 K has been studied and the results have been presented. H_2 has been detected desorbing from the target in ro-vibrationally excited states $v'' = 1$, $J'' = 0$-3 and $v'' = 2$, $J'' = 0$-3 and HD has been detected desorbing from the target in ro-vibrationally excited states $v'' = 0$, $J'' = 0$-6, $v'' = 1$, $J'' = 0$-4 and $v'' = 2$, $J'' = 0$-4. The average rotational temperatures of the desorbing molecules have been determined from the rotational populations and were found to be significantly higher than the temperature of the surface on which the molecule was formed. These observations indicate that molecular hydrogen can form in ro-vibrationally excited states on graphite under conditions similar to those of the ISM.

5.12. References

1. Rinnen, K.D., Buntine, M.A., Kliner, D.A.V., Zare, R.N., and Huo, W.M., *J. Chem. Phys.*, 1991. **95**(1): p. 214-225.

2. Pozgainer, G., Windholz, L., and Winkler, A., *Meas. Sci. Technol.*, 1994. **5**(8): p. 947-953.

3. Perry, J.S.A. and Price, S.D., *Astrophys. Space Sci.*, 2003. **285**(3-4): p. 769-776.

4. Creighan, S.C., Perry, J.S.A., and Price, S.D., *J. Chem. Phys*, 2005. **in press**.

5. Fantz, U. and Wunderlich, D., *Franck-Condon Factors, Transition Probabilities and Radiative Lifetimes for Hydrogen Molecules and their Isotopomers*. 2004, IAEA: Vienna. p. 1-319.

6. Govers, T.R., Mattera, L., and Scoles, G., *J. Chem. Phys.*, 1980. **72**(10): p. 5446-5455.

7. Govers, T.R., Mattera, L., and Scoles, G., J. *presented at the Astrosurf Meeting, University College London, April 18-19, 2005, and to be published (see: http://www.chem.ucl.ac.uk/astrosurf/challenges/programme.html and http://hal.ccsd.cnrs.fr/ccsd-00004273/en/).*

8. Perry, J.S.A., Gingell, J.M., Newson, K.A., To, J., Watanabe, N., and Price, S.D., *Meas. Sci. Technol.*, 2002. **13**: p. 1414-1424.

9. Wiley, W.C. and McLaren, I.H., *Rev Sci Instr*, 1955. **26**(12): p. 1150-1157.

10. Hu, W.P., Harper, S.M., and Price, S.D., *Meas. Sci. Technol.*, 2002. **13**(10): p. 1512-1522.

11. Roser, J.E., Swords, S., Vidali, G., Manico, G., and Pirronello, V., *Astrophys. J.*, 2003. **596**(1): p. L55-L58.

12. Winkler, A., *Appl. Phys. A-Mater. Sci. Process.*, 1998. **67**(6): p. 637-644.

13. Kubiak, G.D., Sitz, G.O., and Zare, R.N., *J. Chem. Phys.*, 1985. **83**(5): p. 2538-2551.

14. Murphy, M.J. and Hodgson, A., *Surf. Sci.*, 1996. **368**: p. 55-60.
15. Schroter, L., David, R., and Zacharias, H., *J. Vac. Sci. Technol. A-Vac. Surf. Films*, 1991. **9**(3): p. 1712-1718.

16. Zacharias, H., *Appl. Phys. A-Mater. Sci. Process.*, 1988. **47**(1): p. 37-54.

17. Meijer, A., Farebrother, A.J., and Clary, D.C., *J. Phys. Chem. A*, 2002. **106**(39): p. 8996-9008.

18. Katz, N., Furman, I., Biham, O., Pirronello, V., and Vidali, G., *Astrophys. J.*, 1999. **522**(1): p. 305-312.

19. Hornekaer, L., Baurichter, A., Petrunin, V.V., Field, D., and Luntz, A.C., *Science*, 2003. **302**(5652): p. 1943-1946.

20. Pirronello, V., Biham, O., Liu, C., Shen, L.O., and Vidali, G., *Astrophys. J.*, 1997. **483**(2): p. L131-L134.

21. Pirronello, V., Liu, C., Shen, L.Y., and Vidali, G., *Astrophys. J.*, 1997. **475**(1): p. L69-L72.

22. Pirronello, V., Liu, C., Roser, J.E., and Vidali, G., *Astron. Astrophys.*, 1999. **344**(2): p. 681-686.

23. Pirronello, V., Biham, O., Manico, G., Roser, J.E., and Vidali, G. *Laboratory studies of Molecular Hydrogen formation on Surfaces of Astrophysical Interest*. in *H2 in Space*. 1999: p. 71-83.

24. Jeloaica, L. and Sidis, V., *Chem. Phys. Lett.*, 1999. **300**(1-2): p. 157-162.

25. Rutigliano, M., Cacciatore, M., and Billing, G.D., *Chem. Phys. Lett.*, 2001. **340**(1-2): p. 13-20

26. Zecho, T., Guttler, A., Sha, X.W., Jackson, B., and Kuppers, J., *J. Chem. Phys.*, 2002. **117**(18): p. 8486-8492.

27. Zecho, T., Guttler, A., and Kuppers, J., *Carbon*, 2004. **42**(3): p. 609-617.

28. Farebrother, A.J., Meijer, A.J.H.M., Clary, D.C., and Fisher, A.J., *Chem. Phys. Lett.*, 2000. **319**(3-4): p. 303-308.

29. Meijer, A.J.H.M., Farebrother, A.J., Clary, D.C., and Fisher, A.J., *J. Phys. Chem. A*, 2001. **105**(11): p. 2173-2182.

30. Meijer, A., Fisher, A.J., and Clary, D.C., *J. Phys. Chem. A*, 2003. **107**(50): p. 10862-10871.

31. Parneix, P. and Brechignac, P., *Astron. Astrophys.*, 1998. **334**(1): p. 363-375.

32. Ree, J., Kim, Y.H., and Shin, H.K., *Chem. Phys. Lett.*, 2002. **353**(5-6): p. 368-378.

33. Sha, X.W., Jackson, B., and Lemoine, D., *J. Chem. Phys.*, 2002. **116**(16): p. 7158-7169.

34. Kim, Y.H., Ree, J., and Shin, H.K., *Chem. Phys. Lett.*, 1999. **314**(1-2): p. 1-8.

35. Morisset, S., Aguillon, F., Sizun, M., and Sidis, V., *Chem. Phys. Lett.*, 2003. **378**(5-6): p. 615-621.

36. Morisset, S., Aguillon, F., Sizun, M., and Sidis, V., *Phys. Chem. Chem. Phys.*, 2003. **5**(3): p. 506-513.

37. Morisset, S., Aguillon, F., Sizun, M., and Sidis, V., *J. Phys. Chem. A*, 2004. **108**(41): p. 8571-8579.

38. Morisset, S., Aguillon, F., Sizun, M., and Sidis, V., *J. Chem. Phys.*, 2004. **121**(13): p. 6493-6501.

39. Morisset, S., Aguillon, F., Sizun, M., and Sidis, V., *J. Chem. Phys.*, 2005. **122**(19): p. art. no.-194702.

40. Tine, S., Williams, D.A., Clary, D.C., Farebrother, A.J., Fisher, A.J., Meijer, A., Rawlings, J.M.C., and Davis, C.J., *Astrophys. Space Sci.*, 2003. **288**(3): p. 377-389.

41. Garrod, R.T., Rawlings, J.M.C., and Williams, D.A., *Astrophys. Space Sci.*, 2003. **286**(3-4): p. 487-499.

Chapter 6. Further Work

The previous chapters in this thesis have described the UCL Cosmic Dust Experiment, including apparatus development and new results that show that molecular hydrogen is formed ro-vibrationally excited on a cold graphite surface. It is clear, however, that there is much scope for further experiments and this Chapter will outline the next stages for the experiment.

6.1. New laser system to detect HD formed in $v'' > 2$

The new Sirah dye laser has been described briefly in Chapter 5. In order to search for higher vibrational levels of molecular hydrogen, UV photons of wavelengths 225 – 260 nm and higher are required. In order to generate these photons, the Nd:YAG pumping of the dye laser will be modified. Instead of using the 532 nm second harmonic light from the Nd:YAG, this light will in future be tripled, in the same way as described in Chapter 3, to give 355 nm third harmonic light. This 355 nm beam will then be used to pump the Sirah dye laser system. The light from the dye laser will then be doubled to give photons in the wavelength range required to search for HD formed in vibrational states $v'' > 2$.

The dyes required for this process will be Coumarin dyes, rather than the Rhodamine and DCM dyes used for the experiments described in this thesis. These Coumarin dyes cover a very large wavelength range, from 440 nm up to 560 nm, although not all with the same dye, and the Coumarin dyes will therefore give the required wavelengths of light for the experiments in question. This method of producing the photons should result in much higher laser power density, which will also make it very much easier to detect the states of interest, particularly if the signal intensities are very small, which may be the case at the surface temperatures at which the experiments are performed.

6.2. Position Sensitive Detector

In order to fully investigate the distribution of the energy released on the formation of molecular hydrogen, a more quantitative determination of the translational energy component than the method used in this thesis would be desirable. This can be achieved by the use of a position sensitive MCP detector. Position sensitive detectors have been used in experiments to probe the dynamics of both unimolecular and bimolecular reactions of molecular dications and the success of this method is well documented in the literature [1-5].

Position sensitive detectors allow both the x and y position of the ion hitting the detector to be established. Since the ionisation region is very well defined as a focused laser spot, the position within the detector that the molecule is ionised in our experimental set-up is known (see Figure 6.1). Hence, it is possible to determine how far in the x, y direction the ion has travelled when it hits the detector. This can then be related to the translational energy of the ion.

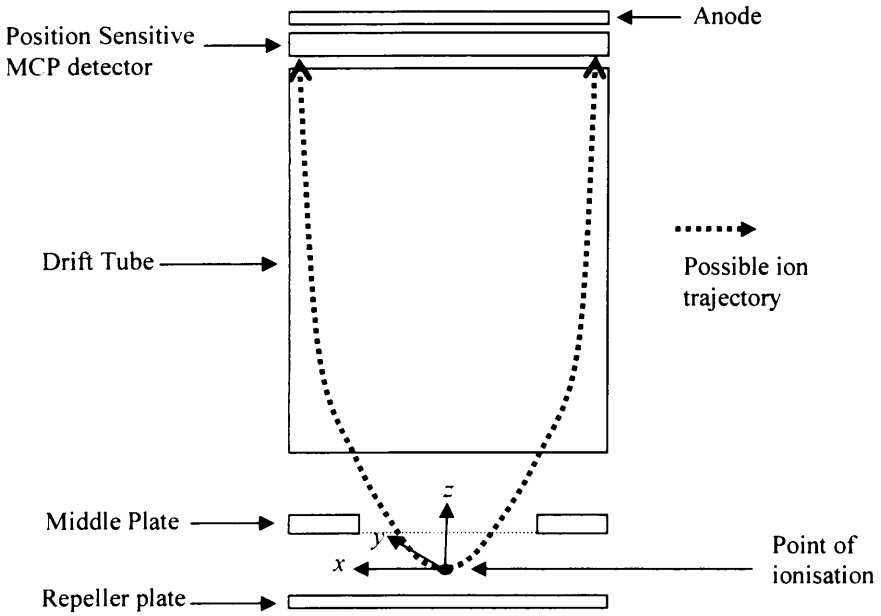

Figure 6.1. Schematic diagram to show the possible trajectory of ions in the TOFMS and how the position sensitive detector will allow determination of the velocities in the x and y directions, and hence the translational energy of the ions.

6.3. Cooled atomic beam source

It is well documented in the literature [6-9] that the temperature of the atomic hydrogen gas in diffuse interstellar clouds is around 100 K. Therefore, to fully attempt to re-create the conditions in interstellar space in the laboratory, it would be desirable to have cooled (100 K) beams of H and D atoms impinging on the cosmic dust analogue target. This can be achieved by the re-introduction of a cold aluminium block, through which the atoms could be piped just before they hit the target surface. Previously, the cooled aluminium block has been used as a diagnostic for the atom source, as described both in Chapter 2 of this thesis and in the literature [10, 11]. The reasons for removing the block from the current experimental set-up have also been described in Chapter 4 of this thesis. In order to cool the atom beams to 100 K just before they hit the target surface, the experimental apparatus would have to be modified so that the coldhead used for cooling the Al block could be positioned close enough to the laser interaction region and cosmic dust analogue target so that the Al block would be the last part of the atom beam transport system before the target.

6.4. Other Interstellar Grain Analogue Surfaces

As was shown in Chapter 1, the composition of interstellar dust is not accurately known. Hence, it would be of use to astronomers to investigate the formation of molecular hydrogen on other suitable dust analogue surfaces. For example, silicates are thought to be present in interstellar dust grains and so experiments on a suitable silicate surface, such as Olivine, would enable us to compare our results with those for HOPG. Olivine is a mixture of Mg_2SiO_4 and Fe_2SiO_4 and the use of this material would also allow further comparison of our results with other experiments where Olivine has been used to study molecular hydrogen formation [12, 13]. It would also be informative to use more amorphous carbon surfaces since it is unlikely that interstellar dust grains are as ordered as the HOPG surface used in the experiments described in this thesis. Future experiments could also be carried out to investigate

the formation of molecular hydrogen on water ice surfaces, again in order to compare the results from these experiments with the work of other groups [14-17].

6.5. Summary

This Chapter has presented some ideas for the future scope of the Cosmic Dust Experiment, building on the apparatus development and results presented in the earlier chapters of this thesis. The use of the new laser system, coupled with a position sensitive detector should allow a complete investigation of the distribution of the binding energy released on the formation of H_2, and go some way towards answering some of the questions about how this energy release influences the interstellar energy budget.

6.6. References

1. Saito, N., Heiser, F., Hemmers, O., Wieliczek, K., Viefhaus, J., and Becker, U., *Phys. Rev. A*, 1996. **54**(3): p. 2004-2010.
2. Hsieh, S. and Eland, J.H.D., *J. Phys. B-At. Mol. Opt. Phys.*, 1997. **30**(20): p. 4515-4534.
3. Hu, W.P., Harper, S.M., and Price, S.D., *Meas. Sci. Technol.*, 2002. **13**(10): p. 1512-1522.
4. Harper, S.M., Hu, S.W.P., and Price, S.D., *J. Chem. Phys.*, 2004. **121**(8): p. 3507-3514.
5. Hu, W.P., Harper, S.M., and Price, S.D., *Mol. Phys.*, 2005. **103**(13): p. 1809-1819.
6. Duley, W.W. and Williams, D.A., *Interstellar Chemistry*. London ed. 1984: Academic Press.
7. Dyson, J.E. and Williams, D.A., *The Physics of the Interstellar Medium*. 2 ed. 1997: Institute of Physics publishing. 165.
8. Greenberg, J.M., *Surf. Sci.*, 2002. **500**(1-3): p. 793-822.
9. Williams, D.A. and Herbst, E., *Surf. Sci.*, 2002. **500**(1-3): p. 823-837.
10. Perry, J.S.A. and Price, S.D., *Astrophys. Space Sci.*, 2003. **285**(3-4): p. 769-776.
11. Perry, J.S.A., Gingell, J.M., Newson, K.A., To, J., Watanabe, N., and Price, S.D., *Meas. Sci. Technol.*, 2002. **13**: p. 1414-1424.
12. Pirronello, V., Biham, O., Liu, C., Shen, L.O., and Vidali, G., *Astrophys. J.*, 1997. **483**(2): p. L131-L134.
13. Pirronello, V., Liu, C., Shen, L.Y., and Vidali, G., *Astrophys. J.*, 1997. **475**(1): p. L69-L72.
14. Roser, J.E., Manico, G., Pirronello, V., and Vidali, G., *Astrophys. J.*, 2002. **581**(1): p. 276-284.
15. Roser, J.E., Swords, S., Vidali, G., Manico, G., and Pirronello, V., *Astrophys. J.*, 2003. **596**(1): p. L55-L58.

16. Hornekaer, L., Baurichter, A., Petrunin, V.V., Field, D., and Luntz, A.C., *Science*, 2003. **302**(5652): p. 1943-1946.

17. Hornekaer, L., Baurichter, A., Petrunin, V.V., Luntz, A.C., Kay, B.D., and Al-Halabi, A., *J. Chem. Phys.*, 2005. **122**(12): p. art. no.-124701.

Appendix A. Calculation of Ion Flight Times in a Two Field Time-of-Flight Mass Spectrometer

The mass, m, of an ion can be determined using a time-of-flight mass spectrometer (TOFMS) by recording the time it takes for the ion to travel a known distance, after having been accelerated through an electric potential. The flight time, t, is then given by the equation [1]:

$$t = k\sqrt{m} + C \qquad \text{A.1}$$

where k and C are constants.

Figure A.1 shows a schematic diagram of the TOFMS used in the experiments described in this thesis, with the dimensions appropriately labelled for the ion flight time calculations.

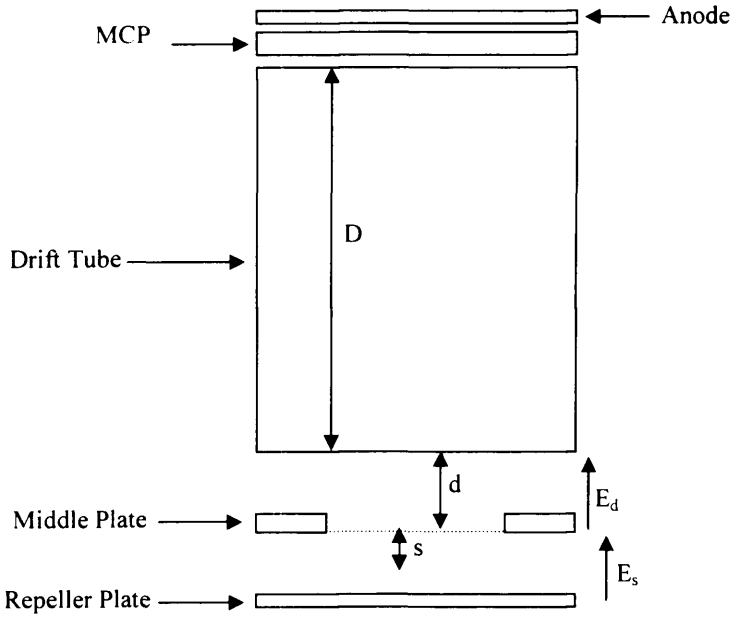

Figure A.1. Schematic diagram of the TOFMS showing the dimensions and electric fields needed to calculate an ion's flight time.

The energy, U, that an ion of charge, q, gains as it moves through an electric field, E, which acts over a distance, s, is given by the equation:

$$U = qsE \qquad \text{A.2}$$

Hence, the final energy gained by an ion of initial energy U_0 travelling through the TOFMS in Figure A.1 is given by:

$$U = U_0 + qsE_s + qdE_d \qquad \text{A.3}$$

The time of flight of an ion (in seconds) traveling in the spectrometer is the sum of the times it takes to travel the distances s, d and D:

$$t = t_s + t_d + t_D \qquad \text{A.4}$$

A standard result from Newtonian mechanics is used to find the time, t_s, it takes for an ion to travel from the point of ionisation to the middle plate of the spectrometer:

$$t_s = \frac{v_s - v_0}{a} \qquad \text{A.5}$$

where v_0 is the initial velocity of the ion, v_s is the ion's velocity after being accelerated through a distance s, and a is the acceleration the ion undergoes due to the electric field, E_s.

v_s is found from:

$$v_s^2 = v_0^2 + 2as \qquad \text{A.6}$$

Substituting equation A.6 into A.5 gives:

$$t_s = \frac{(v_0^2 + 2as)^{\frac{1}{2}} \pm v_0}{a} \qquad \text{A.7}$$

The ± in front of v_0 arises due to the fact that some ions will be created with initial velocities in the direction of the detector and some with initial velocities away from the detector ('-' case).

The initial kinetic energy of an ion is given by:

$$U_0 = \frac{1}{2}mv^2 \qquad \text{A. 8}$$

$$v_0 = \left(\frac{2U_0}{m}\right)^{\frac{1}{2}} \qquad \text{A.9}$$

Substituting equation A.9 into A.7 gives:

$$t_s = \left(\left(\frac{2U_0}{m} + 2as\right)^{\frac{1}{2}} \pm \left(\frac{2U_0}{m}\right)^{\frac{1}{2}}\right)\frac{1}{a} \qquad \text{A.10}$$

The acceleration of an ion can be given in terms of its mass, charge, and the electric field causing the acceleration using Newton's second law:

$$F = ma = qe \Rightarrow a = \frac{qE}{m} \qquad \text{A.11}$$

Substitution equation A.11 into A.10 gives:

$$t_s = \left(\left(\frac{2U_0}{m} + \frac{2sqE_s}{m} \right)^{\frac{1}{2}} \pm \left(\frac{2U_0}{m} \right)^{\frac{1}{2}} \right) \frac{m}{qE_s} \qquad \text{A.12}$$

Equation A.12 can then be simplified to:

$$t_s = \frac{(2m)^{\frac{1}{2}}}{qE_s} \left((U_0 + sqE_s)^{\frac{1}{2}} \pm (U_0)^{\frac{1}{2}} \right) \qquad \text{A.13}$$

Similar arguments can be used to determine the time, t_d, it takes an ion to travel a distance d:

$$t_d = \frac{v_d - v_s}{a} \qquad \text{A.14}$$

where v_d is the ions velocity after being accelerated though a distance d and a is the acceleration of the ion as it passes through an electric field E_d. v_d is found from:

$$v_d^2 = v_s^2 + 2ad = v_s^2 + \frac{2dqE_d}{m} \qquad \text{A.15}$$

Substituting equations A.6 and A.15 into A.14 gives:

$$t_d = \left(\left(v_s^2 + \frac{2dqE_d}{m} \right)^{\frac{1}{2}} - \left(v_0^2 + \frac{2sqE_s}{m} \right)^{\frac{1}{2}} \right) \frac{m}{qE_d} \qquad \text{A.16}$$

Substituting again for equations A.6 and A. 8 gives:

$$t_d = \left((U_0 + sqE_s + dqE_d)^{\frac{1}{2}} - (U_0 + sqE_s)^{\frac{1}{2}} \right) \frac{(2m)^{\frac{1}{2}}}{qE_d} \qquad \text{A.17}$$

Which then simplifies to:

$$t_d = \frac{(2m)^{\frac{1}{2}}}{qE_d}\left(U^{\frac{1}{2}} - (U_0 + qsE_s)^{\frac{1}{2}}\right) \qquad \text{A.18}$$

The ions travel through the drift tube at a constant speed, v_d, as there is no accelerating potential in the drift tube. Therefore, the time, t_d, it takes the ions to travel the length of the drift tube, D, is given by:

$$t_D = \frac{D}{v_d} = \frac{D}{\left(v_s^2 + \frac{2dqE_d}{m}\right)^{\frac{1}{2}}} \qquad \text{A.19}$$

Substituting equations A.6 and A. 8 into equation A.19 gives:

$$t_D = \frac{D}{\left(\left(\frac{2}{m}\right)(U_0 + sqE_s + dqE_d)\right)^{\frac{1}{2}}} \qquad \text{A.20}$$

which simplifies to:

$$t_D = \frac{(2m)^{\frac{1}{2}} D}{2U^{\frac{1}{2}}} \qquad \text{A.21}$$

The total flight time of an ion through the spectrometer (in seconds) is therefore:

$$t = (2m)^{\frac{1}{2}}\left\{\frac{\left((U_0 + sqE_s)^{\frac{1}{2}} \pm (U_0)^{\frac{1}{2}}\right)}{qE_s} + \frac{\left(U^{\frac{q}{m}} - (U_0 + sqE_s)^{\frac{1}{2}}\right)}{qE_d} + \frac{D}{2U^{\frac{1}{2}}}\right\} \qquad \text{A.22}$$

It can be seen from equation A.22 that the time of flight of the ion is proportional to $m^{1/2}$. Since the electric fields and dimensions of the spectrometer are constant, as is the charge on the ion, the equation for the time of flight of the ion can be abbreviated to give equation A.1.

$$t = k\sqrt{m} + C \qquad \text{A.1}$$

The constant k is related to the electric fields and dimensions of the spectrometer and C occurs due to the delays from the spectrometer's electronic timing equipment. The constants can be found by solving two simultaneous equations for two ions of different masses.

Reference

1. Wiley, W.C. and McLaren, I.H., *Rev Sci Instr*, 1955. 26(12): p. 1150-1157.

Chapter 10. Appendix B. Error analysis on the Rotational Populations

As described in Chapter 5, the rotational populations of the nascent molecules are found by determining the area of a rotational peak, corrected for the background, and dividing this area by the laser power normalisation factor, n. In order to find the errors on the measured rotational populations, it is therefore necessary to propagate the error on the background counts under the recorded ion peak, the error on the peak area and the error on the laser power dependence. Figure B.1 below shows a REMPI peak illustrating the various parameters described below.

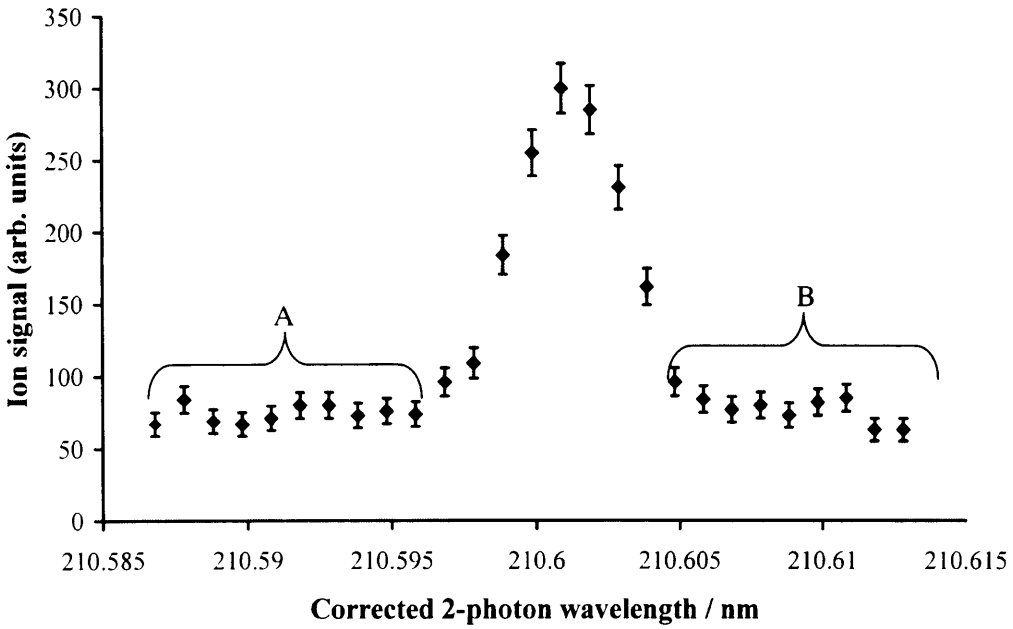

Figure B. 1. REMPI plot showing the A and B parameters described in the text.

The average background count before the peak, A, or after the peak, B, is the mean number of counts before or after the peak. The error on each of the background counts, x_i, is Δx_i. Hence, the error on the average background before the peak, ΔA, is

$$(\Delta A)^2 = \frac{1}{N}\left[(\Delta x_1)^2 + (\Delta x_2)^2 + \cdots + (\Delta x_N)^2\right] \qquad \text{B.1}$$

where N is the number of laser steps before the peak. Rearranging for ΔA gives:

$$\Delta A = \left\{\frac{1}{N}\left[(\Delta x_1)^2 + (\Delta x_2)^2 + \cdots + (\Delta x_N)^2\right]\right\}^{\frac{1}{2}} \qquad \text{B.2}$$

Since $\Delta x_i = \sqrt{x_i}$, it follows that:

$$\Delta A = \sqrt{\frac{1}{N}\sum_{i=1}^{N} x_i} \qquad \text{B.3}$$

which is equal to $\sqrt{}$(mean background counts). The error on the average background counts after the peak, ΔB, is found in the same way.

The error on the measured peak area, E requires propagation of the error on the average background counts under the peak, C and the total average counts under the peak, D.

$$C = \left[\frac{A+B}{2}\right]N \qquad \text{B.4}$$

where N is now the number of laser steps under the peak. ΔC is found from the errors on A and B using equation B.3 to give:

$$(\Delta C)^2 = \left[(\Delta A)^2 + (\Delta B)^2\right]\frac{N}{2} \qquad \text{B.5}$$

hence

$$\Delta C = \left\{\left[(\Delta A)^2 + (\Delta B)^2\right]\frac{N}{2}\right\}^{\frac{1}{2}} \qquad \text{B.6}$$

The error on the total counts under the peak is ΔD:

$$(\Delta D)^2 = (\Delta x_1)^2 + (\Delta x_2)^2 + \cdots + (\Delta x_N)^2 \qquad \text{B.7}$$

and as before, $\Delta x_i = \sqrt{x_i}$, so:

$$\Delta D = \sqrt{\sum_{i=1}^{N} x_i} \qquad \text{B.8}$$

The measured peak area $E = D - C$, hence combining ΔC and ΔD gives ΔE:

$$\Delta E = \left[(\Delta C)^2 + (\Delta D)^2\right]^{\frac{1}{2}} \qquad \text{B.9}$$

The error on the peak area then needs to be propagated through with the error involved in normalising for laser power. The final rotational population, F, is found by dividing the peak area, E, by the laser power, G, raised to the power of its energy dependence:

$$F = \frac{E}{G^n} \qquad \text{B.10}$$

If we let $G^n = H$ then:

$$\left(\frac{\Delta F}{F}\right)^2 = \left(\frac{\Delta E}{E}\right)^2 + \left(\frac{\Delta H}{H}\right)^2 \qquad \text{B.11}$$

Since we know ΔE from equation B.9, we only need to find ΔH.

$H = G^n$ so $\ln H = n \ln G$

If we make the following substitutions:

$\ln H = J$ and $\ln G = K$ then $J = nK$ which gives:

$$\left(\frac{\Delta J}{J}\right)^2 = \left(\frac{\Delta n}{n}\right)^2 + \left(\frac{\Delta K}{K}\right)^2 \qquad \text{B.12}$$

As $K = \ln G$ and $\Delta K = \frac{\Delta G}{G}$, substituting back into equation B.12 gives:

$$\left(\frac{\Delta J}{J}\right)^2 = \left(\frac{\Delta n}{n}\right)^2 + \left(\frac{\Delta G}{G \ln G}\right) \qquad \text{B.13}$$

which gives:

$$\Delta J = J\left[\left(\frac{\Delta n}{n}\right)^2 + \left(\frac{\Delta G}{G \ln G}\right)^2\right]^{\frac{1}{2}} \qquad \text{B.14}$$

But, $J = \ln H$ so $H = \exp J$ giving $\Delta J = \frac{\Delta H}{H}$. Therefore:

$$\frac{\Delta H}{H} = \ln H\left[\left(\frac{\Delta n}{n}\right)^2 + \left(\frac{\Delta G}{G \ln G}\right)^2\right]^{\frac{1}{2}} \qquad \text{B.15}$$

Substituting equation B.15 back into equation B.11 gives:

$$\left(\frac{\Delta F}{F}\right)^2 = \left(\frac{\Delta E}{E}\right)^2 + \left(n \ln G\left[\left(\frac{\Delta n}{n}\right)^2 + \left(\frac{\Delta G}{G \ln G}\right)^2\right]^{\frac{1}{2}}\right)^2 \qquad \text{B.16}$$

Rearranging equation A.16 for ΔF gives us a final error on the rotational population:

$$\Delta F = F\left\{\left(\frac{\Delta E}{E}\right)^2 + \left(n \ln G\left[\left(\frac{\Delta n}{n}\right)^2 + \left(\frac{\Delta G}{G \ln G}\right)^2\right]^{\frac{1}{2}}\right)^2\right\}^{\frac{1}{2}} \qquad \text{B.17}$$

which simplifies to:

$$\Delta F = F\left\{\left(\frac{\Delta E}{E}\right)^2 = (n \ln G)^2\left[\left(\frac{\Delta n}{n}\right)^2 + \left(\frac{\Delta G}{G \ln G}\right)^2\right]\right\}^{\frac{1}{2}} \qquad \text{B.18}$$

where F is the rotational population divided by (laser power)^n, E and ΔE the peak area and associated error, n and Δn the power to which the laser energy is raised for normalisation and its associated error, and G and ΔG the laser power and its associated error.